



Norwegian University of  
Science and Technology

*Master thesis*

# Cryogenic micro-photoluminescence of silicon solar cell materials

by

Jon Skarpeteig

June 7, 2010

Supervisors:  
Helge Weman  
Arne Røyset

*Norwegian University of Science and Technology  
Department of Electronics and Telecommunications*

# Contents

<b>1 Theory</b>	<b>1</b>
1.1 Solar cells . . . . .	1
1.1.1 Bandgap . . . . .	1
1.1.2 Doping . . . . .	3
1.1.3 Transport and recombination processes . . . . .	4
1.1.4 Excitation and recombination . . . . .	5
1.1.5 Solar cell . . . . .	7
1.2 Material science . . . . .	11
1.2.1 Czochralski method . . . . .	11
1.2.2 Float-zone process . . . . .	12
1.2.3 Siemens process . . . . .	12
1.2.4 Multicrystalline silicon . . . . .	12
1.2.5 Wafers . . . . .	13
1.2.6 Doping . . . . .	13
1.2.7 Defects . . . . .	14
1.3 Spectroscopic properties of silicon . . . . .	17
1.3.1 Phonons . . . . .	19
1.3.2 Excitons . . . . .	19
1.3.3 Electron-hole drops . . . . .	21
1.3.4 Pumping wavelength . . . . .	21
1.3.5 Spot size . . . . .	22
1.3.6 Laser intensity . . . . .	22
1.3.7 Temperature dependency . . . . .	23
1.3.8 Spectrometer . . . . .	24
1.3.9 Optics . . . . .	24
1.3.10 Noise . . . . .	25
1.4 Literature review of relevant spectra . . . . .	26
1.4.1 Dislocation photoluminescence . . . . .	26
1.4.2 Impurities . . . . .	28
1.4.3 Atom impurities . . . . .	29
1.4.4 Impurity interaction with dislocations . . . . .	30
<b>2 Experimental</b>	<b>33</b>
2.1 Samples . . . . .	33
2.1.1 R6-Q3-210 . . . . .	33
2.1.2 ES1-Q3-201 . . . . .	33
2.1.3 MH2-Q3-210 . . . . .	34
2.2 Instrumentation . . . . .	36
2.2.1 Optical components . . . . .	37

2.2.2	Pumping wavelength . . . . .	38
2.2.3	Spot size . . . . .	38
2.2.4	Laser intensity . . . . .	38
2.2.5	Temperature . . . . .	39
2.2.6	Spectrometer . . . . .	39
<b>3</b>	<b>Results</b>	<b>40</b>
3.1	R6-Q3-210 . . . . .	40
3.2	ES1-Q3-201 . . . . .	43
3.2.1	Room temperature . . . . .	45
3.2.2	Low temperature . . . . .	46
3.3	MH2-Q3-210 . . . . .	50
3.3.1	Room temperature . . . . .	51
3.3.2	At 70K . . . . .	52
3.3.3	Low temperature . . . . .	53
3.3.4	Line mapping . . . . .	57
<b>4</b>	<b>Discussion</b>	<b>61</b>
4.1	Results plotting . . . . .	62
4.1.1	Disregarding defect pixels . . . . .	62
4.1.2	Noise reduction . . . . .	64
4.1.3	Savitzky-Golay filtering . . . . .	66
4.2	Expected results . . . . .	67
4.2.1	Sample from clean feedstock . . . . .	67
4.2.2	Phosphorus and boron doped samples . . . . .	67
4.2.3	Sample with added Chromium . . . . .	68
4.3	Results analysis . . . . .	69
4.3.1	Comparing different locations on sample R6-Q3-210 . .	69
4.3.2	Comparing different locations on sample ES1-Q3-201 . .	73
4.3.3	Comparing different locations on sample MH2-Q3-210 . .	76
4.3.4	Comparing similar areas on different samples . . . . .	81
<b>A</b>	<b>Silicon energy bands</b>	<b>92</b>
<b>B</b>	<b>Sample types and procedures</b>	<b>94</b>
<b>C</b>	<b>Abbreviations</b>	<b>104</b>
<b>D</b>	<b>Matlab code</b>	<b>105</b>
D.1	Dead pixel correction . . . . .	105
D.2	Dark current noise estimation removal . . . . .	105
D.3	Read result files from directory . . . . .	106

D.4	Remove overlap and glue intervals . . . . .	107
D.5	Filter and plot results . . . . .	108

# List of Figures

1	Energy bands . . . . .	1
2	Typical bandgaps at 0K . . . . .	2
3	Generation and recombination . . . . .	6
4	Direct and indirect recombination (figure from [1]) . . . . .	6
5	Depletion area . . . . .	8
6	Current-voltage characteristics for a solar cell . . . . .	9
7	Current-voltage characteristics with fill factor . . . . .	10
8	I-V characteristics with defects . . . . .	10
9	Czochralski process . . . . .	11
10	Wafer wire saw (figure from CRS Reprocessing LLC) . . . . .	14
11	Dislocations . . . . .	16
12	Area defects . . . . .	17
13	Excitation and recombination [2] . . . . .	18
14	Transverse phonon modes . . . . .	19
15	Excitons . . . . .	20
16	Excitation levels . . . . .	21
17	Numerical aperture . . . . .	25
18	Iron precipitates . . . . .	31
19	Lab setup . . . . .	36
20	R6-Q3-210 A from light microscope . . . . .	40
21	R6-Q3-210 at a dislocation line . . . . .	41
22	R6-Q3-210 at a dislocation dot . . . . .	41
23	R6-Q3-210 at a defect free area . . . . .	42
24	R6-Q3-210 at a grain boundary . . . . .	42
25	R6-Q3-210 at a defect free area . . . . .	43
26	ES1-Q3-201 C from light microscope . . . . .	44
27	ES1-Q3-201 at room temperature . . . . .	45
28	ES1-Q3-201 at a defect free area . . . . .	46
29	ES1-Q3-201 at a defect free area . . . . .	46
30	ES1-Q3-201 at a grain boundary . . . . .	47
31	ES1-Q3-201 at a grain boundary . . . . .	47
32	ES1-Q3-201 at a dislocation line . . . . .	48
33	ES1-Q3-201 at a dislocation line . . . . .	48
34	ES1-Q3-201 at a defect free area . . . . .	49
35	ES1-Q3-201 at a grain boundary . . . . .	49
36	MH2-Q3-210 B2 from light microscope . . . . .	50
37	MH2-Q3-210 at room temperature . . . . .	51
38	MH2-Q3-210 at 70K . . . . .	52
39	MH2-Q3-210 at area 1 . . . . .	53

40	MH2-Q3-210 at area 2 . . . . .	53
41	MH2-Q3-210 at area 3 . . . . .	54
42	MH2-Q3-210 at area 3 . . . . .	55
43	MH2-Q3-210 at area 4 with different intensities . . . . .	55
44	MH2-Q3-210 at area 5 with different intensities . . . . .	56
45	MH2-Q3-210 at area 5 with different temperatures . . . . .	56
46	MH2-Q3-210 line mapping start position . . . . .	57
47	MH2-Q3-210 line mapping end position . . . . .	58
48	MH2-Q3-210 line mapping . . . . .	58
49	MH2-Q3-210 line mapping start position . . . . .	59
50	MH2-Q3-210 line mapping start position . . . . .	60
51	MH2-Q3-210 line mapping . . . . .	60
52	Defective pixels . . . . .	62
53	Defective pixels corrected . . . . .	63
54	Dark current with 10s integration time . . . . .	63
55	Dark current and noise . . . . .	64
56	Dark current removed . . . . .	65
57	R6-Q3-210 comparisons . . . . .	69
58	R6-Q3-210 comparisons close . . . . .	70
59	R6-Q3-210 comparisons close . . . . .	70
60	R6-Q3-210 comparisons close . . . . .	71
61	ES1-Q3-201 comparisons . . . . .	73
62	ES1-Q3-201 comparisons close . . . . .	74
63	ES1-Q3-201 comparisons close . . . . .	74
64	ES1-Q3-201 comparisons close . . . . .	75
65	MH2-Q3-210 comparisons . . . . .	76
66	MH2-Q3-210 comparisons close . . . . .	77
67	MH2-Q3-210 comparisons close . . . . .	77
68	MH2-Q3-210 comparisons close . . . . .	78
69	MH2-Q3-210 line mapping . . . . .	79
70	MH2-Q3-210 line mapping . . . . .	80
71	MH2-Q3-210 line mapping . . . . .	80
72	Comparisons in a clean area . . . . .	81
73	Comparisons in a clean area . . . . .	81
74	Comparisons in a dislocation dot . . . . .	82
75	Comparisons in a dislocation dot . . . . .	82
76	Comparisons in a dislocation line . . . . .	83
77	Comparisons in a dislocation line . . . . .	83
78	Comparison or relative strength . . . . .	84
79	Intrinsic/low doped ( $2 \cdot 10^{14} cm^{-3}$ P atoms) Si PL from [3] . . .	94
80	Boron doped ( $6 \cdot 10^{16} cm^{-3}$ ) Si PL specter from [3] . . . . .	95

81	Phosphorus doped ( $8 \cdot 10^{16} cm^{-3}$ ) Si PL specter from [3] . . . . .	96
82	Iron diffused Si sample at two different temperatures from [4] . .	97
83	Iron diffused boron doped Si sample from [5] . . . . .	98
84	Chromium diffused Boron doped Si sample from [6] . . . . .	99
85	Titanium PL from Ti contaminated 4H SiC from [7] . . . . .	100
86	Dislocation lines from [8] . . . . .	101
87	R1BB plot from [9] . . . . .	103

# 1 Theory

## 1.1 Solar cells

Most solar cells made are crystalline, meaning the structure of atoms is ordered, or periodic. Generally the crystals will contain imperfections and impurities. Some solar cell materials however, are not crystalline, but are missing periodicity. These solar cells are made from amorphous materials.

### 1.1.1 Bandgap

A free electron in vacuum is able to have any energy. An electron in a crystal is bound by an energy gap divided by energy positions the electrons can't possess. Every available energy state can only room two electrons according to the Pauli principle. For a crystal, the energy bands can be viewed as an overlap in between single electron energy states. This can be viewed as the crystals 'electron'-shell.

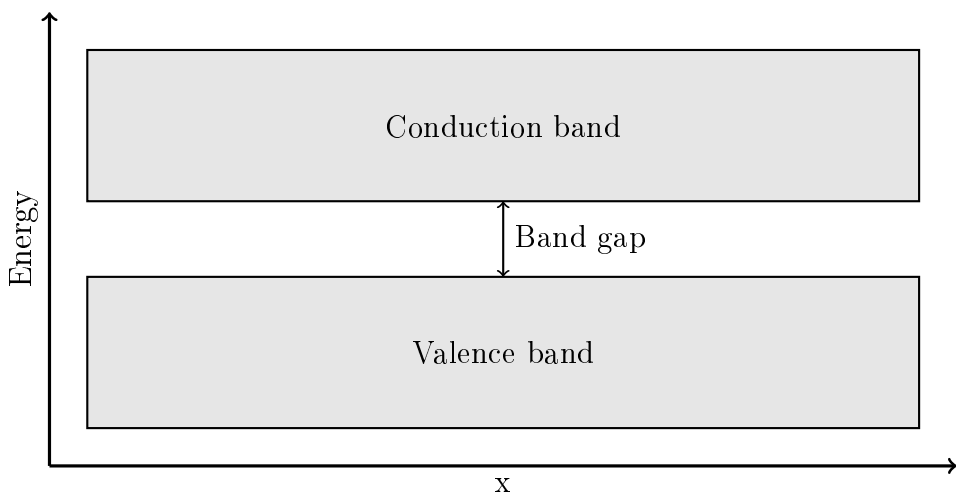


Figure 1: Energy bands

The upper band is called conduction band. The band right below it, is called the valence band. This band gap is very important in relations with solar cells, and is often given in the units of electron volts (eV).

For electrons to move out of the crystal, they have to be in the conduction band. For electrons to get to the conduction band, they need to have enough energy to move from the valence band. This can happen if the electron has enough thermal energy, or receive energy from the outside, like light. This gives the material increased conductivity. In addition to this, there will

be a free state in the valence band, which results in a less probability of collisions among the remaining electron, which lead to a higher mean kinetic energy of the electrons in the valence band. This also contribute to a better conductivity for the material.

For light to excite an electron from the valence band to the conduction band, it needs to have equal, or more energy than the band gap. Energy of light in electron volts is given by:

$$E = h\nu = \frac{hc}{\lambda} \quad (1)$$

where  $E$  is energy in electron volts,  $h$  is Planks constant,  $\nu$  is frequency, and  $c$  is the speed of light.

Materials is often divided into three categories; Isolators, semiconductors, and conductors. Isolators have none, or few electrons in the conduction band, which gives them poor conductivity. Conductors often have filled conduction bands in room temperature, which provide good conductivity. Even with 0K, conductors have a partially filled conduction band. Semiconductors on the other hand, does not have any electrons in the conduction band at 0K. Semiconductors have lower conductivity than conductors, but better than isolators. The bandgap for semiconductors lay in between that of the conductors and isolators. At room temperature semiconductors have a partially filled conduction band.

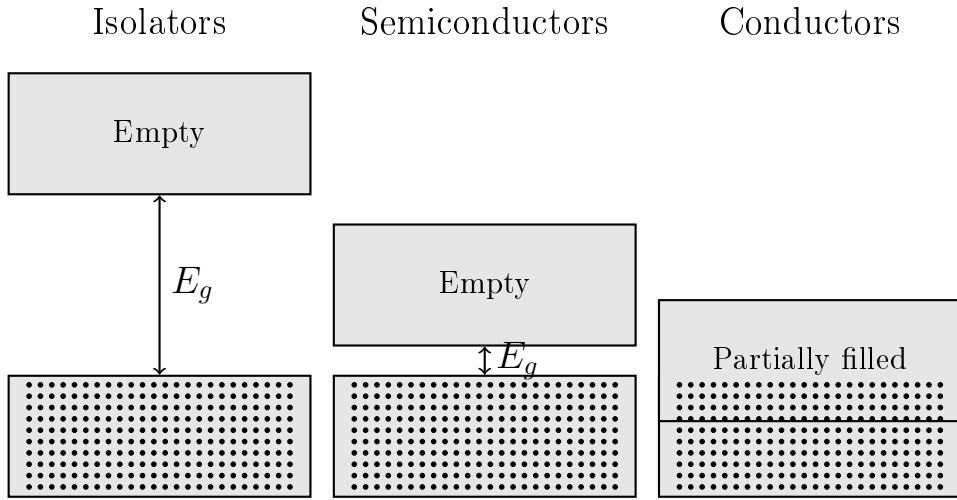


Figure 2: Typical bandgaps at 0K

Typical bandgap for semiconductor silicon is  $E_g=1.1$  eV, compared with

5 eV for diamond, which is an isolator [2, Chapter 3].

Holes is a description of missing electrons in the valence band. A hole will appear when an electron is excited from the valence band into the conduction band. With a small bandgap, and high temperatures, there will be a considerably larger amount of electrons in the conduction band, compared to low temperatures, and a large bandgap. This is described by law of mass action

$$np = N_c N_v e^{-\frac{E_g}{kT}} \quad (2)$$

where  $n$  is number of electrons,  $p$  is number of holes,  $N_c$  and  $N_v$  is constants for a given material,  $E_g$  is the bandgap,  $k$  is Boltzmanns constant, and  $T$  is temperature in Kelvin. For an intrinsic semiconductor, meaning a semiconductor without any doping atoms, like a pure silicon crystal, the law of mass action can be written as

$$np = n_i^2 \quad (3)$$

where

$$n_i = \sqrt{N_c N_v} e^{-\frac{E_g}{2kT}} \quad (4)$$

### 1.1.2 Doping

By adding certain atoms of a different type than those constituting the semiconductor itself, it is possible in increase the concentration of electrons in the conduction band without a concomitant increase on the number of holes in the valence band. This is called donor-doping. An example of donor doping is added phosphorous into a silicon crystal. This will result in more electrons in the conduction band, due to phosphor having one more valence electron than silicon. The doping is usually so small that the band structure won't be affected. By adding phosphorous this way, one has increased electrons,  $n$ , without increasing holes,  $p$ . This is called donor doping. If you instead of phosphor, add boron, the material will be acceptor doped. This is due to boron having one less electron in the valence band than silicon, and would result in an extra hole in the valence band of the crystal. Usually the number of dopants in silicon are substantially larger than the intrinsic concentration,  $n_i$ , so that

$$n \approx N_d \quad (5)$$

for donor doping, and

$$n \approx N_a \quad (6)$$

for acceptor doping where  $N_d$  is donor concentration, and  $N_a$  is acceptor concentration.

A doped semiconductor is generally called extrinsic [2]. If a semiconductor is doped with a number of donor atoms, it is called n-doped or n-type, due to there being more electrons than holes. For acceptor doping it is called p-doped, or p-type semiconductor. The dominating charge carrier in the semiconductor are called majority carriers. The other charge carrier, i.e. holes in the n-type semiconductor are called minority carriers.

### 1.1.3 Transport and recombination processes

There are two mechanisms that contribute to transport of electrons and holes in semiconductors: drift, and diffusion. Drift is a transport of a charge carrier due to an electric field. For transport of a hole in one dimension, the current  $I_p$  is equal to the amount of holes  $N_p$  times the charge  $q$  crossing a cross-sectional area.

$$I_p = N_p q \quad (7)$$

In vacuum, an electric field would accelerate the electrons, and the velocity would increase indefinitely. In solids, however, interactions of collisions with other species in the solid leads to a resistance towards the drift of the charged particles, and after an initial acceleration the velocity becomes constant in a constant electric field. This average drive velocity, denoted  $v_p$  for holes, is related to the electric field  $E$  through the hole mobility  $\mu_p$

$$v_p = \mu_p E \quad (8)$$

If all the electrons is moving in the same direction, the current per area is given by

$$J_p = \frac{I_p}{A} = \frac{N_p q}{A} = p A v_p \frac{q}{A} = p v_p q = p q \mu_p E \quad (9)$$

combined with a similar expression for electrons

$$J = J_p + J_n = (n q \mu_n + p q \mu_p) E = \sigma E \quad (10)$$

where  $\mu_n$  is the mobility for electrons,  $\sigma$  is the semiconductors conductivity, and  $J_n$  is the current density due to the concerted movement of electrons. It is also usual to define the resistivity of the semiconductor as the inverse of its conductivity. The current is then obtained by

$$I = JA = A\sigma E = \left(\frac{A\sigma}{L}\right) V \quad (11)$$

which is recognized as Ohm's law.

Diffusion is a transport process caused by the random motion of the diffusing particles in the medium in which they diffuse. The net transport of particles is in the opposite direction of the concentration gradient. For holes we have

$$N_p = -D_p \frac{dp}{dx} \quad (12)$$

where the proportionality constant  $D_p$  is the diffusion coefficient ( $\text{m}^2/\text{s}$ ) for holes.

The movement of charged particles are frequently determined by the simultaneous presence of electric fields and concentration gradients. Both of the relevant transport parameters, mobilities and diffusion coefficients, will in general depend on temperature. The relation between diffusion coefficient and mobility is

$$\frac{D_p}{\mu_p} = \frac{kT}{q} \quad (13)$$

for holes, and a corresponding one exist for electrons.

#### 1.1.4 Excitation and recombination

Electrons can move from one band to another directly, or indirectly. In indirect generation and recombination the electrons employ the so-called gap-states. Such conditions will always exist in semiconductors and are related to impurities, defects in the crystal structure, boundary surfaces (grain boundaries) and surfaces. Gap-states are in between the valence band and the conduction band, which is not allowed states in a perfect crystal.

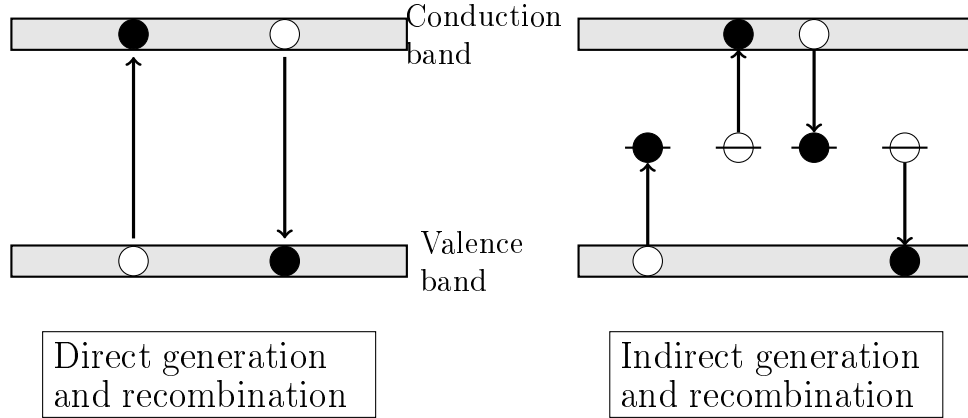


Figure 3: Generation and recombination

In semiconductors with direct bandgap, like GaAs, both processes will occur. In semiconductors with indirect bandgap, like silicon, a direct process cannot happen without contributions from lattice vibrations (phonons), something which makes the process less probable. This is one of the reasons why impurities in silicon solar cells is an important parameter. The electron in an indirect process is moving in the form of a plane wave with propagation constant  $\vec{k}$ , also called wave vector.

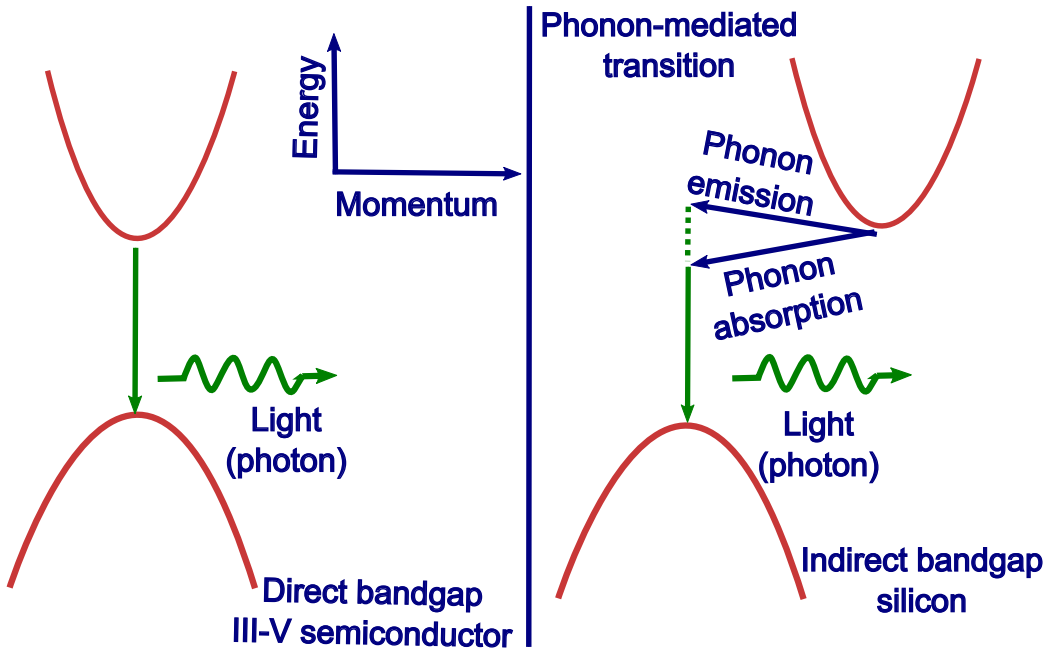


Figure 4: Direct and indirect recombination (figure from [1])

Generation and recombination processes can be described as net flow of electrons to the conduction band,  $U_n$ , proportional to the deviation from equilibrium

$$U_n = -\frac{n - n^0}{\tau_n} \quad (14)$$

where  $\tau_n$  is the lifetime of electrons.  $n$  is the concentration of holes and  $n^0$  is the equilibrium concentration of electrons,  $n^0 = n_i^2$ . The lifetime is the time that an electron of average speeds in the conduction band use before recombining with a hole. Similarly, the net production of holes  $U_p$

$$U_p = -\frac{p - p^0}{\tau_p} \quad (15)$$

### 1.1.5 Solar cell

In a semiconductor with one p-doped, and one n-doped area laying next to each others is called a pn-junction. A pn-junction has rectifying properties, meaning the r electrical conductance are significantly better in one direction than the other, in contrast to a resistor for which it does not matter for the voltage drop across the resistance whether the current runs one way or another through it. This rectifying behavior defines a diode. Due to the p-side having a larger concentration of eletrons in the conduction band than the n-side, there will be a net transport of conduction band electrons from the n-side, to the p-side by diffusion. The same is also happening for holes from the p-side to the n-side. This net flow of charge is called the diffusion current. In principle, the dopants of Si, B, and P can also diffuse between the two parts of the crystal. Such a transport will only be significant at the temperature range of 800 to 900° C, and can be neglected at low temperatures like room temperature.

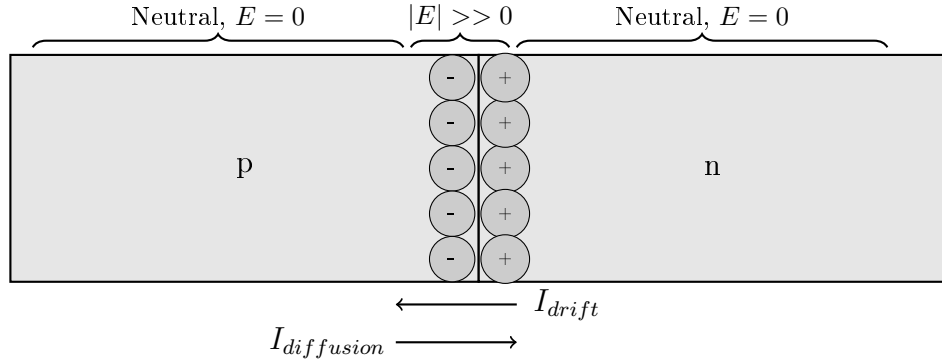


Figure 5: Depletion area

Each hole that leaves the p-side will therefore leave behind an acceptor that is no longer neutralized by a hole. Similarly, each electron in the n-side leave behind a donor that is not neutralized by an electron. A layer near the interface between the two materials with non-neutral donors on the n-side and non-neutral acceptor in the p-side will therefore form. This layer is often called the depletion layer, since it is essentially depleted of free charge carriers. Since the n-side of the depletion layer contains non-neutral donors this side will be positively charged. The corresponding p-side will be negatively charged. These charges therefore will cause an electric field directed from n-to p-side, or a corresponding drop in electrical potential from the n-side to the p-side. This electrical potential is resulting in a drift current which is moving in the opposite direction of the diffusion current which is resulting in equilibrium, meaning zero net flow of current.

By exposing the pn-junction to light, minority carriers may be generated beyond those generated thermally. The carriers are generated by photon absorption. This generation is usually significantly greater than the drift current. A diode not exposed to light has the following current voltage characteristic:

$$I = |I_{drift}| e^{\frac{qV}{kT} - 1} \quad (16)$$

When the diode is exposed to light, the drift current is increased, and the characteristic is changing into:

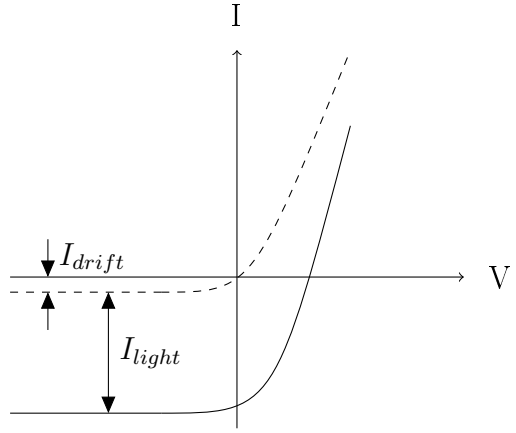


Figure 6: Current-voltage characteristics for a solar cell

For solar cells, the current going out of the cell is usually defined as positive, so that the characteristic is flipped upside-down

$$I = I_{light} - I_{drift}(e^{\frac{qV}{kT}} - 1) \quad (17)$$

where  $I_{light}$ , is the current generated by the exposing light. In an open circuit the voltage is defined as

$$V_{OC} = \frac{kT}{q} \ln\left(\frac{I_{light}}{I_{drift}} + 1\right) \quad (18)$$

and max power defined as

$$P_m = I_m V_m \quad (19)$$

where  $P_m$  is maximum power,  $I_m$  is maximum current and  $V_m$  is maximum voltage. Solar cell efficiency is defined as

$$\eta = \frac{P_m}{P_{inn}} = FF \frac{I_{belysning} V_{OC}}{P_{inn}} \quad (20)$$

where FF is the fill factor give by

$$FF = \frac{I_m V_m}{I_{light} V_{OC}} \quad (21)$$

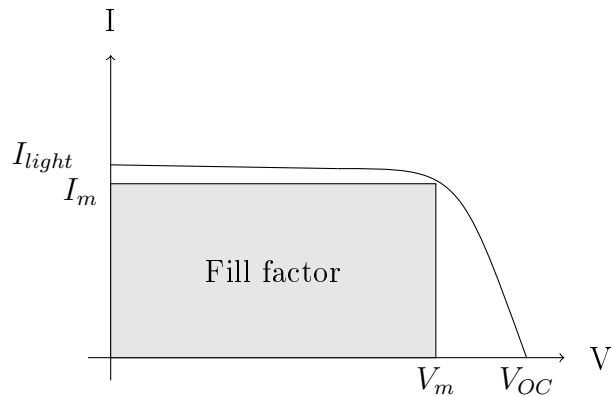


Figure 7: Current-voltage characteristics with fill factor

Solar cells with defects, have a less efficiency than clean samples

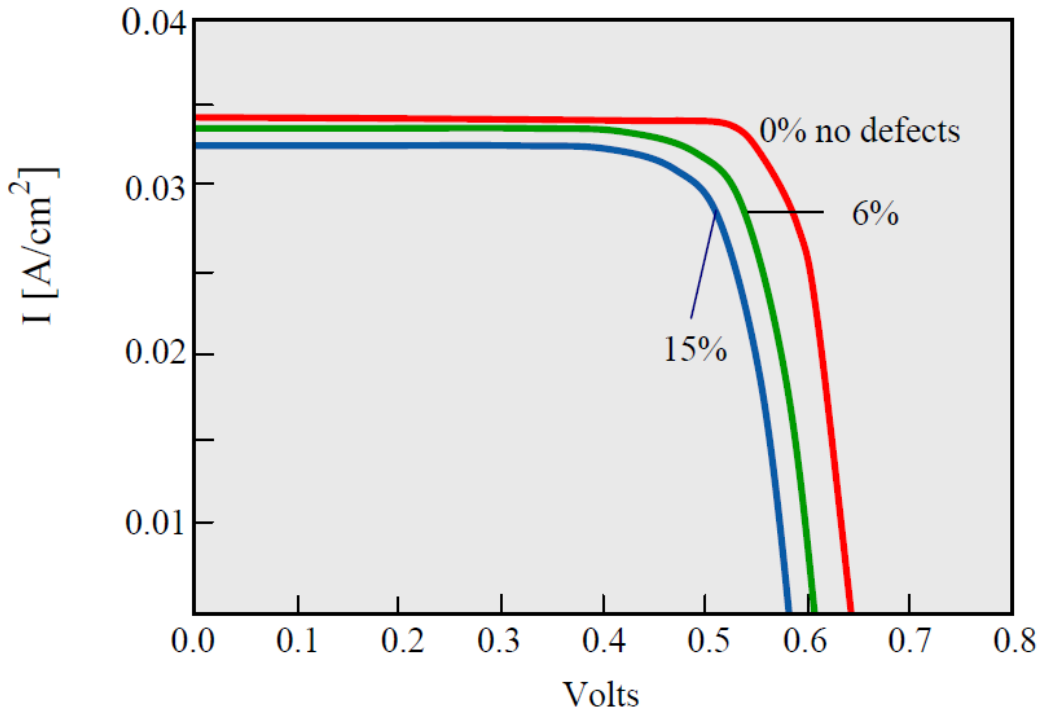


Figure 8: A comparison of calculated I-V characteristics of three cells with 0%, 6%, and 15% of area covered by defects from [10].

which makes it important to be able to characterize defects as well as impurities in order to increase solar cell efficiency.

## 1.2 Material science

A commonly used semiconductor for solar cells is silicon. The supply of silicon is practically endless. 60% of the Earth's crust is sand, for the major part  $\text{SiO}_2$ . Metallurgical grade silicon (MG-Si) is produced in large amount to make special steel alloys. Its purity is only 99% - insufficient for electronic applications [11].

The semiconductor industry purifies this metallurgical-grade silicon until the purity is better than 99.99999%. This corresponds to less than 0.1ppma (part per million atomic), meaning that the total number of foreign atoms must be less than  $5 \cdot 10^{15} \text{ cm}^{-3}$ , due to silicon crystalline atoms density of  $5 \cdot 10^{22} \text{ cm}^{-3}$  [11].

Semiconductor-grade silicon is about ten times more pure than solar-grade silicon. That means that solar-grade silicon can contain up to 1 ppma impurities and still permit reasonably efficient cells. This allows for a lower cost purification process.

### 1.2.1 Czochralski method

The most common crystallization method used for both microelectronic and photovoltaic industries is the Czochralski (CZ) [11], shown in figure 9.

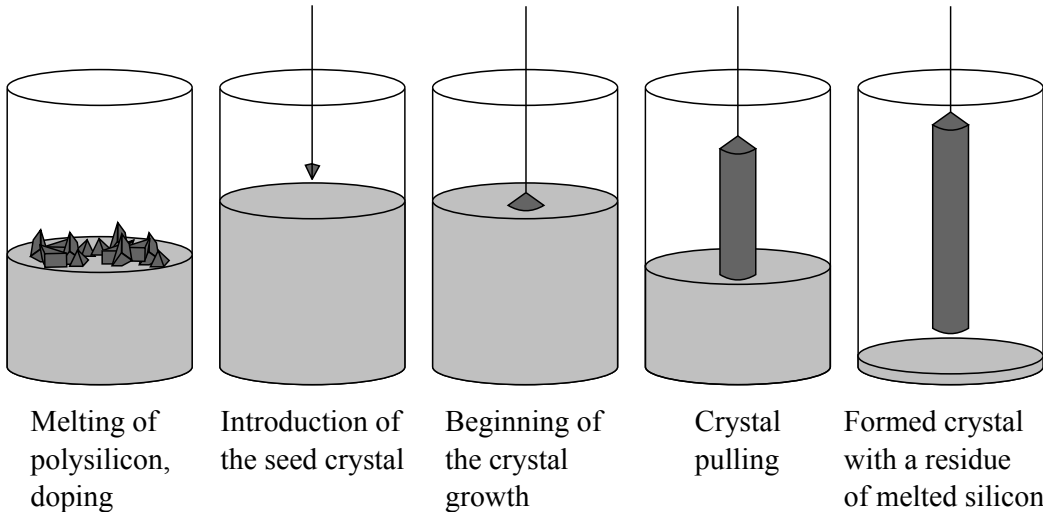


Figure 9: Czochralski process

In the CZ crystal growth, silicon chunks are first melted at  $1414^\circ\text{C}$  in a graphite crucible lined with high purity quartz ( $\text{SiO}_2$ ). This crucible is known as a feedstock. A small polysilicon crystal is used as a seed to start

the crystallization process. The seed is carefully put in contact with the melt and then pulled out very slowly. The temperature is controlled, so that the silicon solidifies at the interface between the seed and the melt and the atoms arrange themselves according to the crystallographic structure of the seed. The crystal grows both vertically and laterally, aided by a rotation movement, yielding a cylindrical ingot of single-crystal silicon.

The growth rate in the CZ method is about 5 cm/h and the cylindrical ingots are typically 1m long, 20 cm in diameter and 75 kg in weight [11]. A disadvantage of the CZ method is that the interaction between the molten silicon and the crucible introduces some contaminants, in particular carbon and oxygen.

### 1.2.2 Float-zone process

The highest quality silicon crystals are obtained by using the float-zone process. In this method, the starting polysilicon is first given the shape of a cylindrical bar. The bar is then locally melted by a coil using radio frequency induction. By moving the coil, and hence the molten zone, along the bar starting from the seed end, the silicon adopts the crystalline structure. The molten zone is self-supporting and is never in contact with a foreign material, thus avoiding contamination problems. The typical growth rate is 15-30 cm/h and the typical ingot is 15 cm in diameter and 1 m in length.

### 1.2.3 Siemens process

In the Siemens reactor process, trichlorosilane gas is introduced into a thermal decomposition furnace (reactor) exposing high-purity silicon rods at 1150 °C. The trichlorosilane gas decomposes and deposits additional silicon onto the rods, enlarging them:



The silicon contained in the gas will deposit on the heated rods, which gradually grow until the desired diameter has been reached. The end product is in the form of rods or chunks of polysilicon. The technology in the Siemens reactor is widely implemented, accounting for a majority of the polysilicon production today, and produces a high purity material [12].

### 1.2.4 Multicrystalline silicon

In order to reduce costs and increase production rates, the multicrystalline silicon (mc-Si) production method was developed. It is possible to grow

silicon ingots by simply melting the starting material, typically silicon scrap, into a crucible and carefully controlling the cooling rate. Upon cooling, a directional solidification takes place and relatively large crystals grow in a columnar way. A crystalline seed is not used, and the nucleation of the silicon atoms commences in many places simultaneously, leading to a myriad of crystals (or grains) of arbitrary shape and crystallographic orientation. Each grain is several millimeters to centimeters across, and internally it has the same structure as single crystalline silicon. The boundaries between the different grains (grain boundaries), are the most obvious imperfection in the material, but they are not the only ones. Microdefects are also common and contamination from the crucible can happen as well, not to mention the possible impurities present in the starting silicon. This means that the mc-Si typically has lower electronic quality than the material produced by the CZ method. Mc-Si typically contains much less oxygen than CZ-Si. The typical crystallization rate is 3.5 kg, and the growth cycle of a complete 16 kg ingot takes 46h [11].

### 1.2.5 Wafers

The silicon ingots have to be sliced into wafers. Before this they are shaped to meet dimensional specifications. The cylindrical CZ ingots are usually reduced to a quasi-square shape. This implies a loss of about 25% of the material, but is necessary if a high packing factor of the cells in the module is required. The large cast silicon parallelepipeds are sawn into smaller bricks. In the case of mc-Si ingots, the shaping is also used to discard the peripheral regions that are usually heavily contaminated by the crucible, which represents approximately 15% of the ingot. In the photovoltaic industry the wafers are cut by a multi-wire saw machines that can cut simultaneously whole blocks, thus increasing the throughput dramatically (figure 10).

An abrasive slurry helps the steel wires cut through silicon, which is a very hard material. The cutting is very slow, with eight hours being typically needed to cut through a  $10 \times 10 \text{ cm}^2$  block. Despite this advanced technique, slicing remains as one of the most costly steps of the whole silicon solar cell fabrication. Even if very thin wires are used approximately 30% of the silicon is wasted as saw dust [11].

### 1.2.6 Doping

A controlled amount of boron or phosphorus is usually added to the melt (feedstock) to dope the silicon p- or n-type. Rather than the elemental boron or phosphorous, accurately measured amounts of silicon heavily doped with

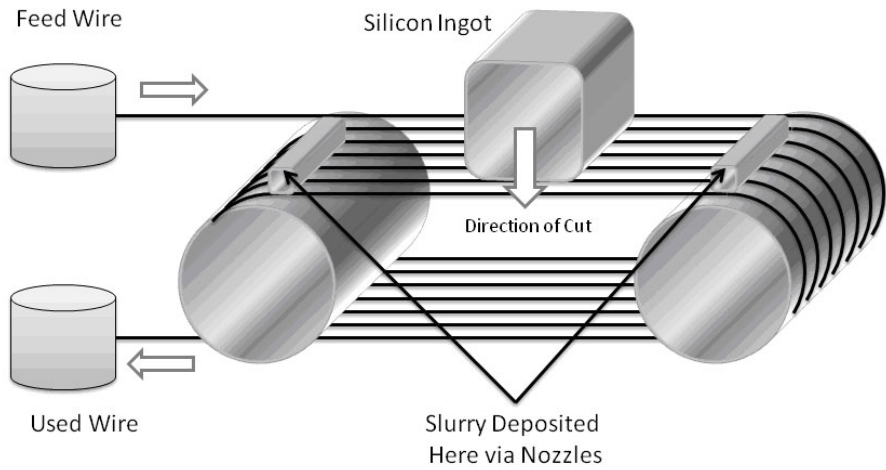


Figure 10: Wafer wire saw (figure from CRS Reprocessing LLC)

those elements are added to the melt. The typical boron concentration is used for solar cell applications is  $1.5 \cdot 10^{16} \text{ cm}^{-3}$ , which results in a resistivity of  $1 \Omega\text{cm}$  [11].

### 1.2.7 Defects

Crystals possess imperfections. They are often referred to as crystalline defects. The presence of most of these crystalline defects is undesirable in silicon wafers. Crystalline defects may be classified into four categories according to their geometry; zero-dimensional or point defects, one-dimensional or line defects, two-dimensional or area defects, and three-dimensional or volume defects

Defect type	Examples
Point or zero-dimensional defects	Vacancy defects Interstitial defects Frenkel defects Extrinsic defects
Line or one-dimensional defects	Straight dislocations (edge or screw) Dislocation loops
Area or two-dimensional defects	Stacking faults Twins Grain boundaries
volume or three-dimentional defects	Precipitates Voids

Table 1: Examples of crystalline defects from [13]

Vacancy defects are defects where a silicon atom is missing in the crystal structure. If an atom is located at a non-lattice location within the crystal, it is known as an interstitial defect. If the interstitial defect involves a silicon atom at an interstitial site within a silicon crystal, then it is referred to as a self-interstitial defect. Vacancies and self-interstitial defects are classified as intrinsic point defects [13].

A Frenkel defect, is when an atom vacates its position in the crystal lattice to an interstitial position. Extrinsic point defects involve a foreign atom, and are more critical than intrinsic point defects. If this foreign atom replace a silicon atom in the lattice, it becomes a substitutional impurity. This include impurity atoms like the dopants B and P. Other common impurities are oxygen, carbon, and metals [14].

Dislocations, or crystal line defects consists of edge dislocations, screw dislocations or a combination of the two. Edge dislocation can be described as an extra plane of atoms squeezed into a part of the crystal lattice. The location with extra atoms would be under compressive stresses, while the part with correct number of atoms would be under tensile stresses. The line connecting all the atoms at the end of the extra plane is known as the dislocation line.

Screw dislocation is such that a step or ramp is formed by the displacement of atoms in a plane in the crystal. The dislocation line of a screw dislocation is in the axis of the screw.

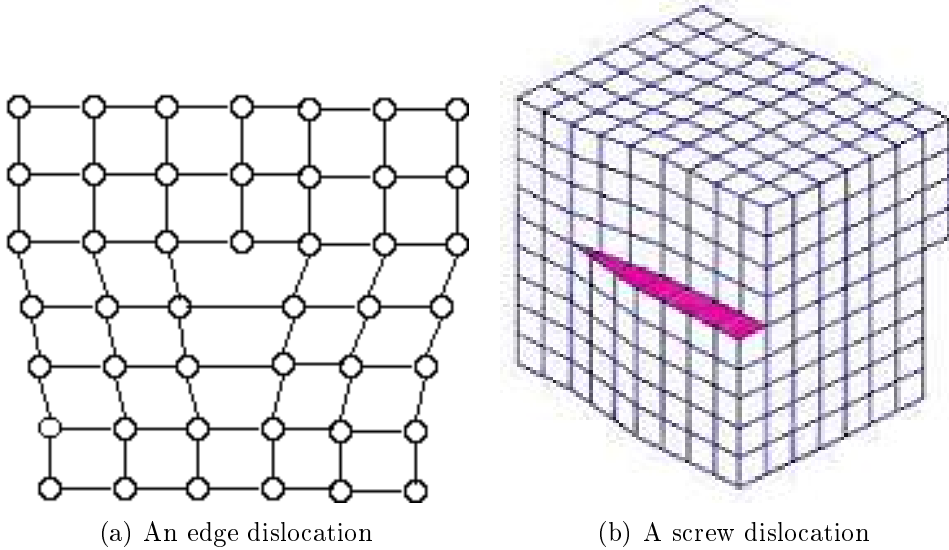


Figure 11: Dislocations

Dislocation loop is a closed curve consisting of an extra plane of atoms lying entirely within the crystal. The line usually form a circular shape, since this shape results in the lowest dislocation energy [13].

Dislocations are not wanted in silicon wafers because impurities are known as recombination centers [15] and serve as sinks for metallic impurities. Gettering may also occur at dislocations, which can lead to the formation of precipitates.

Stacking faults can be considered as a disturbance in the regularity of the stacking of planes in a crystal lattice. This can occur when a plane is inserted or removed from the lattice. Stacking faults can become electrically active when decorated by impurity atoms. Such stacking faults can lead to device degradation.

A twin is a mirroring of a regular lattice formed during the growth of the silicon ingot. This is usually caused by perturbation. The twin boundary is the mirror plane of the twin formation as seen in figure (12(b));

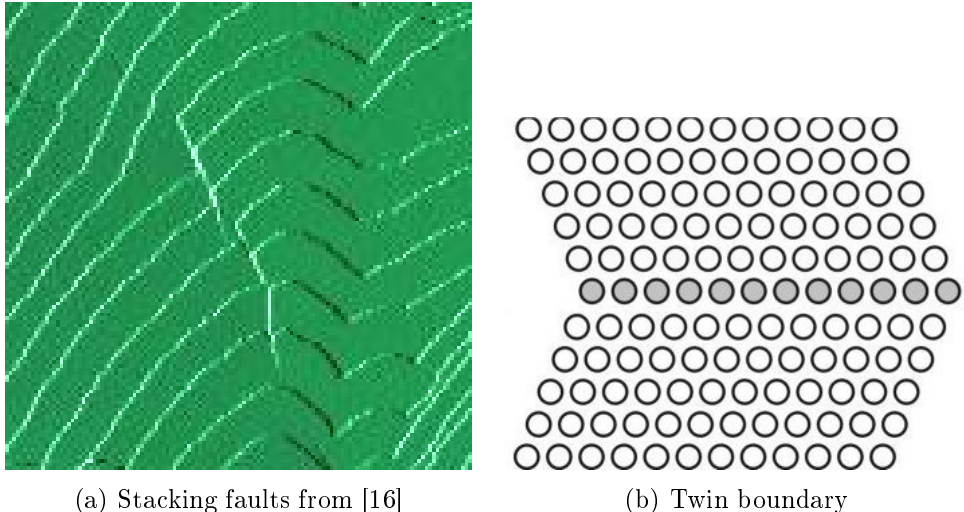


Figure 12: Area defects

Grain boundaries are the boundary in between individual grains where crystal orientation is different from one another. This is common in mc-Si samples due to the production method.

Bulk or volume defects include voids and precipitates of extrinsic and intrinsic point defects. Impurities in a crystal which are introduced at a high temperature usually have a higher solubility than for lower temperatures. If the maximum concentration of an impurity allowed by its solubility at high temperature, the crystal become supersaturated with that impurity once it is cooled down. Under such supersaturated conditions, the crystal seeks and achieves equilibrium by precipitating the excess impurity atoms into another plane phase of different composition or structure. Precipitates are undesirable because they can act as sites for generation of dislocations. Precipitates can form in silicon from metallic impurities, oxygen and dopants like boron [13].

### 1.3 Spectroscopic properties of silicon

When an electron hole pair is recombining, the energy is released as a photon. By measuring this photon in a photo detector it can be determined how much energy that was released during recombination. This energy tells how large the band gap is, which in turn tells us something about the material. By shining light with high enough energy and intensity on to a sample, the light will excite electrons into all available states. When these states recombine, the emitted light can be detected by a camera as a spectra of different wavelengths. The fundamental energy gap between the valence and

conduction bands in silicon is indirect, decreasing monotonically from 1.170 eV at 0 K to 1.125 eV at room temperature [14]. The main phonon contribution (TO phonons) result in energies 1.1 eV for the emitted photons. If there are impurities or defects in the silicon crystal, they can in turn emit light at different photon energies. In order to generate electron-hole pairs, the sample can be excited by a laser. The laser wavelength have to be such that the energy of the light is larger than the band gap, in order to excite the sample.

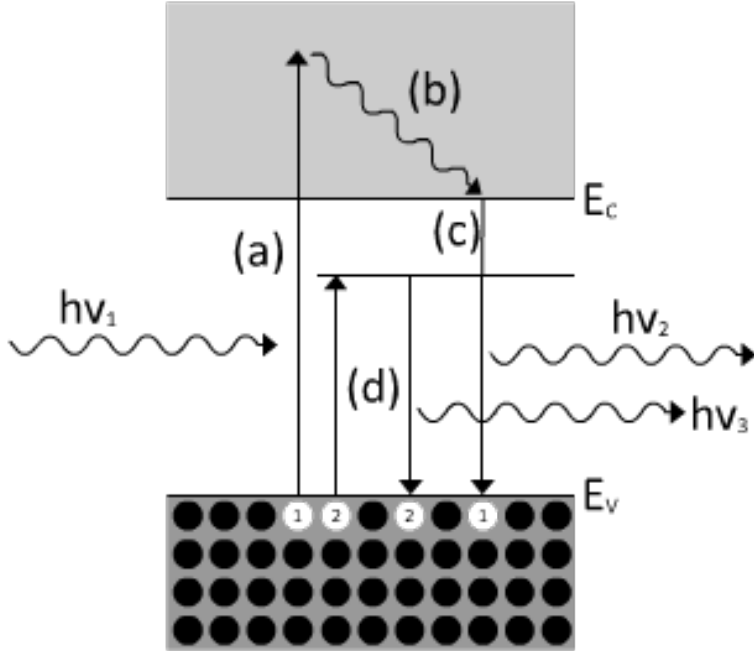


Figure 13: Excitation and recombination [2]

Figure 13 show incoming light with high intensity in a direct band gap material. In *a*, an electron is excited to a high energy state, which falls down to a lower energy state in *b*, after a very short time. When this electron recombines in *c*, it emits a photon with energy equal to  $E_c$ . Another electron is excited in *d*, which reach a so-called trap state, which can occur from impurities in the crystal, or defects. This trap state have a lower energy than the band gap, and when this electron hole pair recombines, and lower energy is emitted. By looking at the light from such trap states, certain known spectra related to different impurities and defects can be recognized.

For an indirect band gap material like silicon, there are other energy levels than the band gap to consider:

### 1.3.1 Phonons

A phonon is an elastic wave in a material such as a silicon crystal. It can be described as lattice vibrations, where the phonon propagate with wave vector  $\vec{k}$ . There is longitudinal (LA), transverse acoustical (TA), longitudinal (LO), and transverse optical (TO) modes.

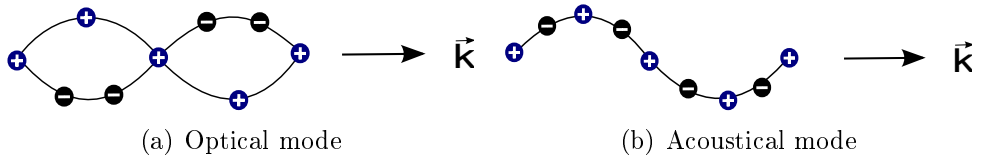


Figure 14: Transverse phonon modes

The atoms in the crystal vibrate against each other, but their center of mass is fixed. If the two atoms carry opposite charges, we may excite a motion of transversal optical with the electric field of a light wave, so that the branch is called the optical branch. If the atoms move together, as in long wavelength acoustical vibrations, whence the term acoustical branch.

Since an electron-hole pair in silicon needs a phonon to recombine, the energy of which the emitted photon has, is highly dependant on the phonon energy involved, as well as the band gap. At absolute zero temperature, a crystal lattice lies in its ground state, and contains no phonons. A lattice at a non-zero temperature has an energy that is not constant, but fluctuates randomly about some mean value. These energy fluctuations are caused by random lattice vibrations, which can be viewed as a gas of phonons. Due to a vast amount of phonons at room temperature, the energy released by recombination varies due to larger fluctuations. In silicon, the optical modes are found right above 48 meV, transverse acoustic (TA) modes are right below 25 meV, and LA modes are in between [17]. [14] list phonon energies in silicon as

$18.4 \pm 0.2$ meV	TA mode
$56.2 \pm 1$ meV	LO mode
$58.0 \pm 1$ meV	TO mode

Table 2: Phonon modes in silicon from [14]

### 1.3.2 Excitons

An exciton is a quasi particle describing an electron bound to a hole. Electrons can be bound together by their attractive coulomb interaction, just as

an electron is bound to a proton form a neutral hydrogen atom. An exciton can move through the crystal and transport energy, however it does not transport charge because it is electrically neutral.

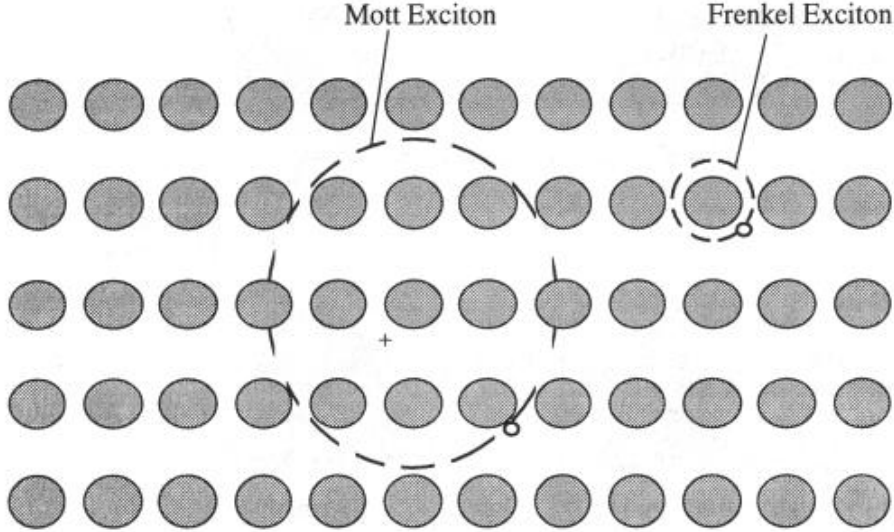


Figure 15: The Mott-Wannier exciton usually free to move together through the crystal, and is weakly bound, with an average electron-hole distance large in comparison with the lattice constant. An ideal Frenkel exciton will travel as a wave throughout the crystal, but the electron is always close to the hole.

Excitons can be formed in every insulating crystal. When the band gap is indirect excitons near the direct gap may be unstable with respect to decay into a free electron and a free hole. All excitons are unstable with respect to the ultimate recombination process in which the electron drops into the hole. Excitons can also form complexes, such as a biexciton from two excitons [18]. In the formation of excitons, the energy is lowered with respect to the binding energy of the exciton. For silicon, the binding energy is 14.7 meV [18]. In a tightly bound exciton (Frenkel) the excitation is localized on or near a single atom. The hole is usually on the same atom as the electron although the pair may be anywhere in the crystal. Boron bound excitons have binding energy 3.8 meV, and phosphorus bound excitons have binding energy 4.7 meV [14].

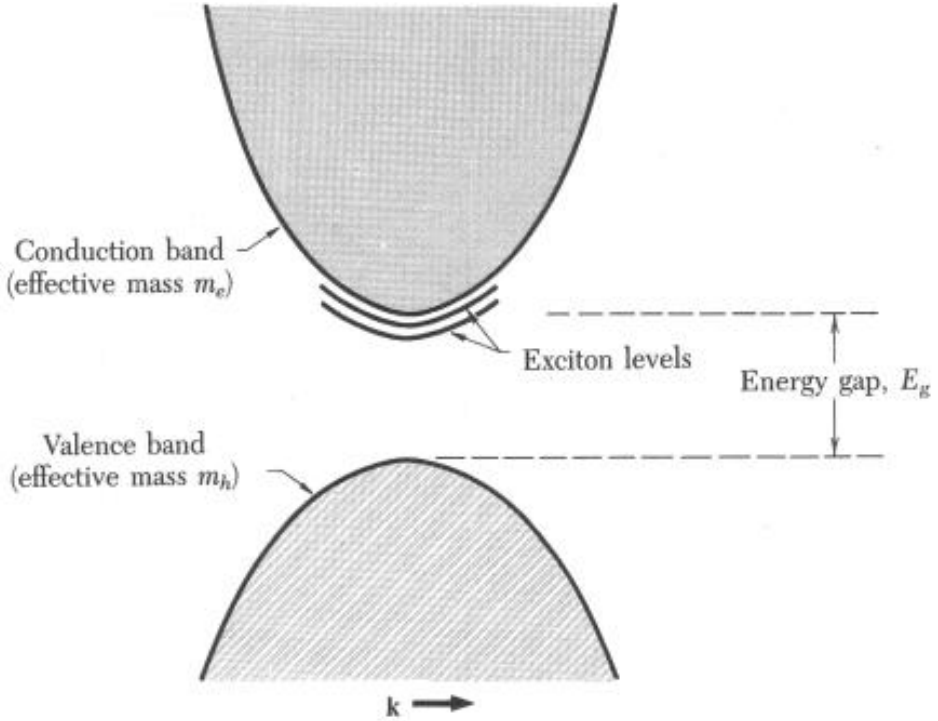


Figure 16: Exciton levels in relation to the conduction band edge for a simple band structure with both conduction and valence band edges at  $\vec{k}=0$ . Figure from [18]

### 1.3.3 Electron-hole drops

A condensed phase of an electron-hole plasma forms in Ge and Si when maintained at a low temperature and irradiated by light. When an electron-hole drop (EHD) forms, the absorption of a photon produces a free electron and free hole with high efficiency. These combine rapidly to form an exciton. If the exciton concentration is sufficiently high, most of the excitons will condense into a drop. The binding energy relative to free exciton is 9.3 meV in silicon with  $3.5 \cdot 10^{18} \text{ cm}^{-3}$  n or p at 23K [18].

### 1.3.4 Pumping wavelength

Pumping light needs to have enough energy to fill all available states in the crystal lattice, in order to detect defects and impurities. For silicon, which has a band gap of around 1.1eV, has most impurity/defect bands below the band gap. In order to fill these states, the pumping wavelength should be

below 1125nm, which corresponds to energies just over 1.1eV.

Silicon has different absorption lengths for different wavelengths. Absorption length is about  $1\text{ }\mu\text{m}$  for 532 nm laser excitation, which means that precipitates, and defects deeper in the sample like iron precipitates won't be detected [19]. By comparison, 800 nm, reach  $12\text{ }\mu\text{m}$  into the sample, and 1125 nm reach as far down as  $200\text{ }\mu\text{m}$  [20]. This limitation might be overcome by an excitation laser with a longer wavelength, and consequently absorption length in silicon.

### 1.3.5 Spot size

Having a small diameter on the pumping laser allows for a high resolution of characteristics on the sample. In an iron contaminated sample, [19] show that at some distinct spots of a size between  $1\mu\text{m}$  and  $4\mu\text{m}$ , the band to band photoluminescence peak is particular low at spots with iron precipitates.

A large electron hole droplet could overshadow characteristics from impurities in the sample. [21] show that electron hole droplets become more intense for a smaller volume, with a silicon nanolayer smaller than the absorption depth of the laser. [21] used a 488nm pumping laser with  $1,5\mu\text{m}$  diameter, on silicon nanolayer thickness of 50nm and 340nm. For the 50nm layer, [21] observed a large electron hole droplet, even for small pumping intensities, with the same amount of photo excited carriers per volume as for the 340nm layer. Assuming that a small volume give rise to a larger electron hole droplet, it would be a limiting factor for the spot size and pumping wavelength.

### 1.3.6 Laser intensity

High excitation laser intensity gives a high signal to noise ratio. But with a large pumping intensity, an electron hole droplet become visible in the specter around 1.08eV in bulk silicon [22]. This electron-hole drop is also more intense at small volumes. [21] show that electron hole droplets occur at weak excitations (0.75mW) and even at high temperatures for a silicon nanolayer of 50nm. For thickness of 340nm, the electron hole droplet show up at pumping intensity of 3mW and above, and the intensity of the electron hole droplet grow larger than for the free exciton at 15mW. This electron hole droplet is not wanted, as it can mask characteristic photoluminescence from impurities.

With a larger pumping intensity, the impurity photoluminescence would in some cases also increase. Photoluminescence from chromium bound with a boron atom is known to increase linearly with laser power [23, 6], and would

be easier to detect at a higher pumping intensity.

Temperature increase is also an issue with high laser intensity. When hitting a small area on the sample, the temperature in that particular area will rise rapidly unless subject to heavy cooling. This can lead to material stress, and broadening of the luminescence energy spectra due to different phonon energies.

### 1.3.7 Temperature dependency

At room temperature, there's a large probability that the phonon energy involved in recombination has an energy considerably different from the mean value, compared to temperatures close to 0K. This makes it difficult to separate phonon assisted recombination, from other available states, like direct recombination trap states. Trap states are important because they describe impurities by exact photon energies, which in turn makes it possible to recognize known impurities. But any recombination involving phonons will have a substantial broadening in regards to energy at room temperature.

To overcome the problem distributed phonon energies, the sample can be cooled down. When cooling down, there are less phonon states available, leading to a much narrower energy distribution of the phonons. This is desirable when looking at the photoluminescence, in order to recognize known spectra. Due to the low binding energies involved in silicon, individual lines would be next to impossible to detect without very low temperatures.

Low temperatures, and high exciting laser light intensity can lead to electron-hole drops. Temperature is a substantial limiting factor for measuring silicon luminescence spectra, meaning low temperature is key to analyze silicon photoluminescence. Electron-hole drops are undesirable because they don't carry information about the material itself, and can emit light at the same wavelengths as actual material properties would. This is a limiting factor at low temperatures on the laser intensity, spot size, and wavelength.

A common way to cool down a sample, is to use liquid nitrogen. Nitrogen has a boiling temperature of 77K, so by exposing the sample to boiling nitrogen, it is cooled down. This can be done in a cryostat, which essentially is a vacuum chamber with a sample holder, where the sample holder is being cooled down. This way there will be no nitrogen contaminants on the sample itself, with only the sample holder being cooled down by nitrogen directly. It's also common to mount the sample holder on piezo elements, which can be used to move the sample in xyz directions.

For silicon, 77K still leads to substantial broadening of emitted photon energies. In order to reach lower temperatures, a different coolant can be used. By using helium, which has a boiling temperature of 4.2K, the en-

ergy broadening is reduced to negligible values, and sharp lines from the photoluminescence can be detected.

### 1.3.8 Spectrometer

In order to analyze different wavelengths, they need to be separated, and detected individually. This is done in a spectrometer. By shining light on a diffraction grating, the light is reflected at different angles by

$$d \sin(\theta_m) = m\lambda \quad (23)$$

where  $d$  is the distance between the grating lines,  $\theta_m$  is the outgoing angle of the light,  $m$  is an integer denoting the diffraction order, and  $\lambda$  is the wavelength. For large wavelength resolution, the angle of the reflected light will be large as well. So, in order to measure a large spectra of wavelengths, several measurements with different center wavelengths is needed. This is due to physical limitations regarding the photo detector. There is a limit to how small a single pixel can be, and how long the array of pixels you can fit in the system. Each pixel translates to a separate wavelength, which measure the intensity of that wavelength only, which result in a full spectra of wavelengths and intensities.

### 1.3.9 Optics

For silicon luminescence, the interesting wavelengths is from 900 to 1600nm, which corresponds to 1.38 eV and 0.77 eV (see table 7). To collect this light, the optics should have minimum loss for these wavelengths.

A common way to measure photoluminescence is to send the laser excitation light through a beam splitter, which reflects 50% of the laser light on to the sample. Then the luminescence pass through the same beam-splitter, where 50% is transmitted, and into the spectrometer. For micro-photoluminescence, it's desireable to hit a very small area of the sample (order of 1  $\mu\text{m}$ ). This can be achieved by using an objective. The objective focuses the excitation laser beam with a size given by the objective specifications in the focal plane, which is the plane of focus for the objective. The length to this plane from the objective (or other optical system), is given by its numerical aperture which in turn is given by:

$$NA = n \sin(\theta) \quad (24)$$

where  $n$  is the refractive index of the medium in which the lens is working (1.0 for air, 1.33 for pure water), and  $\theta$  is the half-angle of the maximum cone of light that can enter or exit the lens.

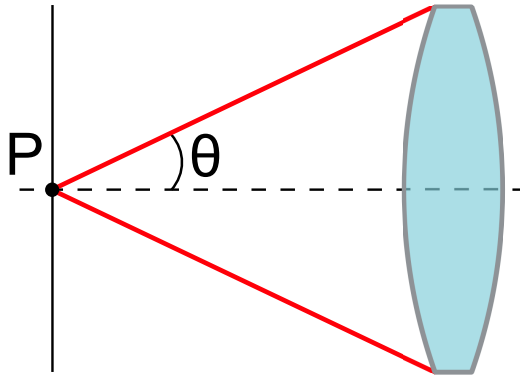


Figure 17: The numerical aperture with respect to a point  $P$  depending on the half-angle  $\theta$

where the point  $P$  is the focus point. NA is important since it indicates the resolving power of a lens. The size of the details that can be resolved is proportional to  $\lambda/NA$ , where  $\lambda$  is the wavelength of the light. A lens with a larger numerical aperture will be able to visualize finer details than a lens with a smaller numerical aperture. Lenses with larger numerical apertures also collect more light which is essential to detect luminescence of lower intensities.

### 1.3.10 Noise

In addition to the actual photoluminescence signal, there will be noise. Noise can be from stray light in the surrounding environment hitting the camera, or it can be noise from the electronics in the camera itself. Examples of noise are thermal noise, dark current, uneven amplification for different pixels in the detector, second (or more) order diffracted light from other wavelengths, background noise and different intensities for different photon energies. All measurements will be subject to noise. By having a longer integration time the signal to noise ratio is likely to increase. But a long integration time, result in a higher dark current signal. Dark current is thermally generated in the detector of the camera, and is independent of the incoming light. By cooling down the detector, the dark current noise is reduced to a minimum. This in turn makes long integration time possible, without the noise floor drowning weak signals. By blocking the signal, the dark current in addition to background light can be measured, and then subtract this noise from the measurement containing the signal. Background light should be consistent in regards to wavelength, compared to dark current, and can be subtracted more accurately. As for dark current, only an averaging is possible to subtract.

This remaining white noise component is not possible to remove, and is clearly visible in areas without any signal. Second order diffraction can be a problem when pumping with a laser due to high intensities. Using a 532 nm laser to pump with, can result in second order diffraction at 1064 nm, which corresponds to 1.165 eV. The laser is reflected off the sample, and needs to be blocked before entering the spectrometer. However, it is possible that some light may slip through the filter, and with 532 nm pumping wavelength, the second order diffraction energy is right next to silicon band gap which is actual signal from the photoluminescence. By using a different pumping wavelength, or having a close to perfect filter would solve this problem.

## 1.4 Literature review of relevant spectra

### 1.4.1 Dislocation photoluminescence

Several investigations have documented that dislocations in silicon give rise to characteristic photoluminescence (PL) spectra below the band edge. First showed for low temperatures in [24], which labeled them D1 (0.812eV), D2 (0.875eV), D3 (0.934eV) and D4 (1.000eV). The samples where deformed at 850° C by bending, so that dislocation densities was inhomogeneous along the samples. [24] states that the intensity of these lines increase closer to the dislocation-rich parts of the crystal. At the same time the intensity of the intrinsic characteristics decrease. The distance between D1-D4 ( $62 \pm 3$  meV) corresponds to the energy of the optical phonons in silicon [24]. [24] reports that D1 and D2 are dominant in heavily deformed Si crystals, while D3 and D4 predominate in weakly deformed Si. A similar result was also reported by recent study [25] for small angle grain boundaries using cathodoluminescence.

It has been suggested in [26] that D1-D4 are due to dislocations which have been frozen in under low-shear stress. [26] state that photoluminescence under uniaxial stress shows that D1/D2 originate in the tetragonal defect with random orientation relative to  $\langle 100 \rangle$  directions. [26] conclude that D3 and D4 are closely related, whereas the independent D1/D2 centers might be deformation-produced point defects in the strain region of dislocations. D1 and D2 is known to be closely related, as well as D3 and D4, and there have been no reports on the D-line spectrum missing only the D1 line [27].

The origin of D1 and D2 is not clear. It has been argued that they originate in electronic transition at the geometrical kinks on dislocations [28], point defects [26] and impurities [29] and/or from the reaction products of dislocations [30]. On the other hand, D3 and D4 lines is generally thought to be related to electronic transition within dislocation cores [31]. In addition, it has been suggested that the D3 line most likely is a phonon-assisted replica

of D4 [31].

New lines D5 and D6 emerge when high-temperature, low-stress deformation is followed by low-temperature, high-stress deformation. [26] propose that line D5 is due to straight dislocations and D6 is due to stacking faults. [26] also suggest that D3/D4 photoluminescence is much more characteristic of the dislocations themselves than the D1/D2 emission lines. [32] state that D5 is correlated with electron-hole recombination at localized centers on separate partial dislocations. After annealing at moderate temperatures ( $T > 360^{\circ}\text{C}$ ) the new lines merge into D4 [32].

Both [24] and [26] studied plastically deformed silicon made by the Czochralski process (Cz-Si). [15] studied dislocations in multicrystalline silicon (mc-Si) and found similar lines with the entire set of D-lines shifted with around 10meV, presumably due to a strain field. Using a laser annealing technique [33], introducing dislocations on a Cz-Si wafer, confirm the band location of D1-D4 from [26] in [15]. A principal difference between dislocation D'-lines in mc-Si versus D-lines in Cz-Si is a substantial broadening in regards to energy (60-70meV at 77K) of the D1'/D2' lines observed in mc-Si [15].

Cz-Si [24]	D1 0.812eV	D2 0.875eV	D3 0.934eV	D4 1.000eV
mc-Si [15]	D1' 0.80eV	D2' 0.89eV	D3' 0.95eV	D4' 1.00eV

Table 3: Energy positions of dislocation D-lines in Cz-Si and D' bands in mc-Si

Photoluminescence mapping in [15] of the 0.78eV (0.8eV) band intensity reveal a linkage to areas of a high dislocation density. This band should also be visible in room temperature [15]. [15] also reveal a linear dependence of the band-to-band photoluminescence intensity and minority carrier lifetime across entire multicrystalline-Si wafers.

Dislocation related lines (D-lines) has been observed in low temperature photoluminescence spectra from the regions which included the intragrain defects. [27] concluded that grain boundaries are not active recombination centers. [27] also show a TO-phonon replica of the boron bound exciton at 1.093eV. Intensity of boron bound exciton from the long lifetime regions was higher than that from the short lifetime regions. D-lines reported by [26] are in a short lifetime region. For a long lifetime region, [27] observe a peak at 1.00eV which is not the D4 line, but the zone center optical phonon sideband of the two-hole transition in the boron bound exciton [3]. [34] conclude that a relatively low contamination level of dislocations in the order of 10 impu-

urity atoms/mm of the dislocation length produces D1 defect luminescence at room temperature and also degrades both the band-to-band luminescence and minority-carrier diffusion length. [35] argue that the D1 and D2 lines can be related to transitions via deep centers. In particular, D2 can be explained by a transition between a deep center and the three dimensional band of the semiconductor, while D1 transition is between a deep level and the dislocation one-dimensional bands. For both the transition is asymmetric. The deep levels are most probably located in the dislocation vicinity, which makes these lines sensitive to the local dislocation environment. Thus their radiation intensity is susceptible to gettering of the impurities.

It is believed that the intra-grain defects observed in the photoluminescence mapping are dislocations decorated with the heavy metals [27]. [8] found that if the contamination level is too low, or too high (dislocation decorated by metal silicate precipitates) the defect photoluminescence band vanished in room temperature. However, a relatively low contamination level of dislocations, in the order of 10 impurity atoms per micron of the dislocation length produces distinguishable defect band luminescence [8, 34].

[36] conclude that defects are metal contaminated dislocation clusters which originated from small angle grain boundaries. [36] study origins of the defects by low temperature photoluminescence spectroscopy, electron backscatter diffraction pattern measurement and the etch-pit observation. [35] demonstrate three areas of a sample with only D3 and D4 present, and conclude that this is due low concentration of metallic impurities.

#### 1.4.2 Impurities

Diffusion of transition metals into silicon crystals result in a variety of different electrically active levels in the forbidden bandgap. Impurities is also known to create precipitates inside a silicon crystal, which change the photoluminescence spectra compared to interstitial impurities.

There are several units of impurities in silicon that's commonly used. Examples are: ppbw (Parts Per Billion by Weight), ppba (Parts per Billion Atomic ) and atoms/cm<sup>3</sup>. To convert from ppbw to atoms/cm<sup>3</sup>, the following equation can be used:

$$\text{atoms}/\text{cm}^{-3} = \frac{10^{-9} [\text{ppbw}] \cdot N_A \cdot [\text{density(Si)}]}{[\text{atomicmassofelement}]} \quad (25)$$

where  $N_A$  is Avogadro's number, density(Si) is in g/cm<sup>3</sup>, and atomic mass is in g/mol. So, for boron

$$\frac{atoms/cm^{-3}}{ppbw} = \frac{10^{-9} \cdot 6.022 \cdot 10^{23} [mol^{-1}] \cdot 2.3290 [g \cdot cm^{-3}]}{10.811 [g/mol]} = 1.3 \cdot 10^{14} atoms \text{ } cm^{-3}$$
(26)

and phosphorous

$$\frac{atoms/cm^{-3}}{ppbw} = \frac{10^{-9} \cdot 6.022 \cdot 10^{23} [mol^{-1}] \cdot 2.3290 [g \cdot cm^{-3}]}{30.97376 [g/mol]} = 4.5 \cdot 10^{13} atoms \text{ } cm^{-3}$$
(27)

To convert from ppba to ppbw

$$ppbw = [ppba \text{ element}] \frac{[atomicmassofelement]}{[atomicmassofSi]}$$
(28)

so that 1 ppba boron in silicon is

$$ppbw = \frac{1[ppba] \cdot 10.811[g/mol]}{28.0855[g/mol]} = 0.385$$
(29)

and 1 ppba phosphorus

$$ppbw = \frac{1[ppba] \cdot 30.97376[g/mol]}{28.0855[g/mol]} = 1.103$$
(30)

### 1.4.3 Atom impurities

Early work done by [3] compare intrinsic silicon from the Czochralski process with doped silicon. [3] do extensive photoluminescence study with doping atoms As, P, Sb, Bi, B, Ga, In and Al. The high intensity transverse optical lines occur at 1.0907eV, 1.0916eV, 1.0921eV, 1.0888eV, 1.0924eV, 1.0914eV, 1.0835eV and 1.092eV respectively with the different doping atoms present. Impurities like carbon complexes with many impurities in silicon, resulting in a large variety of photoluminescence centers. Detected complexes are another C atom, one oxygen atom, one N atom, one Ga atom, the four-lithium atom complex, beryllium and numerous radiation damage centers, especially involving oxygen [14]. See appendix 7 for energies.

Doping atoms give rise to different characteristics in the photoluminescence spectra as well. Boron doping exhibits a line right around 1.15 eV (figure 80). That particular peak is less than 1 % of the intensity compared to its TO phonon replica, but the TO phonon replica can be harder to detect due to a strong luminescence from the silicon itself, and bound excitons with similar energies. Phosphorous doping give rise to a line just below the boron

line, and have a similar relative intensity to its TO phonon replica (figure 81).

Some impurities does not result in any specific photoluminescence spectra, like interstitial chromium [23]. Atleast not for wavelengths up to 1800nm. However, chromium bound with a boron atom can be identified as a peak around 0.85eV where the intensity increase linearly with laser power [23, 6]. Photoluminescence from another impurity, titanium, has been observed around 2.85eV in 4H silicon carbide by [7], and in 6H by [37] at 2.79eV, 2.82eV and 2.86eV named ABC lines (figure 85). These energies are far beyond that of the silicon bandgap, and can in cases described above, be uniquely identified.

Many of the other identified impurities are located just below the silicon bandgap in the photoluminescence spectra. Spectra for a silicon sample with a low amount of impurities can be seen in figure 79. Copper doping of silicon crystals results in an intense emission at 1.014eV [38]. [32] study Cu doped Si and also observe a shoulder on the D1 line which presumably arises from Cu precipitates at the dislocation.

Another important impurity is iron. [4] observe a spectrum of 0.735eV, which relate to a complex defect containing iron. Here the sample was introduced with Fe atoms into a float-zone silicon crystal (PL at figure 82). An earlier study [5], observe a luminescence spectra around 1.07eV in boron-doped, iron-diffused crystalline silicon and suggest the source is Fe-B pairs. Interstitial iron Fe, is about 10 times more effective as a recombination center than Fe-B pairs by low-level lifetime measurements and therefore reduces the minority carrier diffusion length more strongly (PL at figure 83) [39].

Recent work in [19] show that micro-photoluminescence is an excellent tool for identifying metal precipitates in silicon as seen in figure 18. Iron images in [40] reveal internal gettering of iron to grain boundaries and dislocated regions during ingot growth. Distinct spots, where detected with spot size as small as  $1\mu\text{m}$  with particularly low band to band photoluminescence. Precipitates from Fe and Cu are detected due to reduced band to band recombination intensity. Iron in silicon also affect the defect photoluminescence [19].

#### 1.4.4 Impurity interaction with dislocations

Investigation in [41] show that transition-metal contamination plays an important role in the production of D-band luminescence from silicon samples containing either epitaxial stacking faults or oxidation-induced stacking faults. [33] found that Cu doping resulted in reduced intensity of D1 and D2, and the intensity of D3 and D4 become very small. [32] demonstrate that

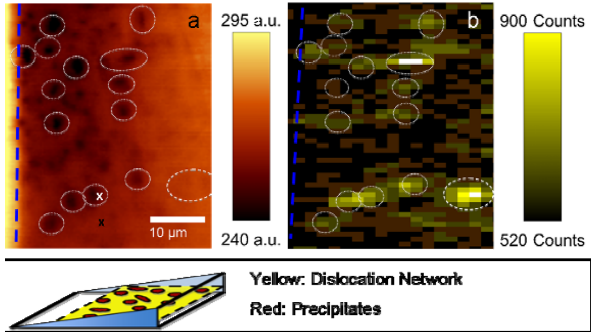


Figure 18: Bottom: Scheme of the sample preparation with the polished angle. Top: A Intensity of the BB PL peak at room temperature (a), and of the iron X-ray K $\alpha$  fluorescence (b) from [19]. The dislocation network intersects the surface to the right of the dashed blue line. The white circles show recombination active precipitates.

a complete passivation of the D-band luminescence is achieved at higher Cu and Fe concentration when deliberately contaminating high purity silicon samples which contain dislocations. However impurities like Ni, lead to no detectable changes in the spectrum [32]. D-band recombination in Si is found to be independent of impurities trapped at dislocations [32], and [30] concluded that metallic impurities don't seem to be related to D1 and D2 luminescence. Even so, it is still generally accepted that metal impurity influence it. Metal precipitation at crystal defects during the crystal growth can clean grains from impurities, and thus improve the performance as suggested for iron in [42]. A recent example of interaction with defects is iron precipitates in [19], showing an enhanced defect photoluminescence at  $1.3\mu\text{m}$  (0.95eV). The same study show that copper contamination almost completely suppress the defect photoluminescence. This is in agreement with [33]. Supression of defect photoluminescence by high copper concentrations was also reported in [43]. Cu precipitates can be located by reduced intensity of the band to band photoluminescence peak, both in areas with dislocations, and without [19].

Electron hole droplets (EHD), free excitons (FE) and bound excitons (BE) localized on phosphorus atoms has been steadily observed in [44] with photoluminescence on samples with low-dislocated regions. When increasing dislocation density the FE, BE and EHD bands decrease sharply. This may be due exciton capture by dislocation lines D1,D2 and non-radiative recombination [44]. EHD photoluminescence intensity is highly dependent on the pumping power [21]. There is a linear dependence, and pumping with 3 mW

or less makes it hardly visible in [21] with spot size of  $1.5 \mu\text{m}$ .

D1 line is shifted towards higher energies under uniaxial elastic deformation of samples with introduced dislocations or after their annealing in oxygen at  $750^\circ\text{C}$  [45]. Room temperature mapping of the  $0.77\text{eV}$  band is attributed to oxygen precipitates in thermally treated silicon made by the Czochralski process (Cz-Si) [46]. The increase of this band on the dislocation lines is due to the preferential precipitation of oxygen [46]. Later, [47] state that the deep-level emission from multicrystalline silicon with an intensity maximum at  $0.78 \text{ eV}$  at room temperature is different from that of the D1 line at low temperature. Furthermore, [47] suggest that the  $0.78 \text{ eV}$  emission is associated with oxygen precipitation, and that the intra-grain defects are dislocation clusters decorated with oxygen impurities in addition to heavy-metal impurities. [48] state that the origin of trap densities in multicrystalline silicon could be structural crystal defects, which are highly decorated with oxygen precipitates.

## 2 Experimental

### 2.1 Samples

All samples has been etched with an etch that consists of hydrofluoric acid, acetic acid, and nitric acid ( $\text{HF}:\text{CH}_3\text{COOH}:\text{HNO}_3$ ) in a volume ratio of 36:15:2 known as Sopori etch [49]. This is done in order to bring dislocations to the surface.

Name	Description	Feedstock
R6-Q3-210	Polysilicon, electronic grade, clean feedstock	Siemens process
ES1-Q3-201	Large amount of P and B, solar grade, dirty feedstock	From Elkem [50]
MH2-Q3-210	Same as ES1 with added Cr, solar grade, dirty feedstock	From Elkem [50]

Table 4: Samples

#### 2.1.1 R6-Q3-210

This sample is from a clean feedstock, with low amount of impurities. B, Al and Fe where measured by Glow-Discharge Mass Spectrometry (GDMS), O and C where measured by Fourier transform infrared spectroscopy (FTIR).

Impurity	ppbw	atoms/cm <sup>3</sup>
B	112.01	$1.45 \cdot 10^{16}$
Al	19.48	$1.0 \cdot 10^{15}$
Fe	nd	nd
C	2576	$2.26 \cdot 10^{17}$
O	1932	$8.87 \cdot 10^{16}$

Table 5: Impurities in R6 from [51]

The impurities that are not listed were not analyzed, and are expected to be present in very low levels (tenths of ppbw).

#### 2.1.2 ES1-Q3-201

This is a regular solar grade sample which originate from a compensated feedstock from Elkem Solar, from 90% ingot height. Impurities are given by

plot in [50]. Boron contaminants is between 550 and 700 ppbw, which corresponds to  $7.1 \cdot 10^{16}$  and  $9.7 \cdot 10^{16}$  atoms/cm<sup>3</sup> respectively using 25, and are homogenously distributed. Phosphorus is measured around 1200-1500 ppbw, which is  $5.4\text{-}6.8 \cdot 10^{16}$  atoms/cm<sup>3</sup>. Aluminum contaminants is just below  $2.6 \cdot 10^{15}$  atoms/cm<sup>3</sup>. Other contaminants like Ti and Fe have very low values: less than  $1.2 \cdot 10^{14}$  and  $3.8 \cdot 10^{14}$  atoms/cm<sup>3</sup> respectively. For the lighter atom impurities, O have  $1.7 \cdot 10^{17}$  atoms/cm<sup>3</sup> and C have  $6 \cdot 10^{17}$  atoms/cm<sup>3</sup> [50].

### 2.1.3 MH2-Q3-210

This sample is almost identical to ES1, but the sample also have extra chromium added. Chromium contaminants is between 2 and 5 ppbw [50] which corresponds to  $5.4 \cdot 10^{13}$  and  $1.3 \cdot 10^{14}$  atoms/cm<sup>3</sup> respectively using 25, but exact concentration might be a little lower due detection limit of the instrument.



## 2.2 Instrumentation

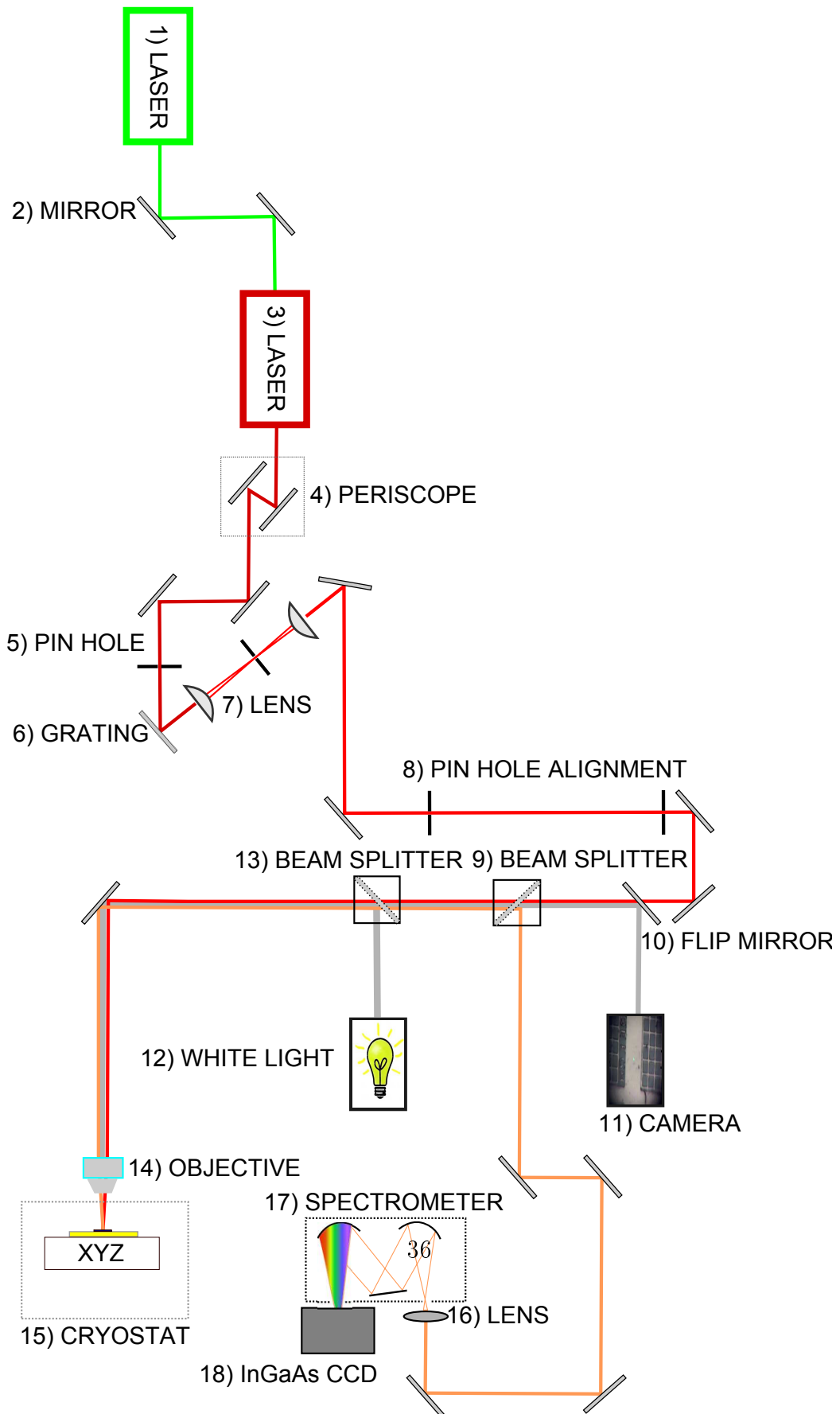


Figure 10. Instrumentation

### 2.2.1 Optical components

Optical components have been chosen to maximize luminescence light transmission in of wavelengths between 1.0-1.5  $\mu\text{m}$ . This is because the interesting parts of silicon luminescence is in this wavelength area (See table 7). The focusing lens in front of the spectrometer has above 90% transmission for these wavelengths, according to its specifications. As for the objective, it has 50X magnification, numerical aperture of 0.65, and a transmission curve that shows around 60% transmission for these wavelengths according to datasheet, with a working distance of 10 mm. Mirrors have very wide spectral coverage and are completely achromatic.

The beam splitter in figure 19:10 transmits 90% of light from 400 nm to 2400 nm and is only used to shine white light on the sample in order to see where on the sample the laser spot is hitting. The white light source can easily be made strong enough, so that 10% reflectance is sufficient. As for the beam splitter in figure 19:9, it splits the light 50/50 in transmission and reflectance. This beam splitter is optimized for 1100-1600 nm with a splitter ratio tolerance less than 15% over the entire wavelength range. However 50% of the luminescence light from the sample is still not entering the detection path, due to the split process.

#	Part	Product #	Manufacturer
1	532nm laser	YVO <sub>4</sub> Nd <sup>3+</sup>	Spectra physics
2	Metallic mirror	PF10-03-P01-10	Thorlabs
3	800nm laser	Ti-sapphire Model 3900S	Spectra Physics
4	Periscope	Two mounted mirrors	Thorlabs
5	Pin hole	ID12SS/M	Thorlabs
6	Grating	23M27	
7	Lens	AC254-150-B	Thorlabs
9	Beam splitter	BS018	Thorlabs
13	Beam splitter	BP208	Thorlabs
14	Objective	NT56-982	Mitutoyo
15	Cryostat	Janis ST-500	Janis Research Company
16	Lens	LB4330	Thorlabs
17	Spectrometer	iHR550 Imaging Spectrometer	Horiba Scientific
18	Camera	iDUS InGaAs Spectroscopy CCD 491-1.7	Andor Technology

Table 6: Lab setup optical components

### 2.2.2 Pumping wavelength

[25] report that small angle grain boundaries in multicrystalline silicon of  $1^{\circ}$ - $1.5^{\circ}$  show D3 and D4 lines, while  $2^{\circ}$ - $2.5^{\circ}$  show D1 and D2 lines. Comparing to data from electron beam induced current measurements show D1 and D2 lines to be correlated with shallow levels, while D3 and D4 appear in both shallow and deep levels [25].

The samples are pumped with a tunable Ti-sapphire laser, where a range of excitation wavelengths are available. A wavelength of 800 nm is chosen for excitation. This corresponds to an absorption depth of  $12 \mu\text{m}$  in silicon [20]. 800 nm is visible to the naked eye at high intensities, unlike larger wavelengths, which would make it much more difficult to align the setup, and make sure nothing is blocking the pathway. In the case of an imperfect filter in front of the spectrometer, 800nm (1.55eV) and the second order diffraction maxima at 1600 nm (0.775 eV), would be outside the most interesting wavelengths from silicon luminescence (see table 7 for silicon energy bands).

### 2.2.3 Spot size

For the setup given here, the spot size is around  $2 \mu\text{m}$ . This is given by the magnification of the objective, and the diameter of the incoming laser beam. With this spot size, it is possible to detect micro-defect, like iron precipitates [19]. The downside to having such a small spot size, is the potential buildup of electron-hole drops for small volumes [21]. This limitation can be overcome by using a larger wavelength, to excite a larger volume in the sample.

### 2.2.4 Laser intensity

A high signal to noise ratio, is desirable. This is achieved by exciting with as much laser intensity as possible. As long as issues with electron-hole drops and temperature are negligible, the intensity can be quite high. The maximum laser intensity achieved in this setup is 170mW measure right before entering the objective above the cryostat. With 800 nm pumping wavelength, and a spot size of  $\tilde{2}\mu\text{m}$ , the electron-hole droplet appear small compared to other signals like the TO-line when looking at the silicon luminescence (see results section). A high intensity is also desirable to be able to fill every available electron state. With low intensities, only the most probable states will be visible in the luminescence specter.

### **2.2.5 Temperature**

To achieve a high spectral resolution of the luminescence signal, it is needed to cool down the sample. Without cooling, the increased number of phonon states leads to energy broadening of the signal. This result in weaker signals getting 'drowned' in the strong signal peaks. To reach temperatures of about 10K, liquid helium is used for cooling. Liquid helium is introduced into the cryostat chamber, where it evaporates, drawing energy from its environment. The sample is on top of a sample holder, which is connected by copper wires to the cooling chamber, and a temperature readout. At such low temperatures, even weak signals as the ideally forbidden zero phonon recombination in silicon is visible [14].

### **2.2.6 Spectrometer**

The spectrometer has a fixed grating, in front of InGaAs camera. The grating is 76 mm x 76 mm, with a groove density of 300. The camera consist of a single array of pixels. The full array of pixels detect wavelengths with a range of 140 nm, with 0.1 nm sensitivity, and is operated at -75°C to minimize dark current noise. To measure a larger wavelength spectra than 140 nm, multiple measurements are needed. The camera spectral response is from 0.8 to  $1.7\mu\text{m}$ , which is suitable for silicon photoluminescence.

### 3 Results

Results have been corrected for dead pixels, measured dark current, and measured background noise unless otherwise specified. Grating is fixed at 300, and pumping wavelength is 800nm. Counts is a number given from the spectrometer which relate to the relative intensity detected by the pixel in the CCD.

#### 3.1 R6-Q3-210

This is the electronic grade sample, with a very low amount of impurities.

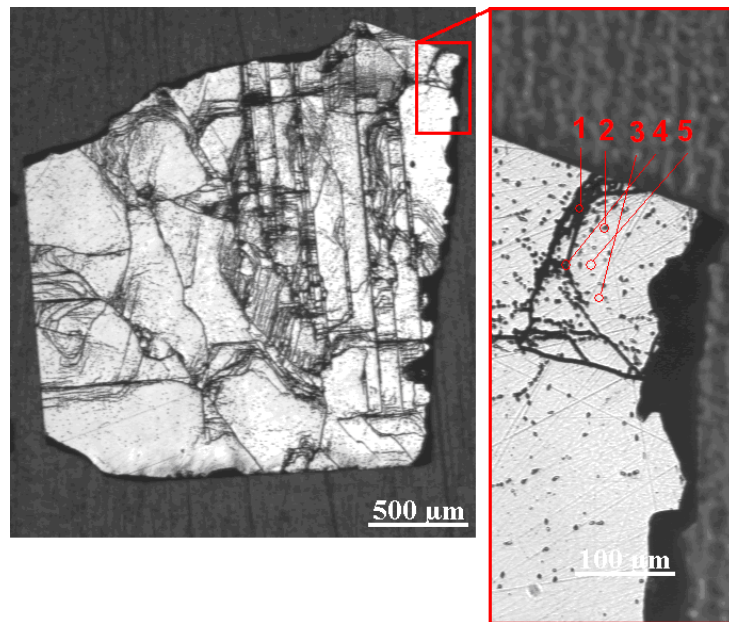


Figure 20: Sample R6-Q3-210 A picture taken using light microscope. Marked areas are spots where photoluminescence has been measured.

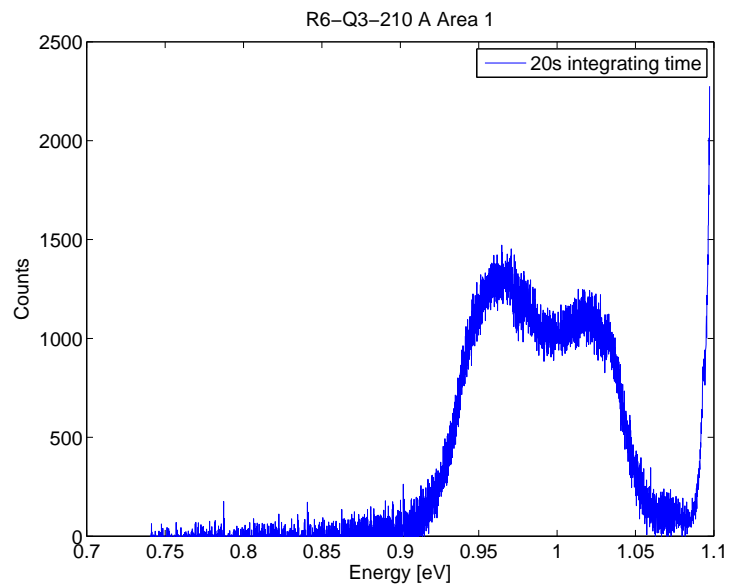


Figure 21: Sample R6-Q3-210 A pumped with 170mW at 10K in a dislocation line (Area 1 in figure 20).

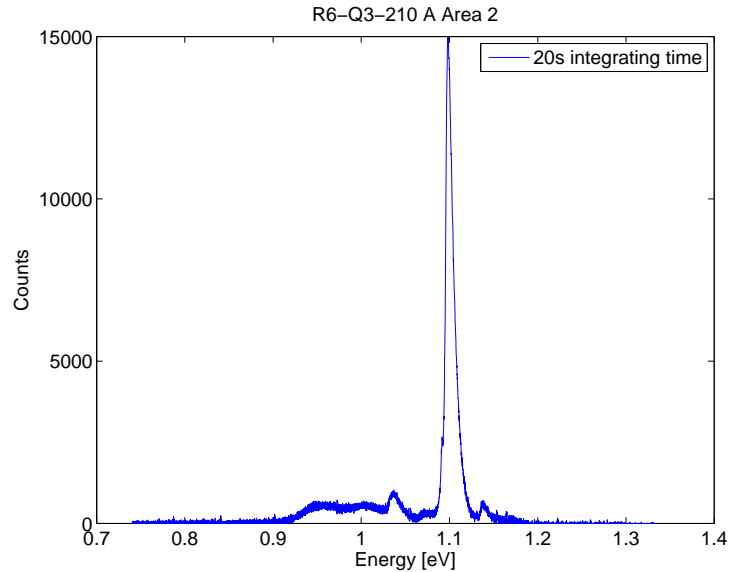


Figure 22: Sample R6-Q3-210 A pumped with 170mW at 10K in a dislocation dot (Area 2 in figure 20).

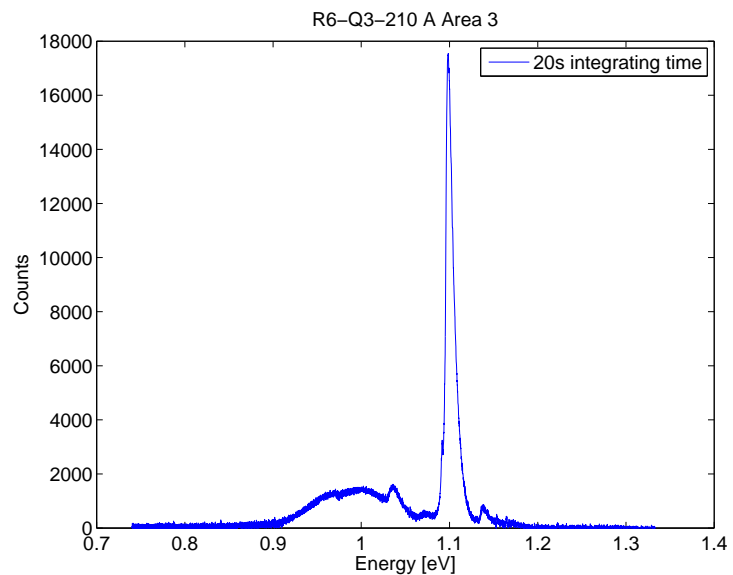


Figure 23: Sample R6-Q3-210 A pumped with 170mW at 10K in a defect free area (Area 3 in figure 20).

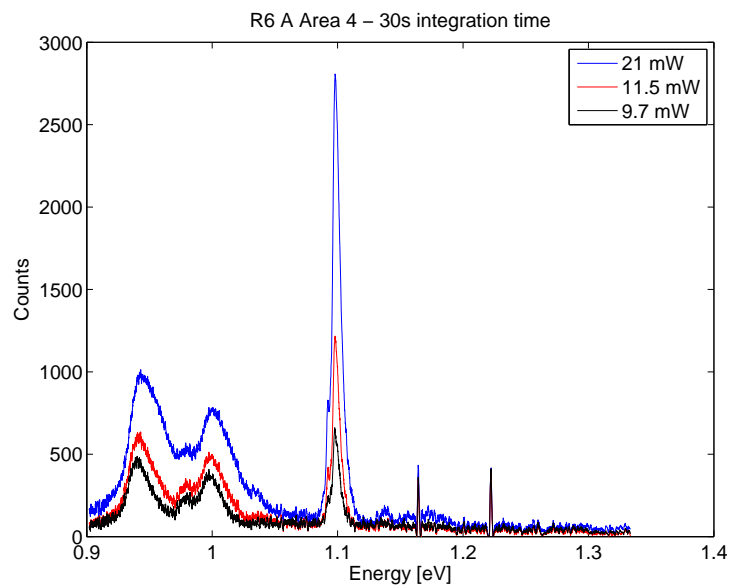


Figure 24: Sample R6-Q3-210 A pumped with different intensities at 22K in a grain boundary (Area 4 in figure 20).

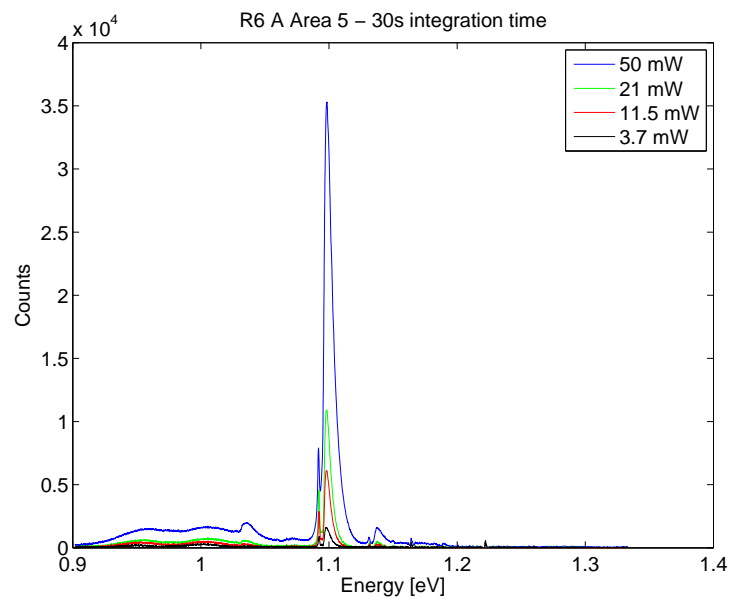


Figure 25: Sample R6-Q3-210 A pumped with different intensities at 22K in a defect free area (Area 5 in figure 20).

### 3.2 ES1-Q3-201

This sample is from a dirty feedstock, with large amount of P and B.

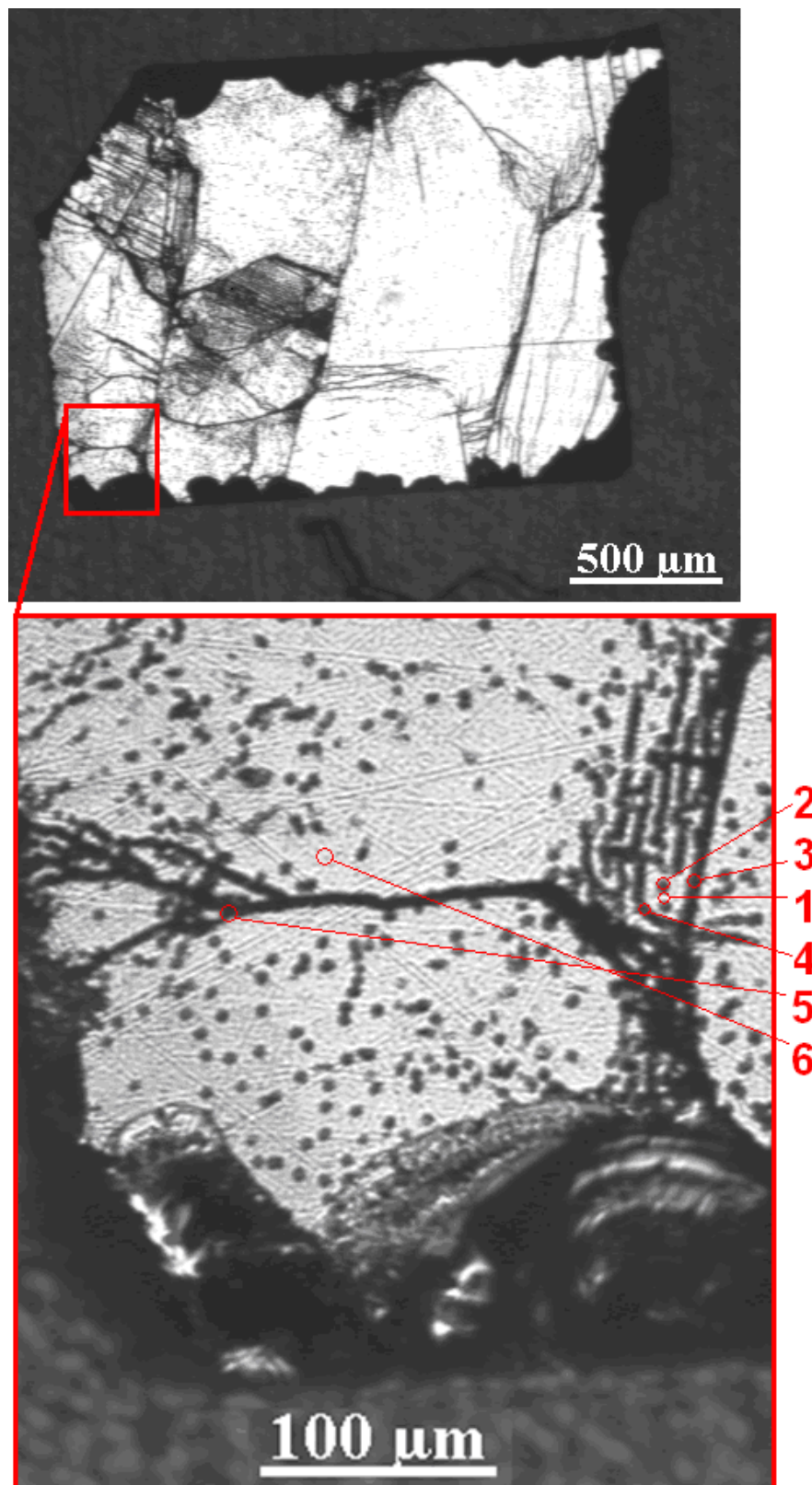


Figure 26: Sample ES1-Q3-201 C 210 Å picture taken using light microscope.  
Marked areas are spots where photoluminescence has been measured.

### 3.2.1 Room temperature

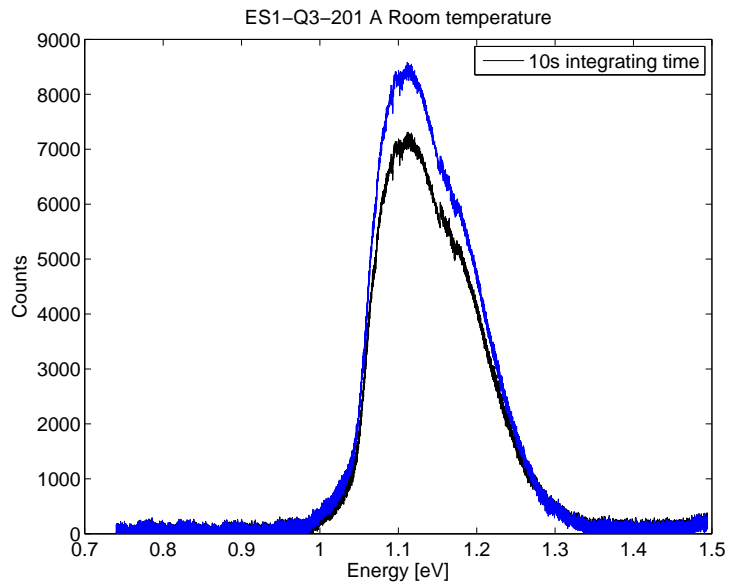


Figure 27: Sample ES1-Q3-201 A pumped with 26mW at 295K in a dislocation line (black) and in a defect free area (blue). An estimated dark current offset has been subtracted.

### 3.2.2 Low temperature

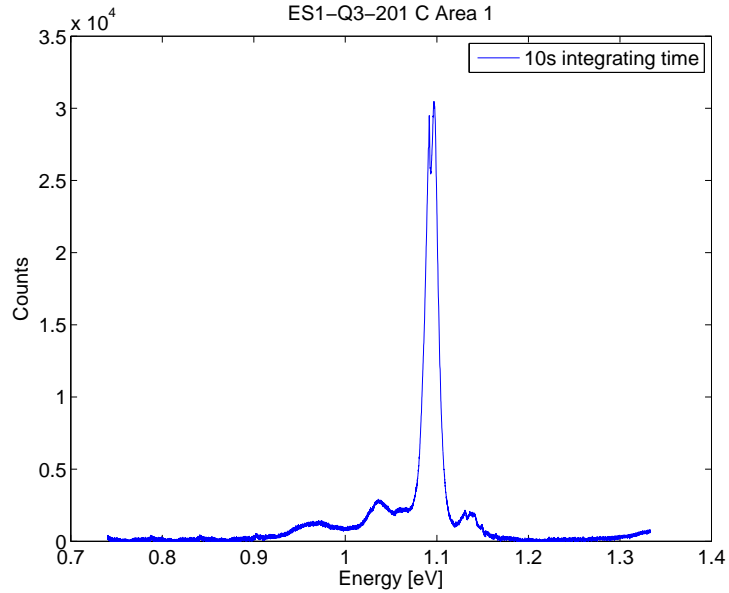


Figure 28: Sample ES1-Q3-201 C pumped with 170mW at 12K in a defect free area (Area 1 in figure 26).

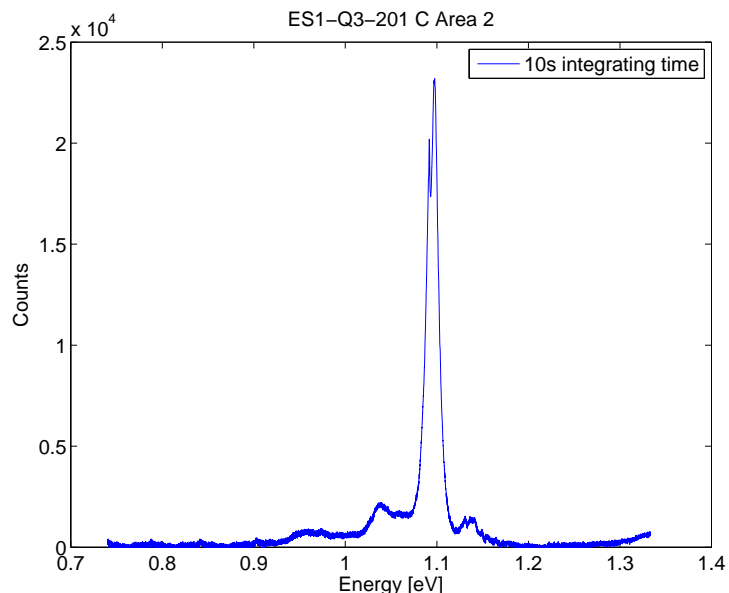


Figure 29: Sample ES1-Q3-201 C pumped with 170mW at 12K in a dislocation spot (Area 2 in figure 26).

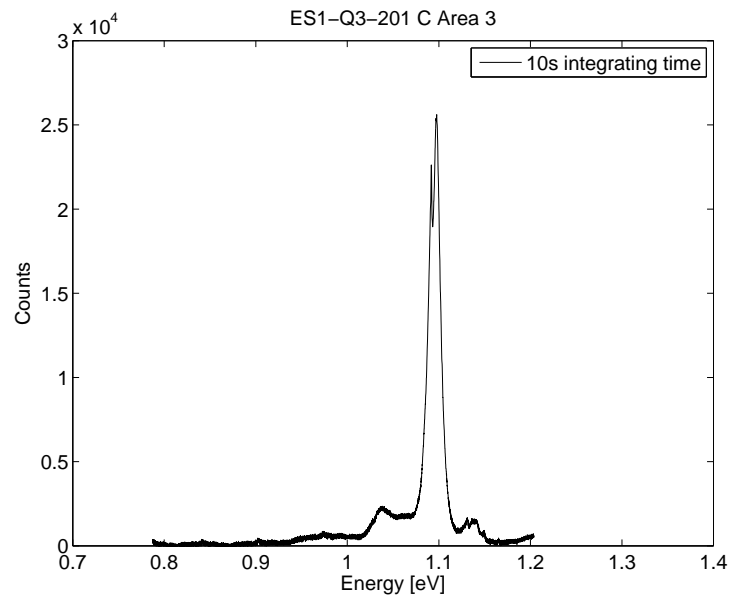


Figure 30: Sample ES1-Q3-201 C pumped with 170mW at 12K in a grain boundary (Area 3 in figure 26).

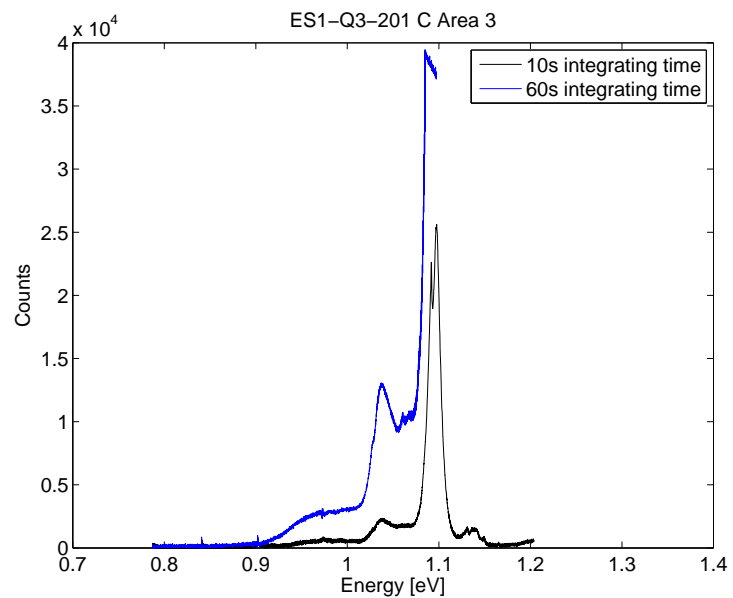


Figure 31: Sample ES1-Q3-201 C pumped with 170mW at 12K in a grain boundary (Area 3 in figure 26) with the result in figure 30 plotted as the black line.

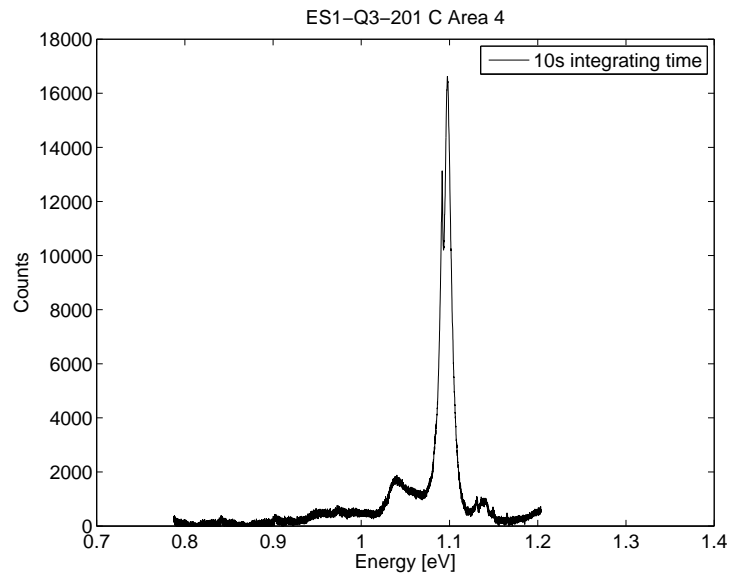


Figure 32: Sample ES1-Q3-201 C pumped with 170mW at 14K in a dislocation line (Area 4 in figure 26).

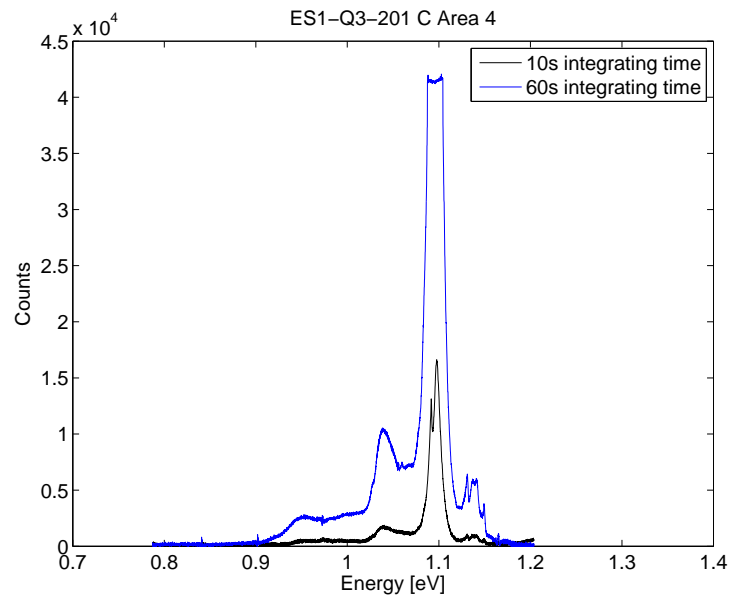


Figure 33: Sample ES1-Q3-201 C pumped with 170mW at 14K in a dislocation line (Area 4 in figure 26) with the result in figure 32 plotted as the black line. For 60s integration, the main TO line around 1.1eV is saturating the camera.

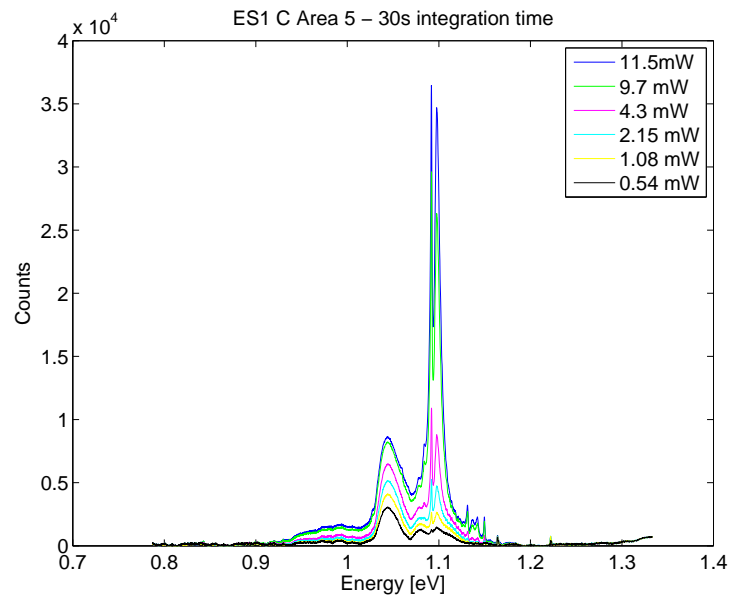


Figure 34: Sample ES1-Q3-201 C pumped with different intensities at 22K in a defect free area (Area 5 in figure 26).

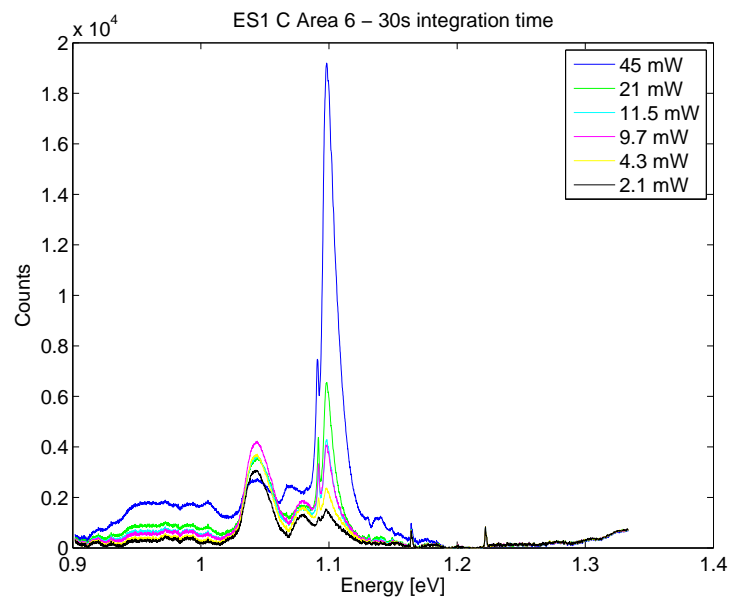


Figure 35: Sample ES1-Q3-201 C pumped with different intensities at 22K in a grain boundary (Area 6 in figure 26).

### 3.3 MH2-Q3-210

This sample is the same as ES1-Q3-201 except for added chromium in this one.

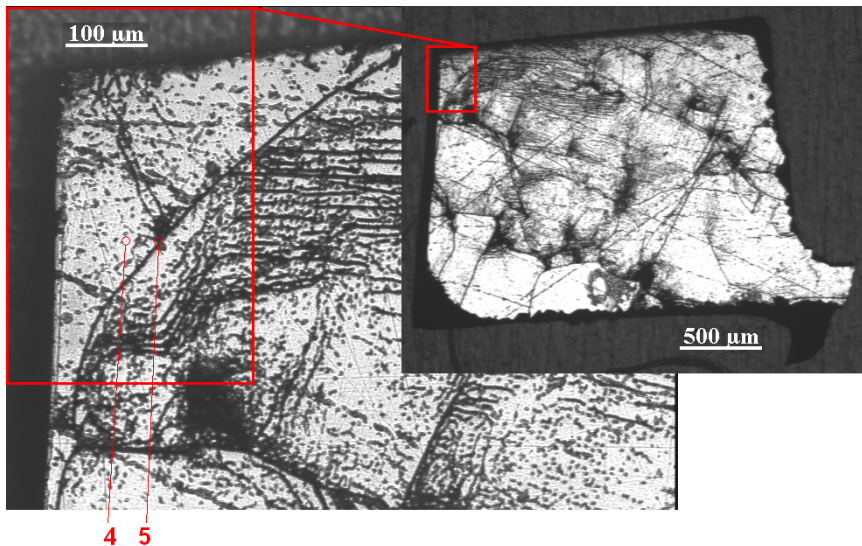


Figure 36: Sample MH2-Q3-210 B2 picture taken using light microscope. Marked areas are spots where photoluminescence has been measured.

### 3.3.1 Room temperature

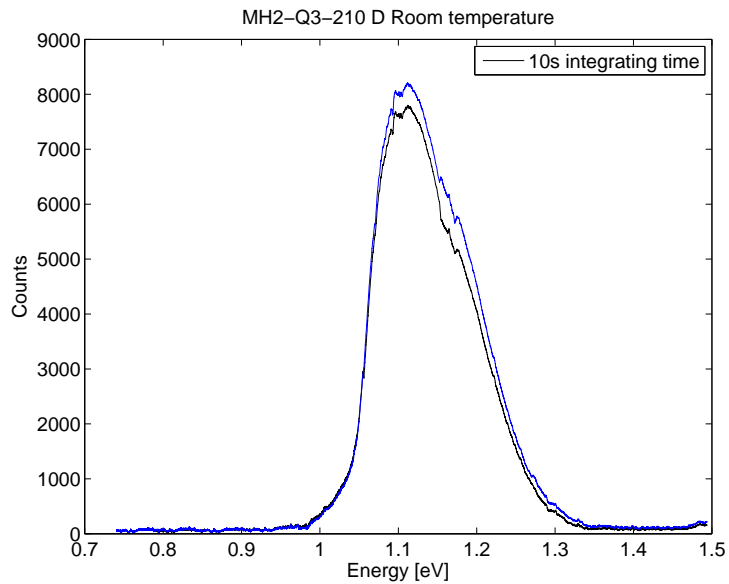


Figure 37: Sample MH2-Q3-210 C pumped with 26mW at 295K in a defect free area (blue), and in an area with dislocations (black). An estimated dark current offset has been subtracted, and results are Savitzky-Golay filtered for easier comparison.

### 3.3.2 At 70K

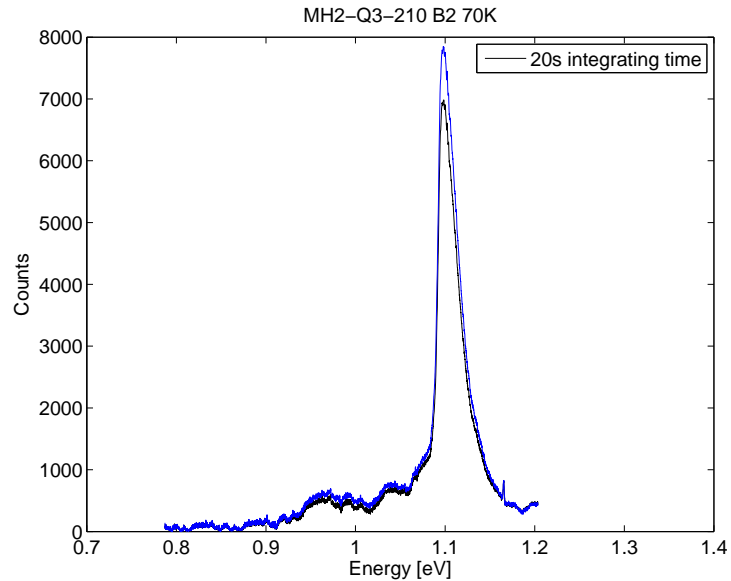


Figure 38: Sample MH2-Q3-210 D pumped with 170mW at 70K in a defect free area (blue), and in an area with dislocations (black). An estimated dark current offset has been subtracted, and results are Savitzky-Golay filtered for easier comparison.

### 3.3.3 Low temperature

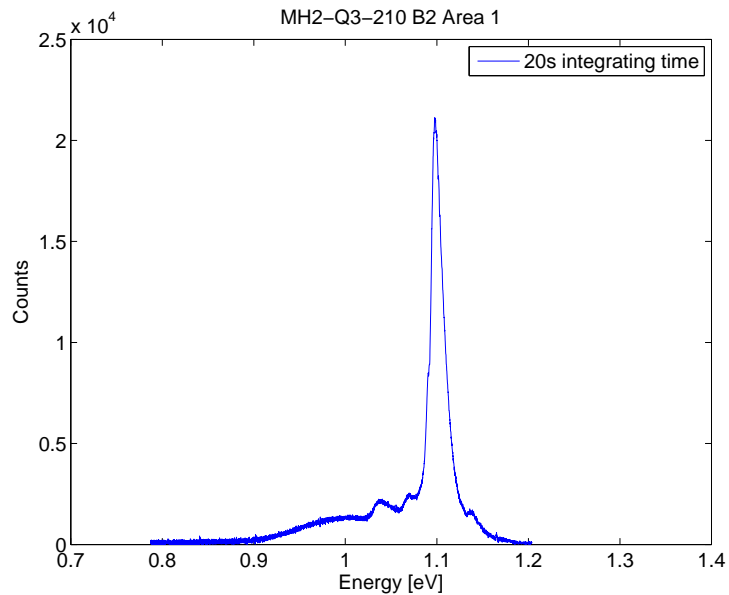


Figure 39: Sample MH2-Q3-210 B2 pumped with 170mW at 12K in a defect free area (Area 1).

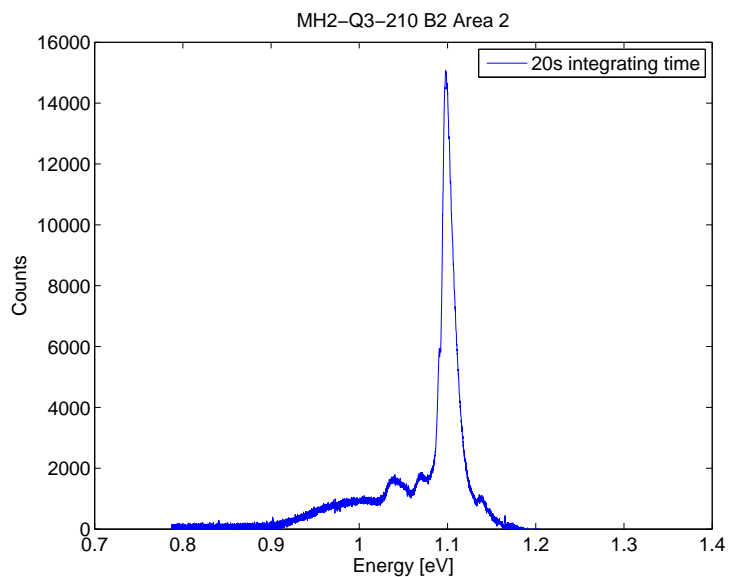


Figure 40: Sample MH2-Q3-210 B2 pumped with 170mW at 12K in a dislocation line (Area 2).

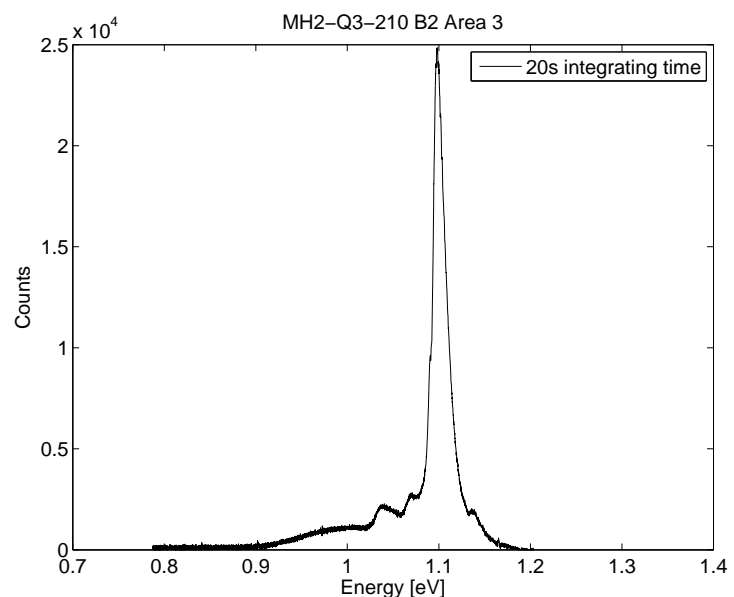


Figure 41: Sample MH2-Q3-210 B2 pumped with 170mW at 12K in a dislocation dot (Area 3).

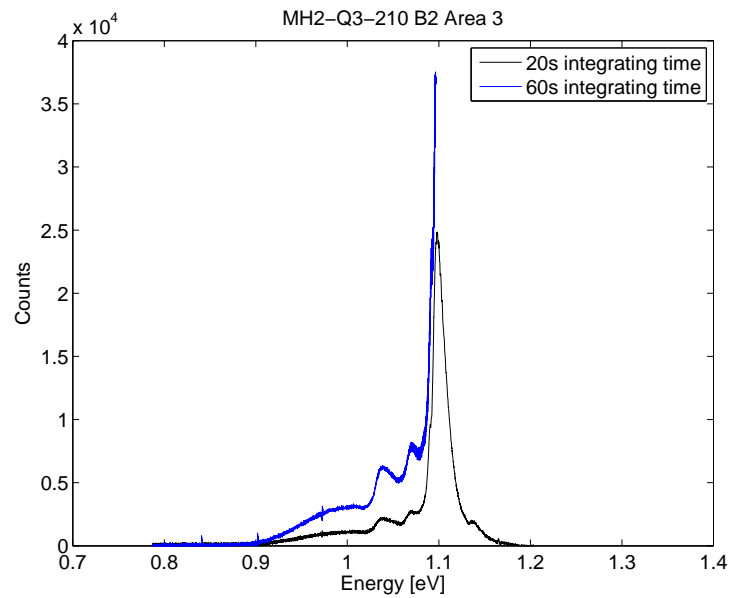


Figure 42: Sample MH2-Q3-210 B2 pumped with 170mW at 12K in a dislocation dot (Area 3) with 20s integration time (black) and 60s integration time (blue). The 60s integration time has an estimated dark current offset subtracted, in addition to measured dark current due to mismatched dark current measurement.

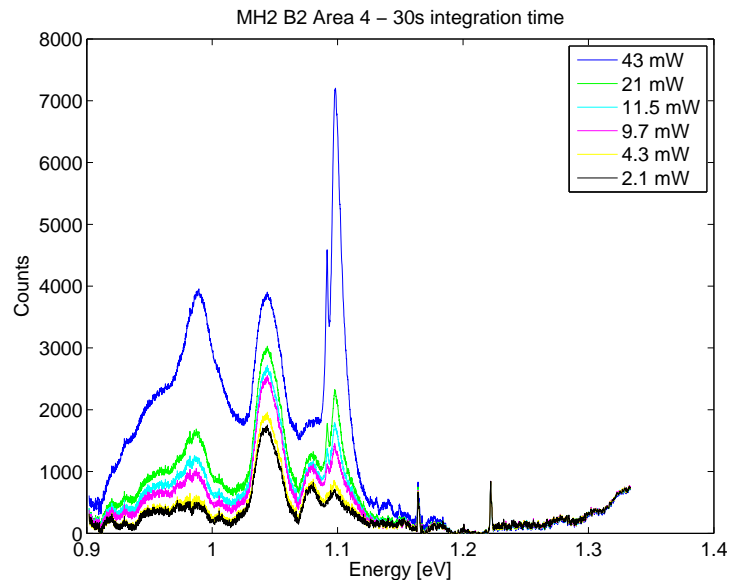


Figure 43: Sample MH2-Q3-210 B2 pumped with different intensities at 27K in a grain boundary (Area 4 in figure 36).

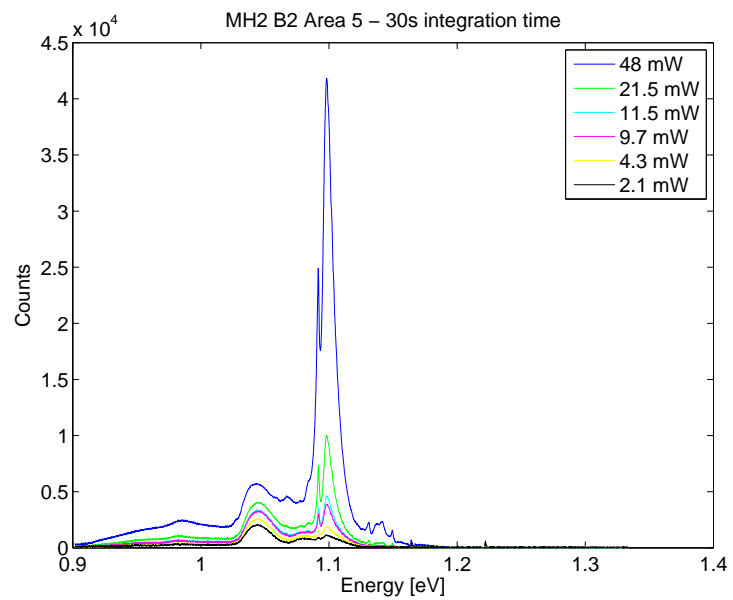


Figure 44: Sample MH2-Q3-210 B2 pumped with different intensities at 27K in a defect free area (Area 5 in figure 36).

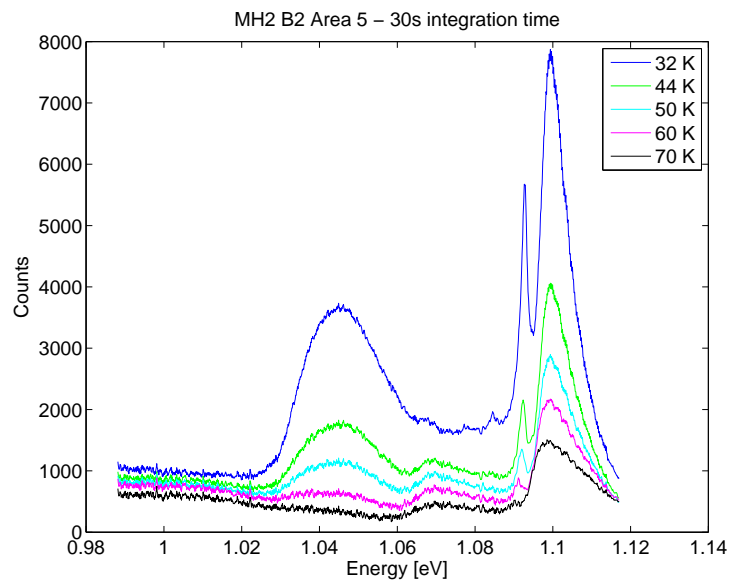


Figure 45: Sample MH2-Q3-210 B2 pumped with 21.5 mW at different temperatures in a defect free area (Area 5 in figure 36).

### 3.3.4 Line mapping

These results are a line mapping of different spots on the sample.

Positions 1-10 has en equally large distance in between them, with position 1 in figure 46 and position 10 in figure 47.

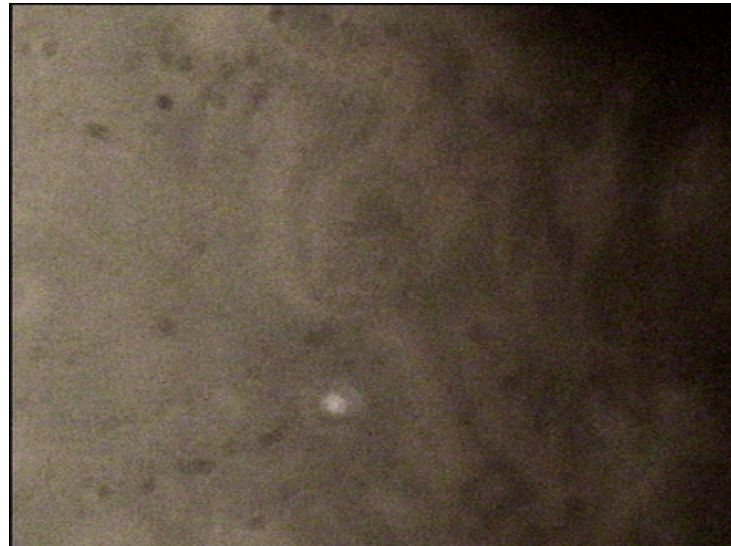


Figure 46: Sample MH2-Q3-210 B2 Line mapping end position. Picture is from the camera inserted into the detection path by use of a flip mirror, and sample illuminated by white light. The bright spot is reflections from the pumping laser.

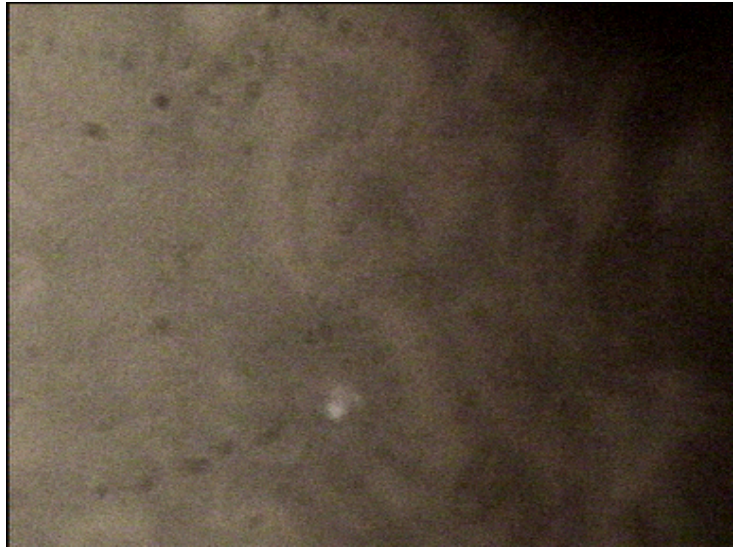


Figure 47: Sample MH2-Q3-210 B2 Line mapping end position. Picture is from the camera inserted into the detection path by use of a flip mirror, and sample illuminated by white light. The bright spot is reflections from the pumping laser.

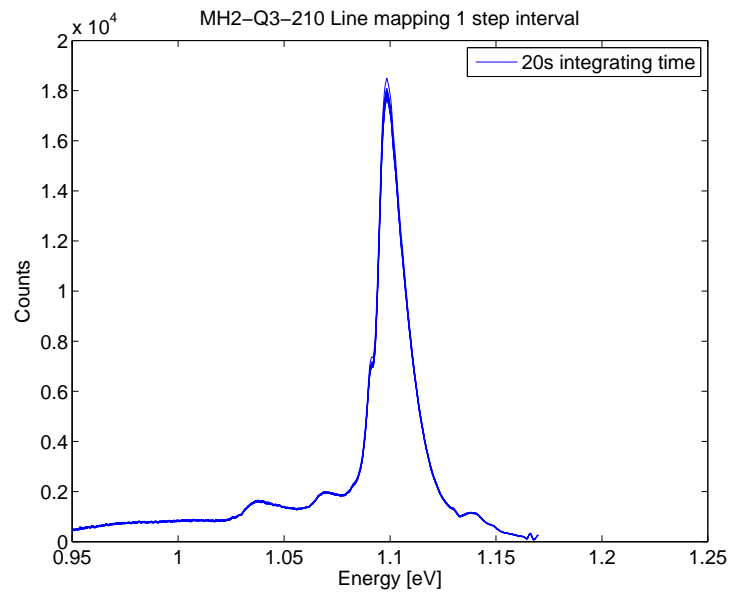


Figure 48: Sample MH2-Q3-210 B2 pumped with 170mW at 14K line map using 10 small steps.

Positions 1-20 has en equally large distance in between them, with posi-

tion 1 in figure 49 and position 20 in figure 50.



Figure 49: Sample MH2-Q3-210 B2 Line mapping end position. Picture is from the camera inserted into the detection path by use of a flip mirror, and sample illuminated by white light. The bright spot is reflections from the pumping laser.

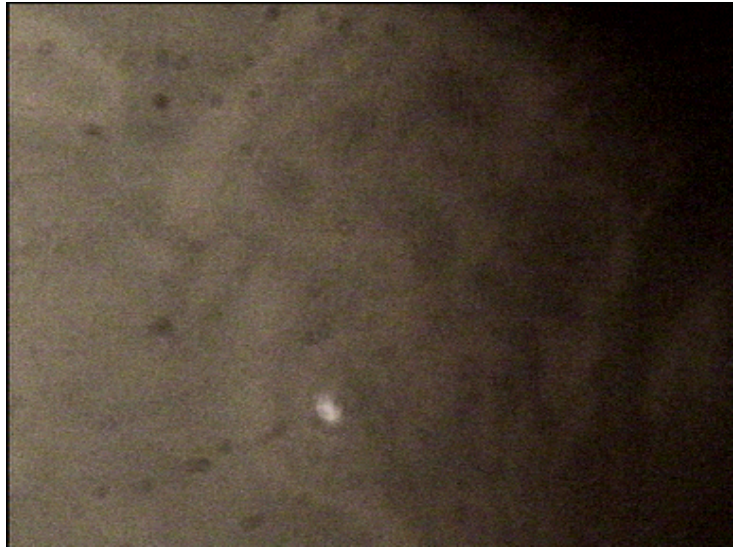


Figure 50: Sample MH2-Q3-210 B2 Line mapping start position. Picture is from the camera inserted into the detection path by use of a flip mirror, and sample illuminated by white light. The bright spot is reflections from the pumping laser.

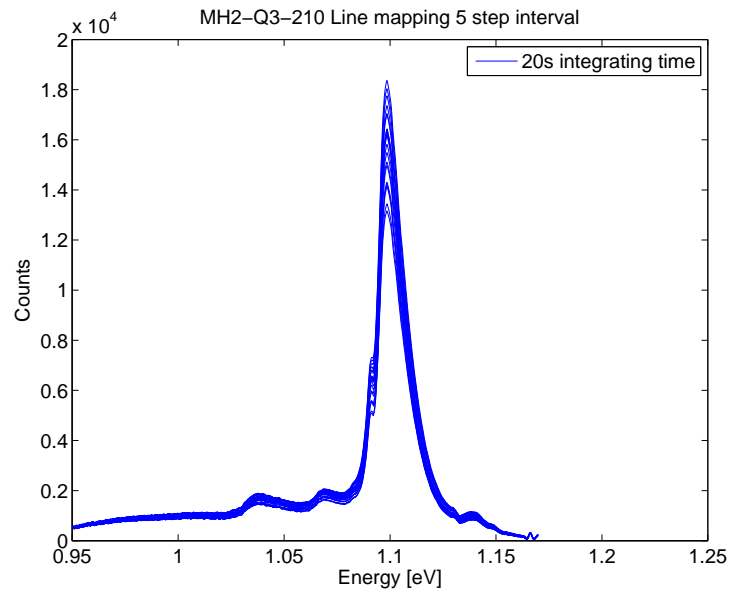


Figure 51: Sample MH2-Q3-210 B2 pumped with 170mW at 14K line map using 20 steps exactly 5 times larger than in figure 48.

## **4 Discussion**

## 4.1 Results plotting

In order to plot the results from the spectrometer, there are a few manipulations that's needed.

### 4.1.1 Disregarding defect pixels

By taking a spectra with the shutter closed, it is possible to measure the dark current coming from the camera. The dark current should be equally distributed across the pixels, based on the assumption that all pixels behave the same. For long integration time, this is not the case as seen in figure 52.

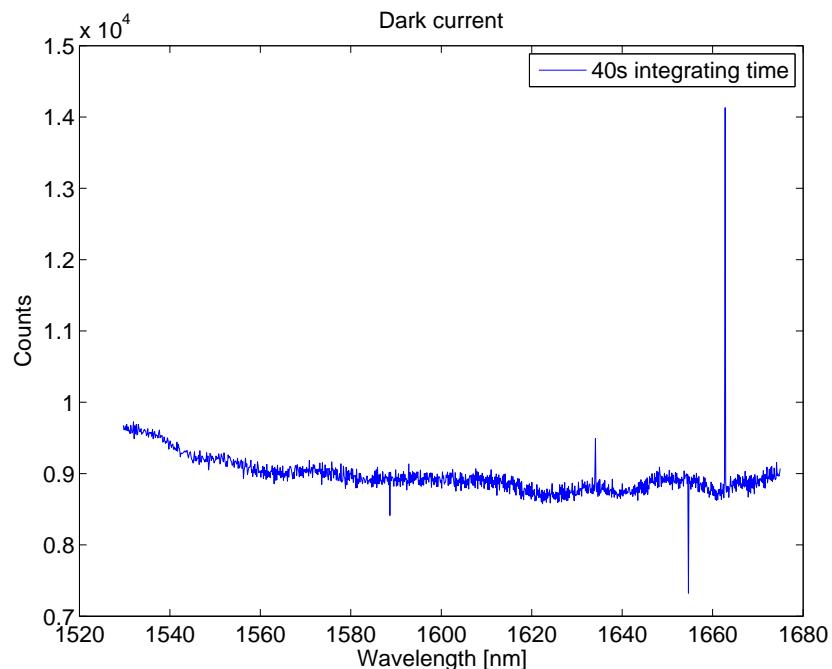


Figure 52: Dark current signal from the camera with defective pixels with shutter closed, and CCD at -75°C using a random center wavelength

To solve this problem, the four pixels standing out are disregarded, and the value of the neighbor pixel has been used instead. Matlab code for this is available in the appendix. Comparing the before and after clearly show how this is done:

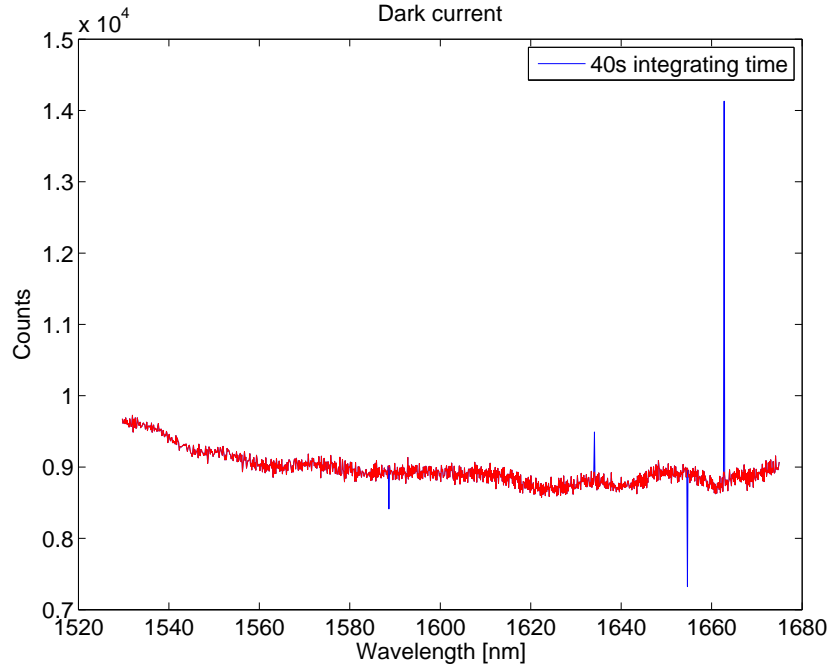


Figure 53: Dark current signal from the camera with defective pixel correction in red using a random center wavelength

The defective pixels are less apparent for shorter integration time, but still a problem:

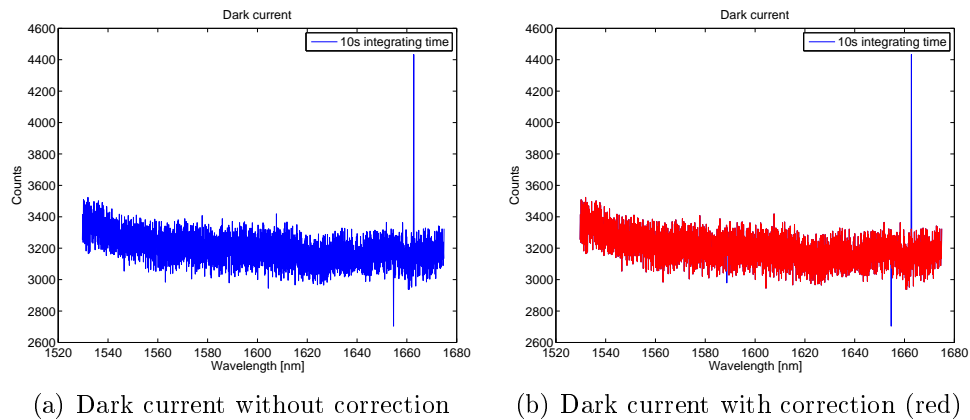


Figure 54: Dark current with 10s integration time using a random center wavelength

Dead pixel correction is performed in all results.

#### 4.1.2 Noise reduction

As seen in the previous section, there is a dark current offset present. Ideally, all pixels should behave exactly the same, and give rise to the same dark current offset. If all pixels behaved the same, and with the same variance in between measurements, it could simply be subtracted. This is not the case. The dark current is unevenly distributed over the pixel array, and needs to be measured by itself in order to remove it. The mean dark current noise shape is pretty much the same from measurement to measurement using the same CCD temperature. In addition to the mean offset, there is white noise elements.

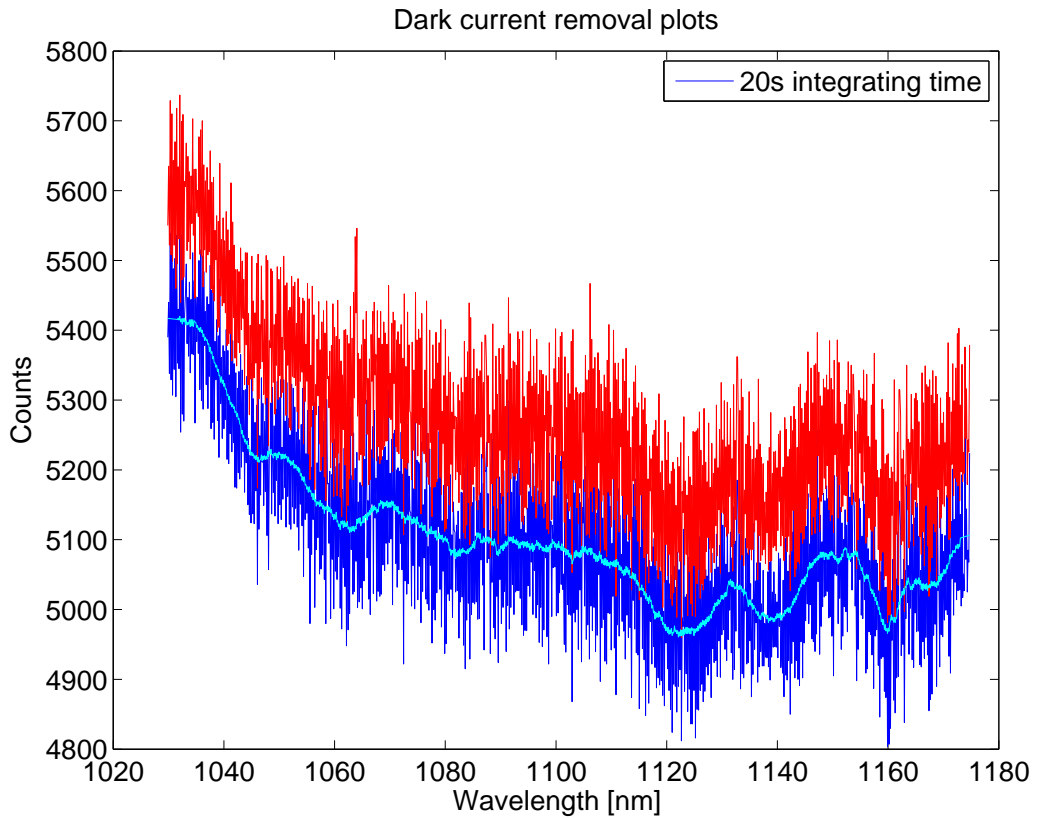


Figure 55: Dark current (blue) and dark current + background noise (red) with Savitzky-Golay filtered noise floor estimation (cyan)

By subtracting the mean offset found in the dark current noise measurement, only background noise and white noise would be left. The matlab code used to do this can be found in the appendix.

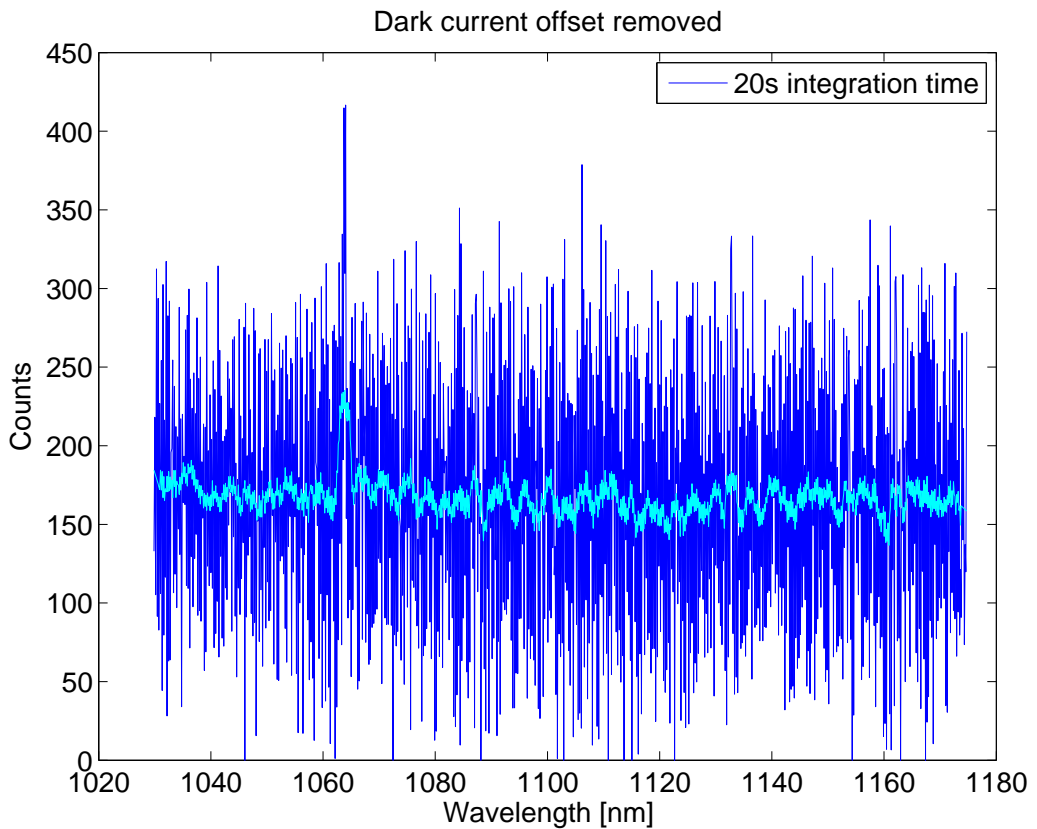


Figure 56: Dark current removed from background noise (blue), and Savitzky-Golay filtered signal (cyan)

It appears that the dark current noise is larger with the shutter open, compared to closed. But a more critical noise in the spectrum is a background signal around 1064nm. The spectrometer has a range of 140nm when using 300 as grating. It has proven difficult to align the system so that the entire array of pixels in the camera get an equally distributed light beam. And based on the noise level, the nm interval is chosen as 100nm, in order to remove the left hand side of the spectra when gluing different intervals together. This also avoid the problem of not hitting the entire array evenly. To get a full overview over the background noise, a full spectra was done, and glued together. This full spectra show that the artifact visible in 56 is the only background noise line visible in the wavelength area 800-1650nm.

### 4.1.3 Savitzky-Golay filtering

Savitzky-Golay filter (also called digital smoothing polynomial filter or least-squares smoothing filter), is a smoothing filter which essentially performs a local polynomial regression on a series of values equally spaced. This filter is chosen because of the large frequency span of the signal. Although Savitzky-Golay filters are more effective at preserving the pertinent high frequency components of the signal, they are less successful than standard averaging FIR filters at rejecting noise [52].

## 4.2 Expected results

### 4.2.1 Sample from clean feedstock

Having carbon values around  $2.26 \cdot 10^{17}$ , it is possible that the two-carbon atom band is visible here also. Else this sample is expected to only show intrinsic values similar to [3] in so called 'good' areas due to low concentration of impurities. However, there might be precipitates and higher concentration of impurities at the grain boundaries and dislocations. Particularly heavy metals like Fe and Al can be detected here. It is expected that the band to band recombination from silicon show considerably lower intensity for these areas.

### 4.2.2 Phosphorus and boron doped samples

With fairly high concentrations of doping atoms, it's expected that lines attributed to phosphorous and boron atoms in the photoluminescence spectra is detectable. A previous study, on samples with similar doping concentrations can be found in [3]. [3] observe a line around 1.0924eV which is attributed to  $B^{TO}$ . Concentrations values for B in [3] are  $6 \cdot 10^{16} \text{ cm}^{-3}$ . Also observed is a phosphorus line at 1.0916eV, with  $8 \cdot 10^{16} \text{ cm}^{-3}$  phosphorus atoms. With ES1 and MH2 having similar B and P values, they are expected to show a similar behavior. (See figure 80 and 81 in appendix 4.3.4)

There is a photoluminescence line involving carbon bound to oxygen in Czochralski silicon known as the C-O band [14]. In [53], it was observed only in crucible grown silicon, but not in float zone. In the crucible grown silicon, the oxygen impurities where  $2 \cdot 10^{18} \text{ atoms/cm}^3$ , which is over ten times more than in ES1 and MH2. This makes it unlikely that any C-O complex luminescence will be strong enough to be detectable in these samples.

Another line involving carbon, is the two-carbon atom band [14]. This band has been detected in float-zone silicon with  $C = 9.7 \cdot 10^{16} \text{ cm}^{-3}$  after irradiation, together with the C-O complex line. The relative intensity between the C-O band and the two-carbon atom band in [14] show that the 969 meV band is close to 5 times larger than the 789 meV band. With both MH2 and ES1 having carbon impurities around  $6 \cdot 10^{17} \text{ cm}^{-3}$  it is possible that this line at 969 meV will be visible.

As for aluminum, [3] show a line at 1.09 eV called  $Al^{TO}$  in a sample with  $2 \cdot 10^{16} \text{ cm}^{-3}$  Al doping atoms. In ES1 and MH2, the Al impurities are 20 times less. In addition to a fairly low value of Al impurities, the  $Al^{TO}$  line is very close to the  $I^{TO}$ , which can make it difficult to detect, and not likely to show up in the results.

Fe bound with boron is also known to give rise to photoluminescence at 1.069 eV [5]. The sample used in the article had  $10^{13}$  to  $10^{16} \text{ cm}^{-3}$  boron doping concentration. The article doesn't mention how many Fe impurity atoms that's introduced into the sample, but it's done by high temperature diffusion, and assumed to be considerably larger than for all the samples in this study.

Based on the low values of Fe impurities in these samples, it's assumed that interstitial Fe won't have any effect on the photoluminescence bands. The same goes for Ti, which also have a very low amount present.

#### 4.2.3 Sample with added Chromium

This sample have the same impurity values as ES1, except for chromium. The closest comparison is samples used in [23]. Here, luminescence spectra was observed for chromium in an p-type sample. Interstitial chromium concentrations where between  $10^{14}$  and  $10^{16} \text{ cm}^{-3}$  in [23].

Chromium in an n-type sample doped with phosphorus atoms does not result in any luminescence, but chromium bound with boron show a clear line at 0.8432eV ( $\text{CrB}^0$ ). The reaction velocity for the formation of CrB pairs at room temperature depend on the boron concentration. For large ( $10^{15} \text{ cm}^{-3}$ ) boron content, the chromium-boron reaction reach saturation in less than a day after chromium diffusion [23].

There is enough boron atoms in MH2 to saturate chromium by forming CrB pairs. Chromium atoms are in the order of  $10^{14} \text{ atoms/cm}^3$  which is similar to that in [23]. Expected photoluminescence spectra is therefor expected to be similar. (See figure 84 in appendix). Only a small amount of the overall boron atoms will be bound to chromium, and there are also Fe impurities present in the sample, that can form bonds with boron. However, based on the low amount of Fe in this sample, those bonds are not believed to have any impact on the photoluminescence. It has been shown experimentally that neutral iron does not form FeB pairs in boron-compensated n-type silicon [54].

## 4.3 Results analysis

Comparison plots have been slightly filtered using weak Savitzky-Golay filtering to reduce white noise for easier comparison. The line map and bar plots are without this filtering.

### 4.3.1 Comparing different locations on sample R6-Q3-210

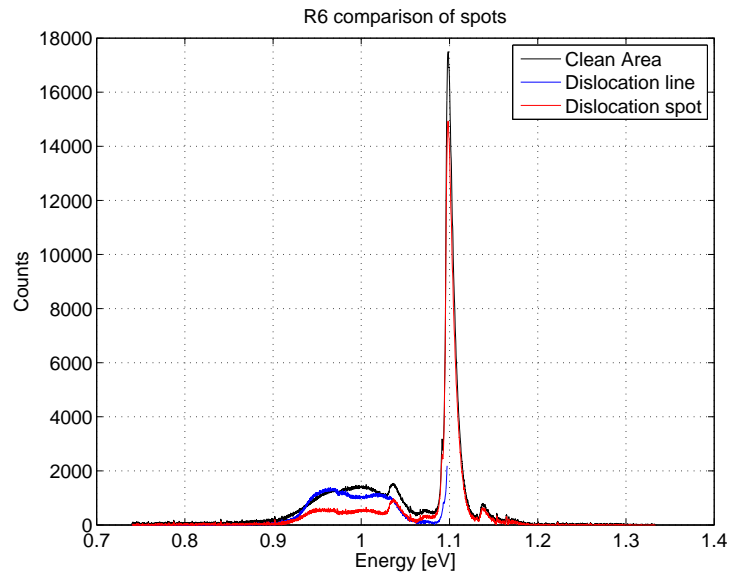


Figure 57: Comparison of different locations on sample R6-Q3-210 A from results in figure 23, 21, and 22.

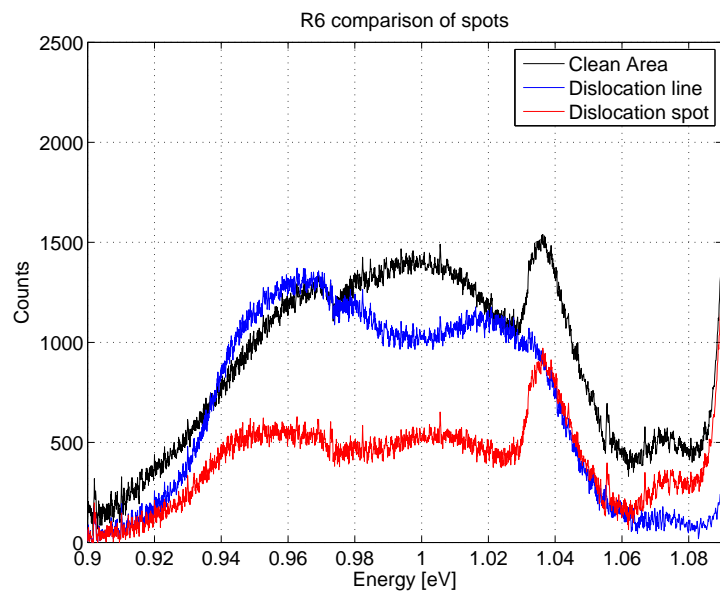


Figure 58: A closer look on differences in R6-Q3-210 A from graph in figure 57

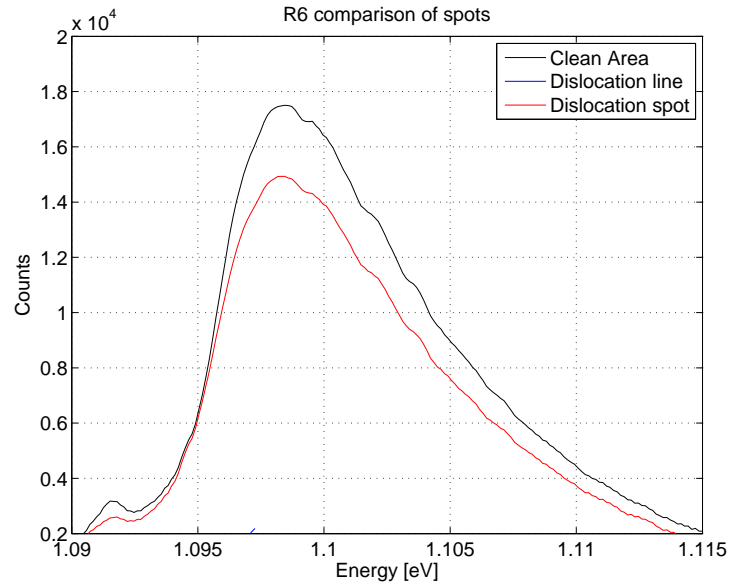


Figure 59: A closer look on differences in R6-Q3-210 A from graph in figure 57

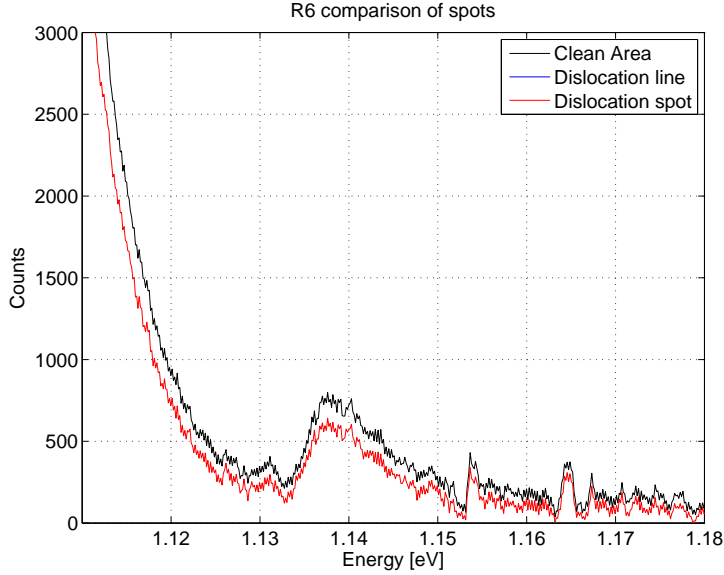


Figure 60: A closer look on differences in R6-Q3-210 A from graph in figure 57

The strong TO line and its replicas, has relative intensities similar to those found in [3]. Low impurity levels in the sample allows for comparisons with intrinsic characteristics from [3] (figure 79). Comparison show TO + 2 Zone center phonon at 0.968 eV, TO + Zone center phonon at 1.0315 eV, intervalley phonon replicas around 1.07 eV, TO at 1.097 eV and TA at 1.365 eV. It is also possible that the peak at 1.54 eV is the ideally forbidden no phonon peak, but it is very close to the noise floor, and cannot be unequivocally identified. The intensity differences can be due to small differences in focus of the excitation light, or other small alignment changes when physically moving the sample.

TO + Zone center phonon line have 7 % relative intensity to TO in [3], when pumped with 7 W from a mercury arc on to an etched surface of intrinsic silicon. The relative intensity of TO + Zone center phonon line is 6 % for both the dislocation line, and dislocation dot. The difference here could be due to a bound exciton line at 1.092 eV also influencing the TO line. This peak at 1.092 eV is attributed to the TO phonon assisted Si:B bound excitons [55]. The Si:B free exciton would be at 1.150 eV, with 10% intensity relative to the TO. This line could be present, by judging the R6 results, however due to the noise level, it is hard to know for sure, but the relative intensities would be in the same order of magnitude as in [55] if it is in fact the free exciton line.

[56] describe a relation between  $B^{TO}(\text{BE})/I^{TO}(\text{FE})$ . The ratio in R6 is close to 0.1, which in [56] correspond to  $N_A - N_D \approx 5 \cdot 10^{11} \text{ cm}^{-3}$ . R6 is in the

order of  $10^{16} \text{ cm}^{-3}$ , and with excitation intensity (150 mW in [56]), and temperature (liquid helium temperatures in [56]) being similar, there is clearly some mismatch between the samples. Other differences is [56] using an Ar ion laser, and having as spot size of 1mm. This should, however, not affect the ratio in between the two lines, unless the smaller volume give rise to other types of recombination, like electron-hole drops, or non radiative recombination. One possible explanation is that [56] where looking at compensated high purity CZ-Si and FZ-Si, and that the relation is invalid for mc-Si. Specifically [24] report a decrease in bound exciton intensities when nearing dislocation areas, which could account for the mismatch to results in [56].

There are some lines present, that doesn't relate to intrinsic silicon, like the line at 1.0 eV. In addition, there is an increased intensity of TO + 2 zone center phonons which is expected to be 1 % of the TO line [3]. But this appear to be  $\tilde{7}$  % in the R6 dislocation line , and  $\tilde{3}$  % in the R6 dislocation dot. These are likely to originate from dislocations. D3 and D4 are known to appear at 0.934 eV and 1.00 eV respectively at 4.2 K in CZ-Si [24]. D4 has not been observed without D3, and vice versa, and D3 is considered to be a phonon replica of D4 [31]. In addition, [46] report a broad background emission reaching from 0.9-1.0 eV with D3 and D4 present. In the R6 results, on the dislocation dot, there's signs of D3' and D4' lines at 0.95 eV, and 1.0 eV respectively. This corresponds to measurements on mc-Si with a temperature of 77K, from [15], which reports a shift in the energies when comparing CZ-Si and mc-Si. The D3 line is larger than D4, which can be explained by the small energy differences between the three, momentum conserving TO phonons, which cause three replicas slightly different in the their energy [35].

If, in fact, it is the D3' and D4' lines in the result, D1 and D2, which also are attributed to dislocation areas are completely missing. [34] state that a relatively low contamination level of dislocations in the order of 10 impurity atoms/mm of the dislocation length produces D1 defect luminescence at room temperature. [35] state that D1 and D2 are most probably caused by the interaction of the dislocations with background metallic impurities. This is a probable reason, due to the low level of metallic impurities in R6.

When pumping at lower intensities, the relative intensity of D3' and D4' compared to TO is higher. This is most likely caused by the D3' and D4' lines reaching saturation for high intensities, effectively halting the rise of these bands, for higher pumping light intensities. These lines are also considerably smaller for a defect free area. The peaks from this area are likely to arise from defects below the surface.

There are two peaks observed at 1.04 eV and 0.98 eV. The 0.98 eV line, is only distinguishable in figure 24, but is likely to be present in the other results

as well, based on the shape of the dislocation related luminescence, which has a contribution to the photoluminescence in between D3' and D4' that can not be explained by phonon replicas of the TO line alone. These lines are known as R1BB and R2BB [57, 9]. [9] (figure 87 in appendix) observed these lines in FZ-Si as well as mc-Si, and suggest that they are most probably phonon replicas of the band edge emission with 1, and 2 phonons respectively.

The two peaks observed above 1.16 eV are of unknown origin. The background noise, and dark current has been subtracted, however, the fact that these peaks have the same intensity and shape for different pumping intensities, and have energies above the silicon bandgap, suggest that these are in fact not photoluminescence signal, but noise added by the system.

#### 4.3.2 Comparing different locations on sample ES1-Q3-201

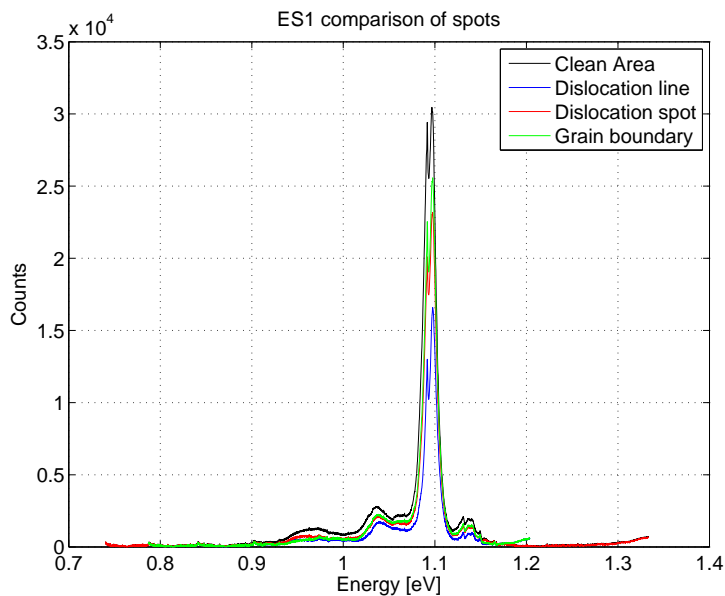


Figure 61: Comparison of different locations on sample ES1-Q3-201 C from results in figure 28, 32, 29, and 30.

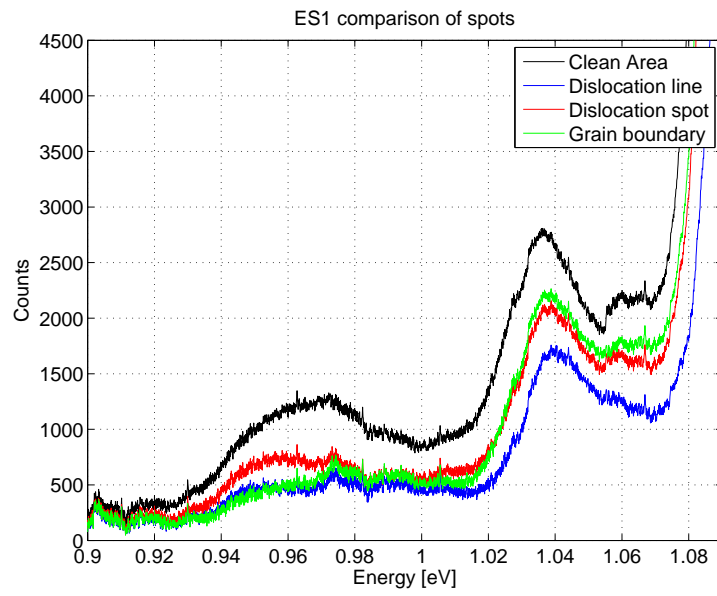


Figure 62: A closer look on differences in ES1-Q3-201 C from graph in figure 61

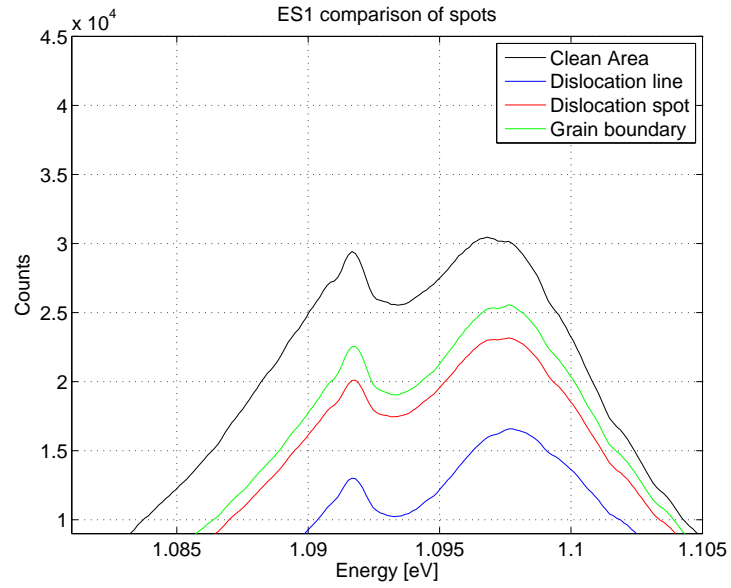


Figure 63: A closer look on differences in ES1-Q3-201 C from graph in figure 61

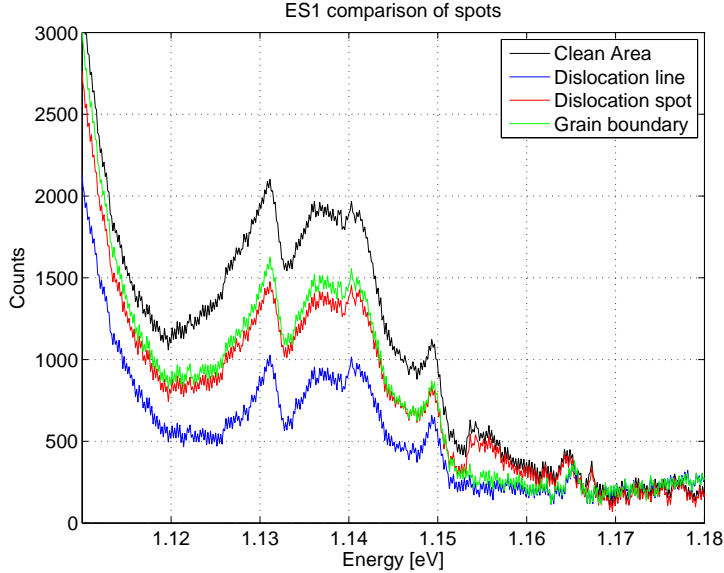


Figure 64: A closer look on differences in ES1-Q3-201 C from graph in figure 61

Intrinsic values are present, and recognized as  $I^{TO+20\Gamma}$ [0.968 eV],  $I^{TO+0\Gamma}$ [1.0315 eV],  $I^{TO}$ [1.097 eV], and  $I^{TA}$ [1.1365 eV]. In addition there are some expected, less defined luminescence at the TO intervalley phonon replica energies of 1.151 eV and 1.074 eV, and intervalley  $I^{TO+0\Gamma}$  replica energy at 1.013 eV. No phonon luminescence at 1.1545 eV seems to disappear in the area of grain boundary and dislocation line. A possible explanation for this, is that the emitted photons carry enough energy to excite a new electron-hole pair. Due to the geometrical properties of dislocation etched line and grain boundary, there is an etch pit with less atoms blocking the excitation laser, compared to the case of a perfect crystal structure. This would result in the laser penetrating deeper into the sample, and the photons are emitted from a deeper region of the sample and are less likely to be emitted with a direct path out of the sample.

Phosphorus no phonon line is observed at 1.1496 eV in [3]. This line should be accompanied by a TO phonon assisted line at 1.0916 eV with three times the intensity. These are not resolved in the ES1 results, but given the strong bound exciton peak, it's likely that it is present. Boron has a similar characteristic, with the no phonon line at 1.1503 eV, and TO phonon assisted line at 1.0924 eV. The no phonon line should have around 0.5% of the  $B^{TO}$  line, which is a considerably larger ratio than that of the  $P^{TO}$  line [3]. Boron and phosphorus lines are indistinguishable from each other, but both are likely to influence the luminescence.

As expected, there are no C-O line present. As for Fe bound with B, a sharp line at 1.068 eV should be present [5]. Even though it could appear like this line is present, it is more likely that this is an artifact from noise, as the same sharp peak shape can be observed in different parts of the spectra known to contain nothing but noise. Based on the repeating on this peak, it is possible that the mean dark current noise has shifted, in regards to intensity for some pixels, compared to the measured mean dark current which is subtracted. An example which shows that the mean dark current noise has shifted, is the repeating artifacts from 0.7 eV to 0.9 eV. As the spectra consist of several glued together spectra, the artifact is repeating itself. These spectra has been glued together with some overlap, so that one side of the spectra has been removed. The rising intensities at 1.3 eV for the red line, show the non-overlapping part of the spectra. For lower energies, these pixels have been disregarded, and replaced by overlap except for the last interval.

Pumping at lower intensities, a new band is observed. This band is likely to be present at higher pumping intensities as well, but saturates, and becomes hard to detect. The peak of this band is at 1.04 eV

#### 4.3.3 Comparing different locations on sample MH2-Q3-210

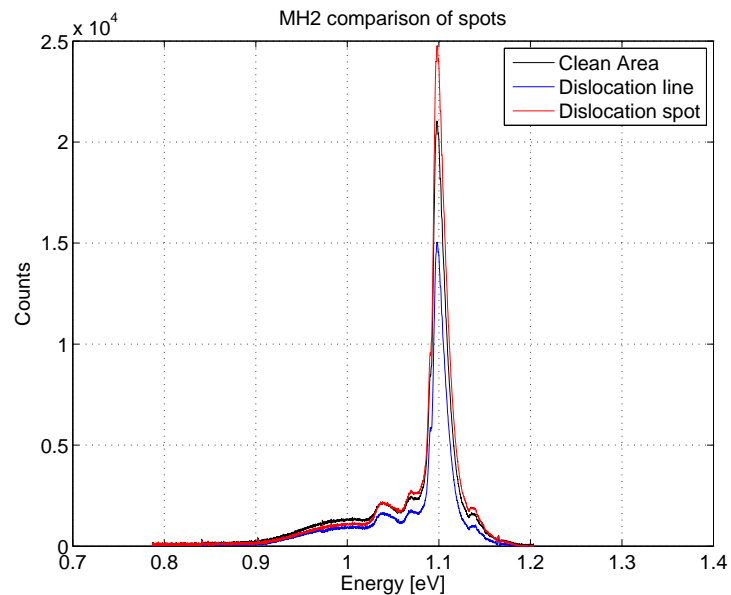


Figure 65: Comparison of different locations on sample MH2-Q3-210 B2 from results in figure 39, 40, and 41

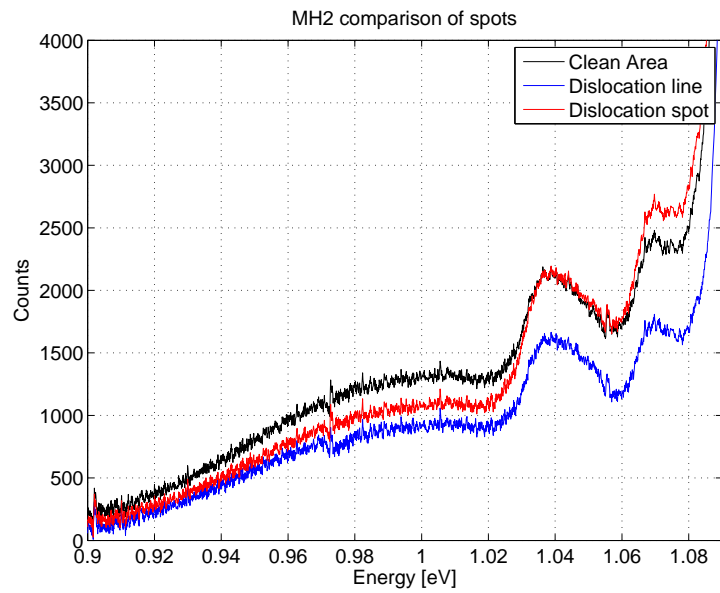


Figure 66: A closer look on differences in MH2-Q3-210 B2 from graph in figure 65

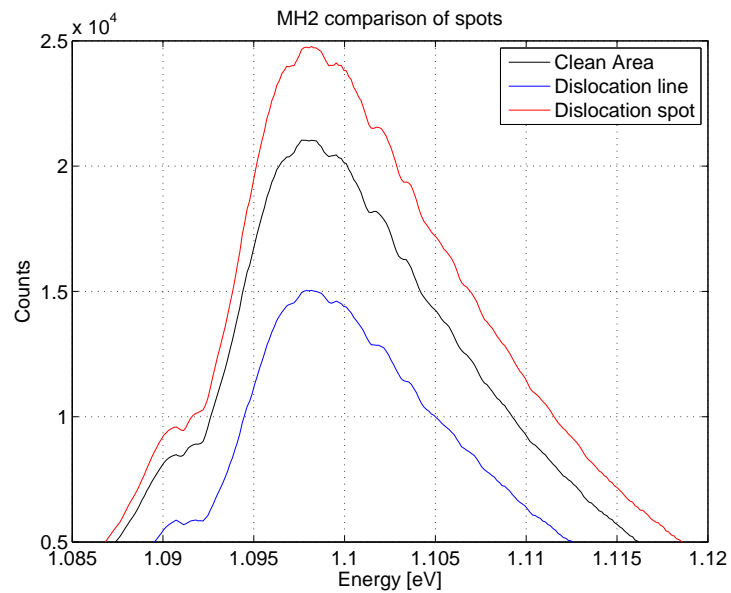


Figure 67: A closer look on differences in MH2-Q3-210 B2 from graph in figure 65

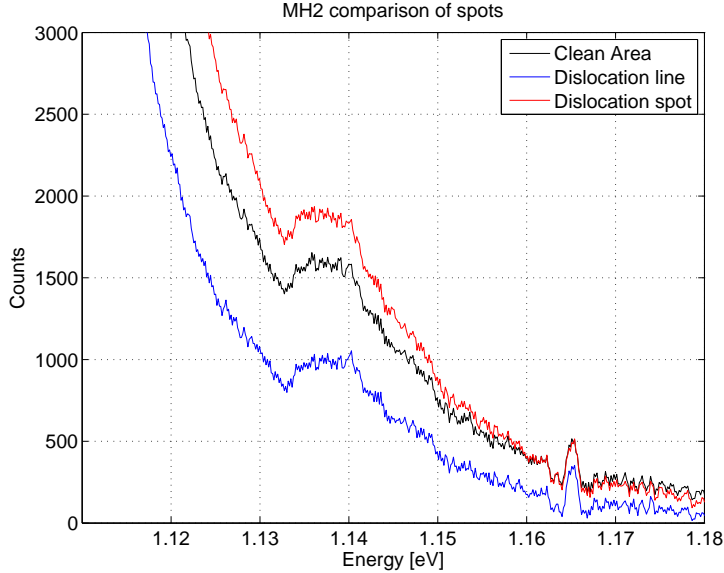


Figure 68: A closer look on differences in MH2-Q3-210 B2 from graph in figure 65

The no phonon line at 1.545 eV is not observed. TA, TO, BE, intervally phonon replica, and zone center phonon TO replica lines are recognized from figure 79. In addition, there are some luminescence around 1 eV and below, which cannot be attributed to 2 zone center phonon TO replica alone. If this is due to D4, which can be observed at 1.0 eV, then D3 should also be observed at 0.934 eV. While it is still possible these lines contribute to the intensity, the luminescence cannot be explained by these alone, due to the asymmetrical shape. [35] observe a similar behavior around D4 at 80K, and argue that it indicates residual stress leading to strong multi-phonon (two and three) mediated band-to-band luminescence rather than radiation from defects.

$\text{CrB}^0$  from [23] where expected at 0.8432 eV. This is not the case for MH2. Chromium not bound with boron, does not give rise to any luminescence, and [23] did not find any chromium related signal in phosphorous doped samples. [23] state that the intensity of this line is proportional with the chromium boron pairs. This would mean that the formation of these pairs haven't taken place in MH2. [23] used chromium doped (by diffusion) Si:B FZ and CZ samples stored at room temperature, to give CrB pairs time to bond. MH2 is mc-Si, and CrB pairs in MH2 have been investigated in [50] by measuring lifetime. No change in lifetime occurred by regards to time, which also suggest that the forming of these pairs have not taken place in MH2 to the extent that it is detectable. This implies that chromium is mostly

dissolved in the silicon lattice as an interstitial specie.

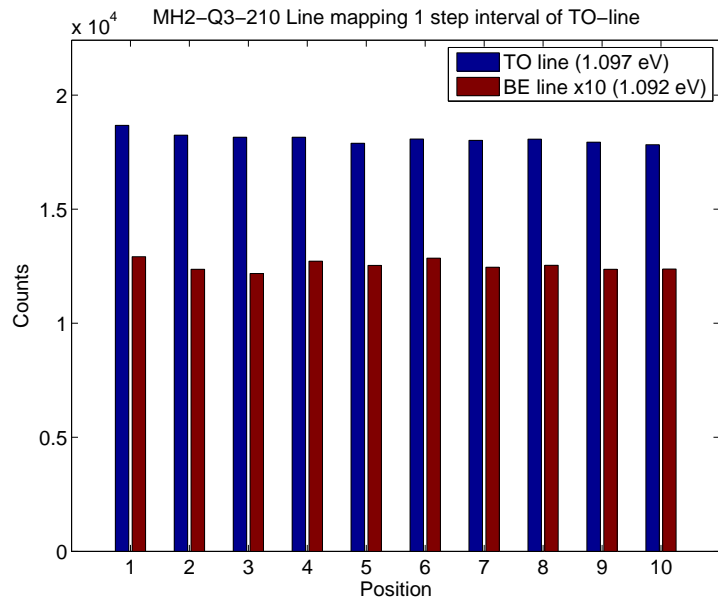


Figure 69: Sample MH2-Q3-210 B2 pumped with 170mW at 14K line map using 10 small steps, looking at TO and BE line only from results in figure 48.

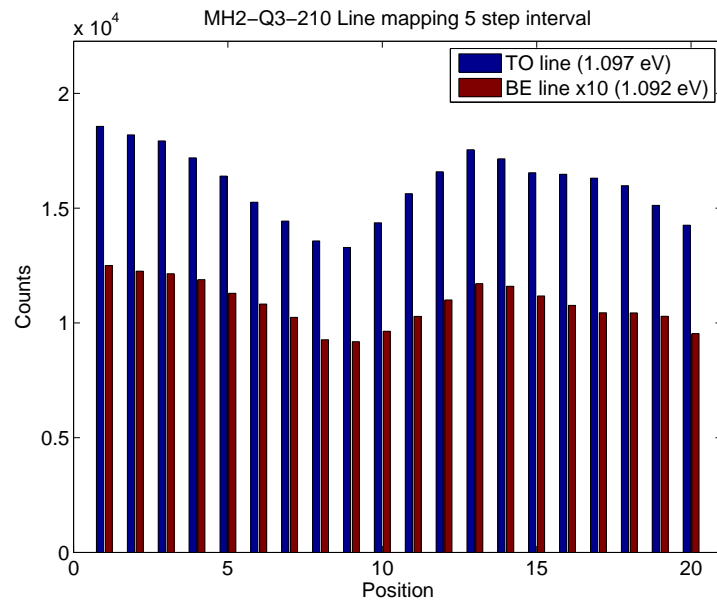


Figure 70: Sample MH2-Q3-210 B2 pumped with 170mW at 14K line map using 20 small steps exactly 5 times larger than in figure 48, looking at TO and BE line only from results in figure 51.

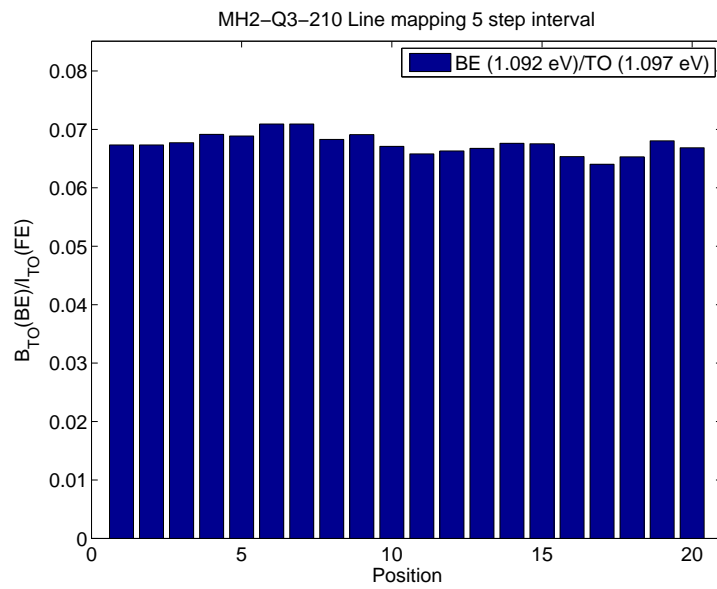


Figure 71: Sample MH2-Q3-210 B2 comparing relative intensity between TO and BE line from results in 70.

#### 4.3.4 Comparing similar areas on different samples

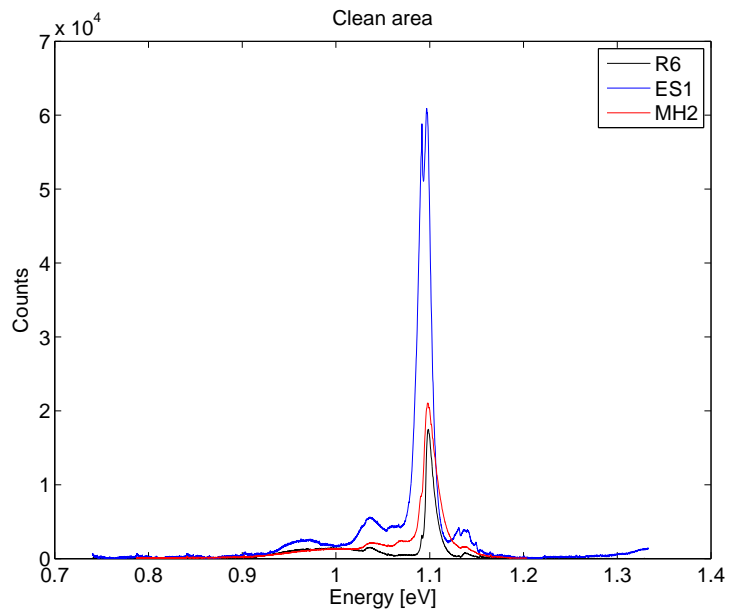


Figure 72: Results from figure ( 23,28,39) where results in figure 28 are multiplied by 2, to account for 10s integration time compared to 20.

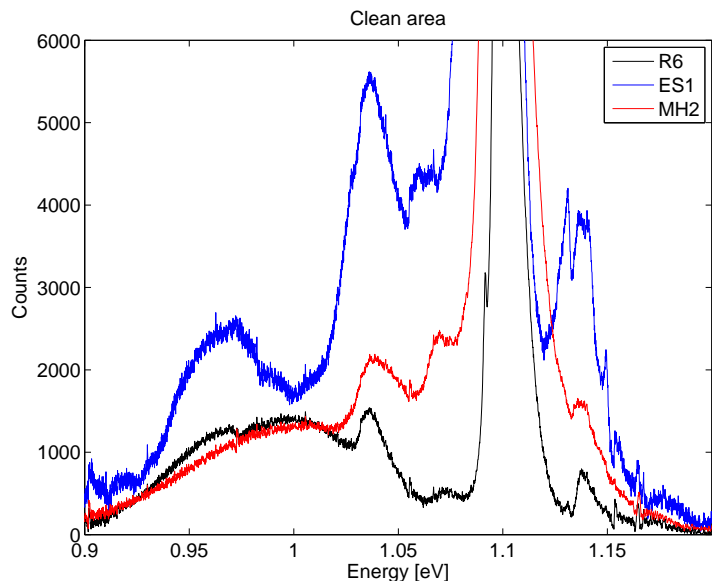


Figure 73: Plot from figure 72 in greater detail

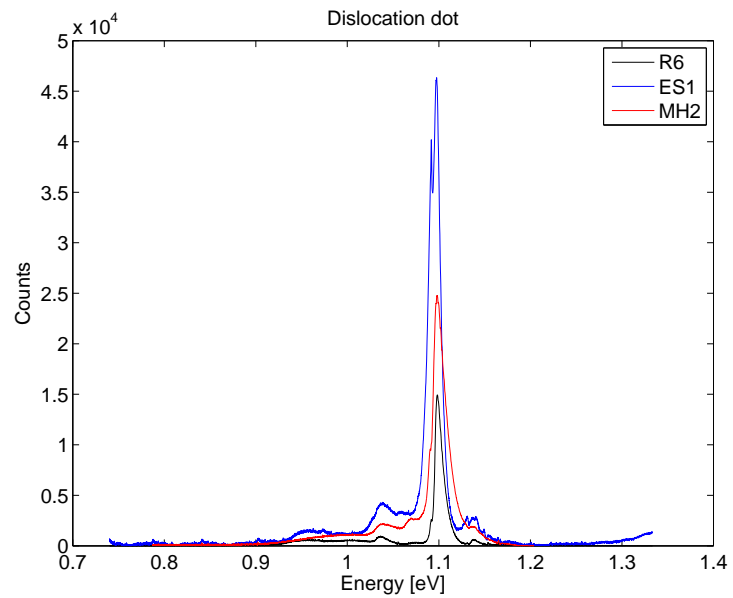


Figure 74: Results from figure ( 22,29,41) where results in figure 29 are multiplied by 2, to account for 10s integration time compared to 20.

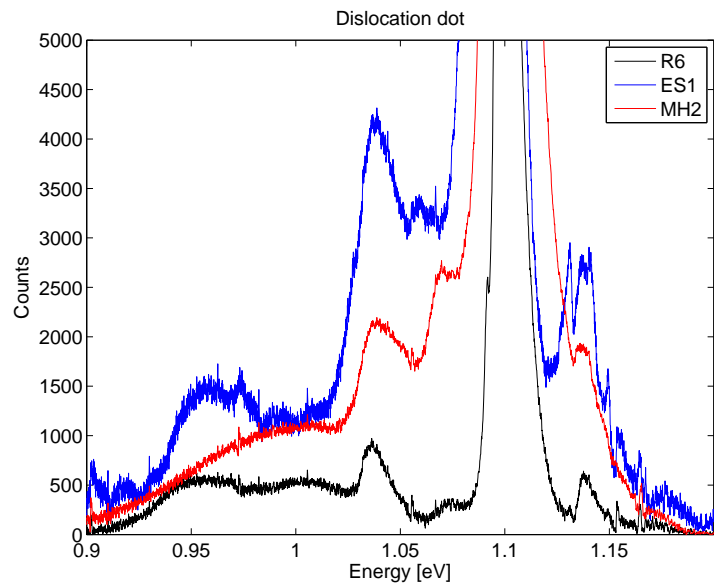


Figure 75: Plot from figure 74 in greater detail

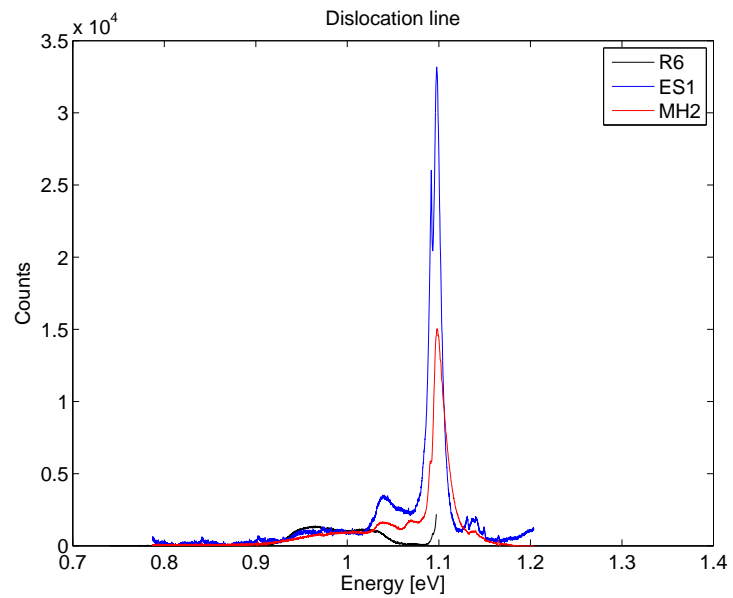


Figure 76: Results from figure ( 21,32,40 ) where results in figure 32 are multiplied by 2, to account for 10s integration time compared to 20.

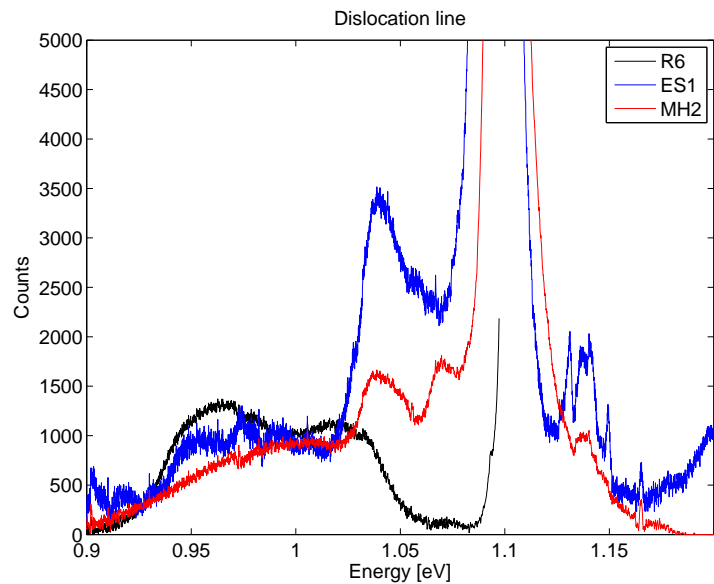


Figure 77: Plot from figure 76 in greater detail

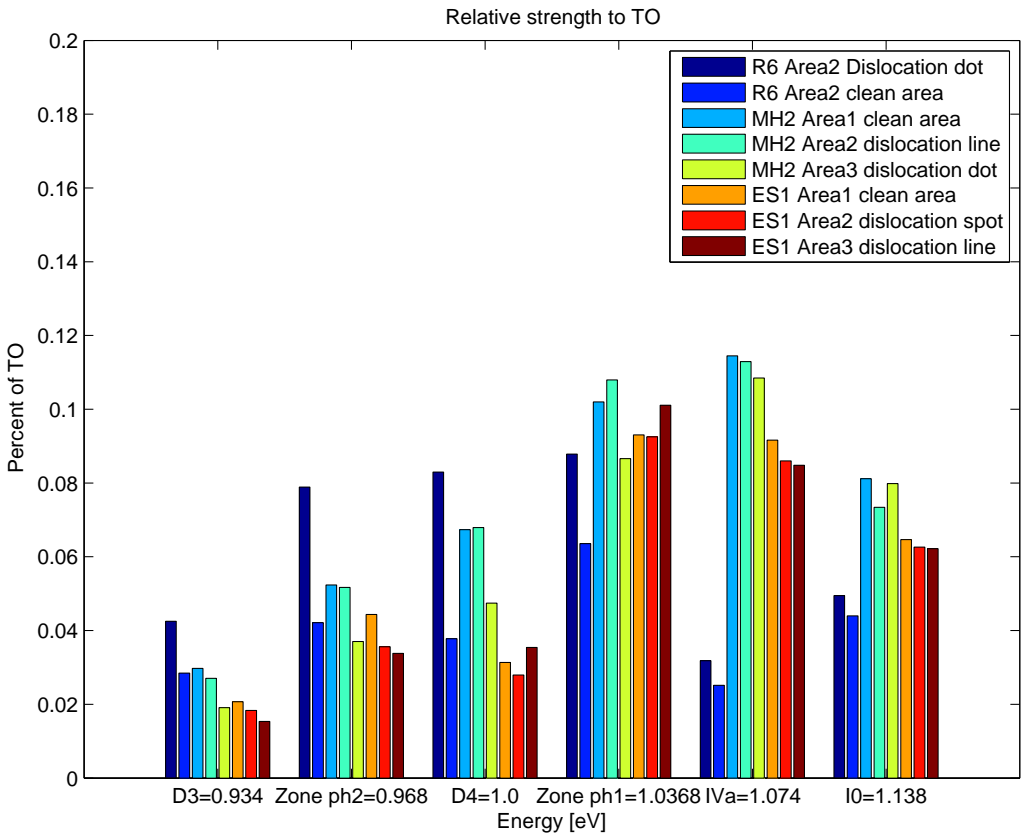


Figure 78: Comparison of relative strength of known characteristics to TO line

Compared to R6, ES1 have a fairly intense bound exciton line at 1.092 eV. This corresponds to a higher concentration of boron and phosphorus atoms according to [56]. The ratio is different on different parts of the sample, which could mean that the doping atoms are unevenly distributed. It could also mean that the excitons at defect locations are more subject to interaction with defect characteristics, than the TO line. This behavior was reported in [24], which state that the series of bound exciton lines decrease sharply in intensity in areas of dislocations.

## References

- [1] B. Jalali, "Physics and technology forefronts - silicon lasers," *American Physical Society*, 2006.
- [2] B. G. Streetman and S. K. Banerjee, *Solid state electronic devices*. Prentice Hall, 2006.
- [3] P. J. Dean, J. Haynes, and W. Flood, "New radiative recombination processes involving neutral donors and acceptors in silicon and germanium," *Physical Review Volume 161 Number 3*, 1967.
- [4] M. Càlao and M. do Carmo, "Luminescence from an iron related deep center in silicon," *Physica Scripta*, 1988.
- [5] H. Mohring, J. Weber, and R. Sauer, "Photoluminescence of excitons bound to an isoelectronic trap in silicon associated with boron and iron," *Physical Review B*, 1983.
- [6] H. Conzelmann and J. Weber, "Photoluminescence from chromium-boron pairs in silicon," *Physica*, 1983.
- [7] L. Patrick and W. Choyke, "Photoluminescence of ti in four sic polytypes," *Physical Review B*, 1974.
- [8] I. Tarasov, S. Ostapenko, W. Seifert, M. Kittler, and J. Kaleis, "Defect diagnostics in multicrystalline silicon using scanning techniques," *Elsevier Science B.V.*, 2001.
- [9] T. Arguirov, W. Seifert, M. Kittler, and J. Reif, "Temperature behaviour of extended defects in solar grade silicon investigated by photoluminescence and ebic," *Elsevier B.V.*, 2003.
- [10] B. Sopori, P. Rupnowski, V. Mehta, V. Budhraja, S. Johnston, N. Call, H. Moutinho, M. Al-Jassim, A. Shaikh, M. Seacrist, and D. Carlson, "Performance limitations of mc-si solar cells caused by defect clusters," *Conference Paper NREL/CP-520-45012*, 2009.
- [11] T. Markvart, *Solar Electricity*. John Wiley & Sons ltd., 2000.
- [12] A. Luque and S. Hegedus, *Handbook of photovoltaic science and engineering*. John Wiley & Sons ltd., 2003.
- [13] [www.siliconfareast.com<sup>TM</sup>](http://www.siliconfareast.com), "Crystalline defects in silicon." <http://www.siliconfareast.com/crystaldefects.htm>.

- [14] G. Davies, “The optical properties of luminescence centres in silicon,” *Physics Report*, 1988.
- [15] I. Tarasov, S. Ostapenko, C. Haessler, and E.-U. Reisner, “Spatially resolved defect diagnostics in multicrystalline silicon for solar cells,” *Elsevier Science S.A.*, 2000.
- [16] J. A. Gavira-Gallardo, J. D. Ng, and M. George, “Stacking faults.” <http://lmass.uah.edu>.
- [17] Z. Aksamija, H.-S. Hahm, and U. Ravaioli, “Emission and absorption of phonons in silicon,” *phys. stat. sol. (c)*, 2007.
- [18] C. Kittel, *Introduction to Solid State Physics*. John Wiley & Sons, 2005.
- [19] P. Gundel, M. C. Schubert, W. Kwapił, J. Schön, M. Reiche, H. Savin, M. Yli-Koski, J. A. S. and Gema Martinez-Criado, W. Seifert, W. Warta, and E. R. Weber, “Micro-photoluminescence spectroscopy on metal precipitates in silicon,” *Phys. Status Solidi RRL*, 2009.
- [20] E. Palik., *Handbook of optical constants of solids*. 2001.
- [21] S. Nihonyanagi and Y. Kanemitsu, “Enhanced luminescence from electron-hole droplets in silicon nanolayers,” *Applied physics letters*, 2004.
- [22] R. Hammond, T. McGill, and J. Mayer, “Temperature dependence of the electron-hole-liquid luminescence in si,” *Physical Review B*, 1975.
- [23] H. Conzelmann, K. Graff, and E. Weber, “Chromium and chromium-boron pairs in silicon,” *Appl. Phys. A*, 1982.
- [24] N. A. Drozdov, A. Patrin, and V. Tkachev, “Recombination radiation on dislocations in silicon,” *Pis'ma Xh. Eksp. Teor. Fiz.*, 1976.
- [25] W. Lee, J. Chen, B. Chen, J. Chang, and T. Sekiguchi, “Cathodoluminescence study of dislocation-related luminescence from small-angle grain boundaries in multicrystalline silicon,” *Applied Physics Letters*, 2009.
- [26] R. Sauer, J. Weber, and J. Stolz, “Dislocation-related photoluminescence in silicon,” *Appl. Phys.*, 1985.

- [27] H. Sugimoto, M. Inoue, M. Tajima, A. Ogura, and Y. Ohsita, “Analysis of intra-grain defects in multicrystalline silicon wafers by photoluminescence mapping and spectroscopy,” *Japanese Journal of Applied Physics*, 2006.
- [28] M. Suezawa, Y. Sasaki, and K. Sumino, “Dependence of photoluminescence on temperature in dislocated silicon crystals,” *Physica Status Solidi*, 1983.
- [29] V. Higgs, P. Kightley, P. Goodhew, and P. Augustus, “Metal-induced dislocation nucleation for metastable sige/si,” *Appl. Phys. Lett.*, 1991.
- [30] T. Sekiguchi and K. Sumino, “Cathodoluminescence study on dislocations in silicon,” *J. Appl. Phys.*, 1995.
- [31] V. Kveder, E. Steinman, S. Shevchenko, and H. Grimmeiss, “Dislocation-related electroluminescence at room temperature in plastically deformed silicon,” *Phys. Rev. B*, 1995.
- [32] K. Weronek, J. Weber, and R. Buchner, “Origin of d-band photoluminescence in silicon,” *Springer Proceedings in Physics*, 1991.
- [33] W. Staiger, G. Pfeiffer, K. Weronek, A. Höpner, and J. Weber, “Dislocation-induced defect levels in silicon,” *Materials Science Forum*, 1994.
- [34] M. Kittler, W. Seifert, T. Arguirov, I. Tarasov, and S. Ostapenko, “Room-temperature luminescence and electronbeam-induced current (ebic) recombination behaviour of crystal defects in multicrystalline silicon,” *Solar Energy Materials and Solar Cells*, 2002.
- [35] T. V. Arguirov, *Electro-optical properties of dislocations in silicon and their possible application for light emitters*. PhD thesis, Naturwissenschaften und Informatik der Brandenburgischen Technischen Universität Cottbus, 2007.
- [36] H. Sugimoto, K. Araki, M. Tajima, T. Eguchi, I. Yamaga, M. Dhamrin, K. Kamisako, and T. Saitoh, “Photoluminescence analysis of intragrain defects in multicrystalline silicon wafers for solar cells,” *Journal of Applied Physics*, 2007.
- [37] A. van Kemenade and S. Hagen, “Proof of the involvement of ti in the low-temperature abc luminescence spectrum of 6h sic,” *Solid State Communications*, 1974.

- [38] J. Weber, H. Bauch, and R. Sauer, “Optical properties of copper in silicon: Excitons bound to isoelectronic copper pairs,” *Physical Review B*, 1982.
- [39] G. Zoth and W. Bergholz, “A fast preparation-free method to detect iron in silicon,” *J. Appl. Phys.*, 1990.
- [40] D. Macdonald, J. Tan, and T. Trupke, “Imaging interstitial iron concentrations in boron-doped crystalline silicon,” *Journal of applied physics*, 2008.
- [41] V. Higgs, M. Goulding, and P. Kightley, “Characterization of epitaxial and oxidation-induced stacking faults in silicon: The influence of transition-metal contamination,” *Appl. Phys. Lett.*, 1992.
- [42] J. Bailey and E. R. Weber, “Precipitation of iron in polycrystalline silicon,” *Physica Status Solidi (a)*, 1993.
- [43] E. C. Lightowlers and V. Higgs, “Luminescence associated with the presence of dislocations in silicon,” *Physica Status Solidi (a)*, 1993.
- [44] N. Drozdov and A. Fedotov, “Electron-hole drops in dislocational silicon,” *Microelectronic Engineering* 66, 2002.
- [45] N. A. Drozdov, A. A. Patrin, and V. T. Tkachev, “Modification of the dislocation luminescence spectrum by oxygen atmospheres in silicon,” *physica status solidi (a)*, 1981.
- [46] M. Tajima, M. Tokita, and M. Warashina, “Photoluminescence due to oxygen precipitates distinguished from the d-lines in annealed si,” *Materials Science Forum*, 1995.
- [47] M. Inoue, H. Sugimoto, M. Tajima, Y. Ohshita, and A. Ogura, “Microscopic and spectroscopic mapping of dislocation-related photoluminescence in multicrystalline silicon wafers,” *J. Mater Sci*, 2007.
- [48] P. Gundel, M. C. Shubert, and W. Warta, “Origin of trapping in multicrystalline silicon,” *Journal of applied physics*, 2008.
- [49] B. Sopori, “A new defect etch for polycrystalline silicon,” *J. Electrochem. Soc.*, 1984.
- [50] M. Hystad, “The distribution and impact of chromium impurities in compensated sog-silicon,” Master’s thesis, The Norwegian University of Science and Technology, 2009.

- [51] C. Modanese, “Electronic grade sample impurity levels.” private communication, 2010.
- [52] S. Orfanidis, *Introduction to Signal Processing*. Prentice-Hall, 1996.
- [53] A. Hare, G.Davies, and A.T.Collins, “The temperature dependence of vibronic spectra in irradiated silicon,” *J. Phys. C: Solid State Phys.*, 1972.
- [54] H. Lemke, “Dotierungseigenschaften von eisen in silizium,” *physica status solidi (a)*, 1981.
- [55] R. Sauer, “Evidence for bound multiple-exciton complexes in silicon,” *Phys. Rev. Let.*, 1973.
- [56] M. Tajima, “Determination of boron and phosphorus concentration in silicon by photoluminescence analysis,” *Electrotechnical Laboratory*, 1978.
- [57] T. Arguirov, W. Seifert, M. Kittler, and J. Reif, “Temperature behaviour of photoluminescence and electron-beam-induced current recombination behaviour of extended defects in solar grade silicon,” *J. Phys.: Condens. Matter*, 2002.
- [58] T. Arguirov, W. Seifert, and M. K. J. Reif, “Temperature behaviour of photoluminescence and electron-beam-induced current recombination behaviour of extended defects in solar grade silicon,” *J. Phys: Condens, 2002.*
- [59] R. Sauer, J. Weber, , and J. Stolz, “Dislocation-related photoluminescence in silicon,” *Applied Physics*, 1985.
- [60] V. V. Kveder, E. A. Steinman, S. A. Shevchenko, and H. G. Grimmeiss, “Dislocation-related electroluminescence at room temperature in plastically deformed silicon,” *Phys. Rev. B*, 1995.
- [61] K. Leosson, J. Jensen, J. Hvam, and W. Langbein, “Linewidth statistics of single ingaas quantum dot photoluminescence lines,” 2000.
- [62] T. Arguirov, W.Seifer, G. Jia, and M. Kittler, “Photoluminiscence study on defects multicrystalline silicon,” *Semiconductors*, 2006.
- [63] A. J. Kenyon, C. E. Chryssoua, C. W. Pitta, T. Shimizu-Iwayamab, D. E. Holec, N. Sharmad, and C. J. Humphreysd, “Broad-band and flash-lamp pumping of 1.53  $\mu\text{m}$  emission from erbium-doped silicon nanocrystals,” 2001.

- [64] M. Inoue, H. Sugimoto, M. Tajima, Y. Ohshita, and A. Ogura, “Microscopic and spectroscopic mapping of dislocation-related photoluminescence in multicrystalline silicon wafers,” *Mater Electron*, 2008.
- [65] E. Katz, M. Koltun, and L. Polyak, “Polycrystalline silicon solar cells: Improvements in efficiency through hydrogen passivation,” *Diffusion and Defect Data Pt.B: Solid State Phenomena*, 1996.
- [66] S. Binetti, J. Libal, M. Acciarri, M. D. Sabatino, H. Nordmark, E. Øverlid, J. Walmsley, and R. Holmestad, “Study of defects and impurities in multicrystalline silicon grown from metallurgical silicon feedstock,” *Materials Science and Engineering B*, 2008.
- [67] L. Patrick and W. Choyke, “Photoluminescence of ti in four sic polytypes,” *Physical Review B*, 1974.
- [68] M. Wagner, I. Ivanov, L. Storasta, J. Bergman, B. Magnusson, W. Chen, and E. Janzén, “Photoluminescence upconversion in 4h-sic,” *Applied Physics Letters*, 2002.
- [69] J. Dean, “Photoluminescence as a diagnostic of semiconductors,” *Prog. Crystal growth charact.*, 1982.
- [70] H. Conzelmann, “Photoluminescence of transition metal complexes in silicon,” *Appl. Phys. A*, 1987.
- [71] S. A. Shevchenko and A. N. Izotov, “Dislocation-induced photoluminescence in silicon crystals of various impurity composition,” *Physics of the Solid State*, 2003.
- [72] T. Trupke, R. A. Bardos, M. C. Schubert, and W. Warta, “Photoluminescence imaging of silicon wafers,” *Applied Physics Letters*, 2006.
- [73] J. Bauer, O. Breitenstein, and J.-P. Rakotonaina, “Electronic activity of sic precipitates in multicrystalline solar silicon,” *phys. stat. sol. (a)*, 2007.
- [74] V. Karasuyk, A. Steele, A. Mainwood, E. Lightowlers, and G. Davies, “Ultrahigh-resolution photoluminescence studies of excitons bound to boron in silicon under uniaxial stress,” *Physical Review B*, 1992.
- [75] M. Kasemann, D. Grote, B. Walter, W. Kwapił, T. Trupke, Y. Augarten, R. Bardos, E. Pink, M. Abbott, and W. Warta, “Luminescence imaging for the detection of shunts on silicon solar cells,” *Prog. Photovolt: Res. Appl.*, 2008.

- [76] M. Kasemann, W. Kwapis, B. Walter, J. Giesecke, B. Michl, M. The, J. Wagner, J. Bauer, A. Schütt, J. Carstensen, S. Kluska, F. Granek, H. Kampwerth, P. Gundel, M. Schubert, R. Bardos, H. Föll, H. Nagel, P. Würfel, T. Trupke, O. Breitenstein, M. Hermle, W. Warta, and S. Glunz, “Progress in silicon solar cell characterization with infrared imaging methods,” *23rd European Photovoltaic Solar Energy Conference*, 2008.
- [77] S. McHugo, H. Hieslmair, and E. Weber, “Gettering of metallic impurities in photovoltaic silicon,” *Appl. Phys. A*, 1996.
- [78] S. Ostapenko, I. Tarasov, J. Kalejs, C. Haessler, and E. Reisner, “Defect monitoring using scanning photoluminescence spectroscopy in multicrystalline silicon wafers,” *Semicond. Sci. Technol.*, 2000.
- [79] S. Pizzini, M. Acciarri, E. Leoni, and A. L. Donne, “About the d1 and d2 dislocation luminescence and its correlation with oxygen segregation,” *phys. stat. sol. (b)*, 2000.
- [80] E. Steinman, A. Kenyon, and A. Tereshchenko, “Time-resolved measurements of dislocation-related photoluminescence bands in silicon,” *Semicond. Sci. Technol.*, 2008.
- [81] H. Sugimoto, M. Tajima, T. Eguchi, I. Yamaga, and T. Saitoh, “Photoluminescence analysis of intra-grain defects in cast-grown polycrystalline silicon wafers,” *Materials Science in Semiconductor Processing*, 2006.
- [82] M. Tajima, “Characterization of semiconductors by photoluminescence mapping at room temperature,” *Journal of Crystal Growth*, 1990.
- [83] B. H. Liesert, T. Gregorkiewicz, and C. Ammerlaan, “Photoluminescence studies on therma donors in boron- and aluminum-doped silicon,” *Physical Review B*, 1991.
- [84] E. Irion, N. Biirger, W. Kiirner, K. Thonke, R. Sauer, W. Zulehner, and G. Pensl, “Photoluminescence study of acceptor-carbon complexes in irradiated silicon - aluminum-related defects,” *Appl. Phys. A*, 1988.
- [85] I. G. G. N. Mishinova and Y. M. Suleimanov, “Low-temperature luminescence of silicon carbide crystals,” *Zhurnal Prikladnoi Spektroskopii*, 1966.
- [86] R. Sauer, “1974,” *Solid State Communications*, Bound Multiple-Excition Complexes in Silicon at High Doping Levels.

## A Silicon energy bands

Energy	Name	Temp.	Impurity / Defect	Observed in
0.735eV	ZPL	22K	Fe contamination	[4]
0.745eV	C-N		Carbon-Nitrogen complex	[14]
0.76-0.8eV	Defect	290K	Dislocation with low contamination	[15, 8, 62]
0.77-0.78eV	$D_b$	4.2-295K	Oxygen impurity band	[46, 47]
0.77eV	P line	12K	C-O complex related	[14, 66]
0.780eV	$\text{CrB}^0\Gamma$	4.2K	$\text{CrB}^0$ phonon replica	[6]
0.79eV	C-O	12K	Carbon-Oxygen complex	[14, 66, 53]
0.80eV	D1'	77K	Dislocations <sup>1</sup>	[15, 8]
0.812eV	D1	4.2K	Dislocation related line <sup>1</sup>	[24, 26, 9]
0.8160	$\text{CrB}^2$	4.2K	Cr-B excitation of local vibrations	[6]
0.8402	$\text{CrB}^1$	4.2K	Cr-B excitation of local vibrations	[6]
0.8432eV	$\text{CrB}^0$	4.2K	Cr-B pair no-phonon	[23, 6]
0.875eV	C-Ga		Carbon-Gallium complex	[14]
0.875eV	D2	4.2K	Dislocation related line <sup>1</sup>	[24, 26, 9]
0.89eV	D2'	77K	Dislocations <sup>1</sup>	[15, 8]
0.8-0.9eV	$D_{a1}$	11K	Broad background emission under D1/D2	[46]
0.91eV	H-line	12K	C-O complex related	[14, 66]
0.93eV	H-line	12K	C-O complex related	[14, 66]
0.934eV	D3	4.2K	Dislocations <sup>2</sup>	[24, 26, 9]
0.95eV	D3'	77K	Dislocations <sup>2</sup>	[15, 8]
0.953eV	D5	4.2K	Straight dislocations	[26, 32]
0.9537eV	Defect	300K	Iron precipitate	[19]
0.968eV	$I^{TO+20^\Gamma}$	26K	TO + 2 Zone center phonon	[3]
0.969eV	C-C		Carbon-Carbon complex	[14]
0.98eV	R2BB	80K	Two phonon replica of band edge emission	[9]
0.9-1.0eV	$D_{a2}$	11K	Broad background emission under D3/D4	[46]
1.000eV	D4	4.2K	Dislocations <sup>2</sup>	[24, 26, 9]
1.00eV	D4'	77K	Dislocations <sup>2</sup>	[15, 8]
1.0089eV	$\text{FeB}^0(\text{TO})$	6K	Fe-B pair phonon replica	[5]
1.0126eV	D6	4.2K	Stacking faults	[26, 32]
1.013eV	$I^{TO+0^\Gamma+IV^a}$	26K	$TO + 0^\Gamma + IV^a$ phonon	[3]
1.014eV	$Cu_0$	4.2K	Copper doping	[38, 32]
1.018eV	W/I1		Radiation damage	[14]
1.0315eV	$I^{TO+0^\Gamma}$	26K	TO + Zone center phonon	[3]
1.04eV	R1BB	80K	One phonon replica of band edge emission	[9]
1.045eV	Q		4-Li atom complex	[14]
1.0504eV	$\text{FeB}^2$	6K	Fe-B pair contamination	[5]

Continued on next page

**Table 7 – continued from previous page**

Energy	Name	Temp.	Impurity / Defect	Observed in
1.051eV	I <sup>TO+IV<sup>b</sup></sup>	26K	Inter valley phonon replica	[3]
1.0595eV	FeB <sup>1</sup>	6K	Fe-B pair contamination	[5]
1.0692eV	FeB <sup>0</sup>	6K	Fe-B pair no phonon	[5]
1.074eV	I <sup>TO+IV<sup>a</sup></sup>	26K	Inter valley phonon replica	[3]
1.078	EHD	4.2K	Electron Hole Droplet dislocation-area	[44]
1.082eV	EHD <sub>TO</sub>	4.2K	Electron Hole Droplet dislocation-free	[22, 44, 21]
1.0835eV	In <sup>TO</sup>	30K	Indium doping TO	[3]
1.0888eV	Bi <sup>TO</sup>	15K	Bismuth doping TO	[3]
1.0902eV	Al <sup>TO</sup>	30K	Aluminum doping TO	[3]
1.0907eV	As <sup>TO</sup>	15K	Arsenic doping TO	[3]
1.0907eV	Ga <sup>TO</sup>	15K	Gallium doping TO	[3]
1.0916eV	P <sup>TO</sup>	15K	Phosphorus doping TO	[3]
1.0921eV	Sb <sup>TO</sup>	15K	Antimony doping TO	[3]
1.0924eV	Si:B(BE) <sup>TO</sup>	4.2K	Si:B bound exciton TO line	[24, 55, 86, 36, 47]
1.097eV	I <sup>TO</sup> (FE)	26K	Transversal Optical/Free exciton	[3, 55, 22, 44]
1.1319eV	Si:B(BE) <sub>2</sub> <sup>0</sup>	26K	Transversal Acoustical phonon mode	[3]
1.1365eV	I <sup>TA</sup> (FE)	26K	Transversal Acoustic	[22, 3]
1.147eV	Si:P <sup>TO</sup> (BE)	2K	Si:P bound exciton replica	[55, 86]
1.1496eV	Si:P(BE)	2K	Si:P bound exciton no phonon	[55, 3]
1.1503eV	Si:B(BE)	26K	Si:B bound exciton no phonon	[3]
1.1545eV	I <sup>0</sup> (FE)	26K	No phonon	[3]
2.786eV	<sup>48</sup> C Ti	4.2K	C line Ti isotope 48 impurity in 6H SiC	[37]
2.820eV	<sup>48</sup> B Ti	4.2K	B <sup>0</sup> line Ti isotope 48 impurity in 6H SiC	[37, 68]
2.85eV	<sup>48</sup> Ti	4.2K	Ti isotope 48 impurity in 4H SiC	[7]
2.861eV	<sup>48</sup> A Ti	4.2K	A <sup>0</sup> line Ti isotope 48 impurity in 6H SiC	[37, 68]

Table 7: Silicon energy bands

<sup>1</sup>D1 and D2: It has been argued that they originate in electronic transition at the geometrical kinks on dislocations [28], point defects [26] and impurities [29] and/or from the reaction products of dislocations [30].

<sup>2</sup>D3 and D4 lines is generally thought to be related to electronic transition within dislocation cores [31]. In addition, it has been suggested that the D3 line most likely is a phonon-assisted replica of D4 [31].

## B Sample types and procedures

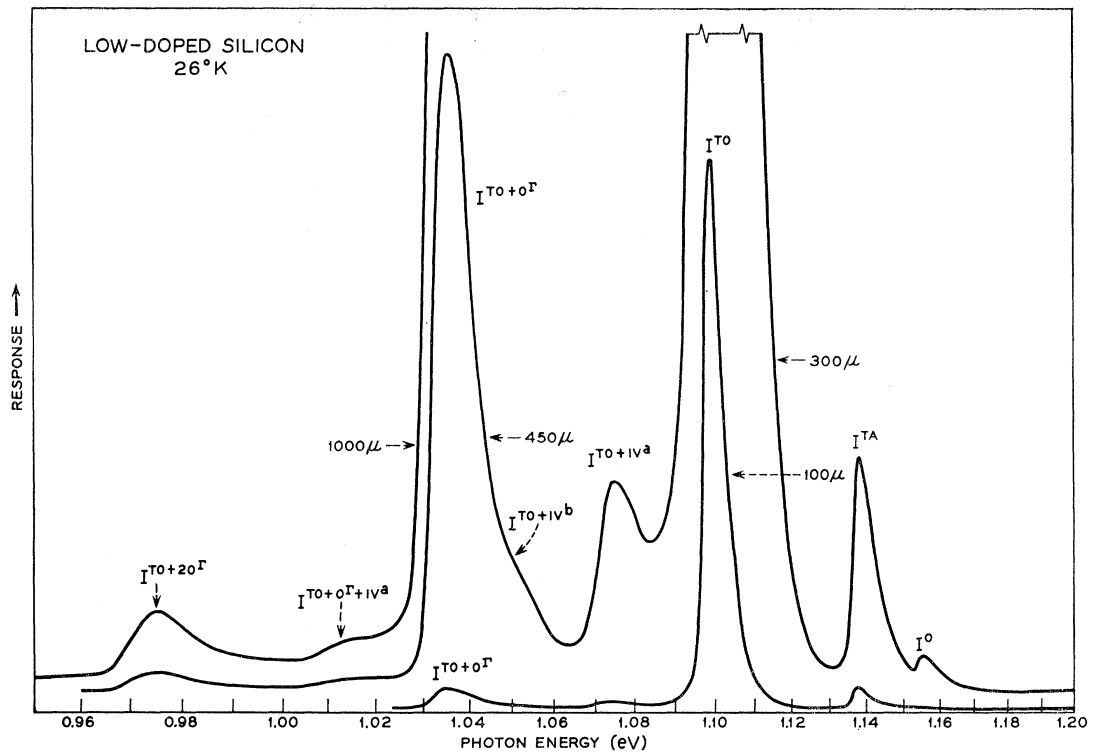


Figure 79: Intrinsic/low doped ( $2 \cdot 10^{14} cm^{-3}$  P atoms) Si PL from [3]

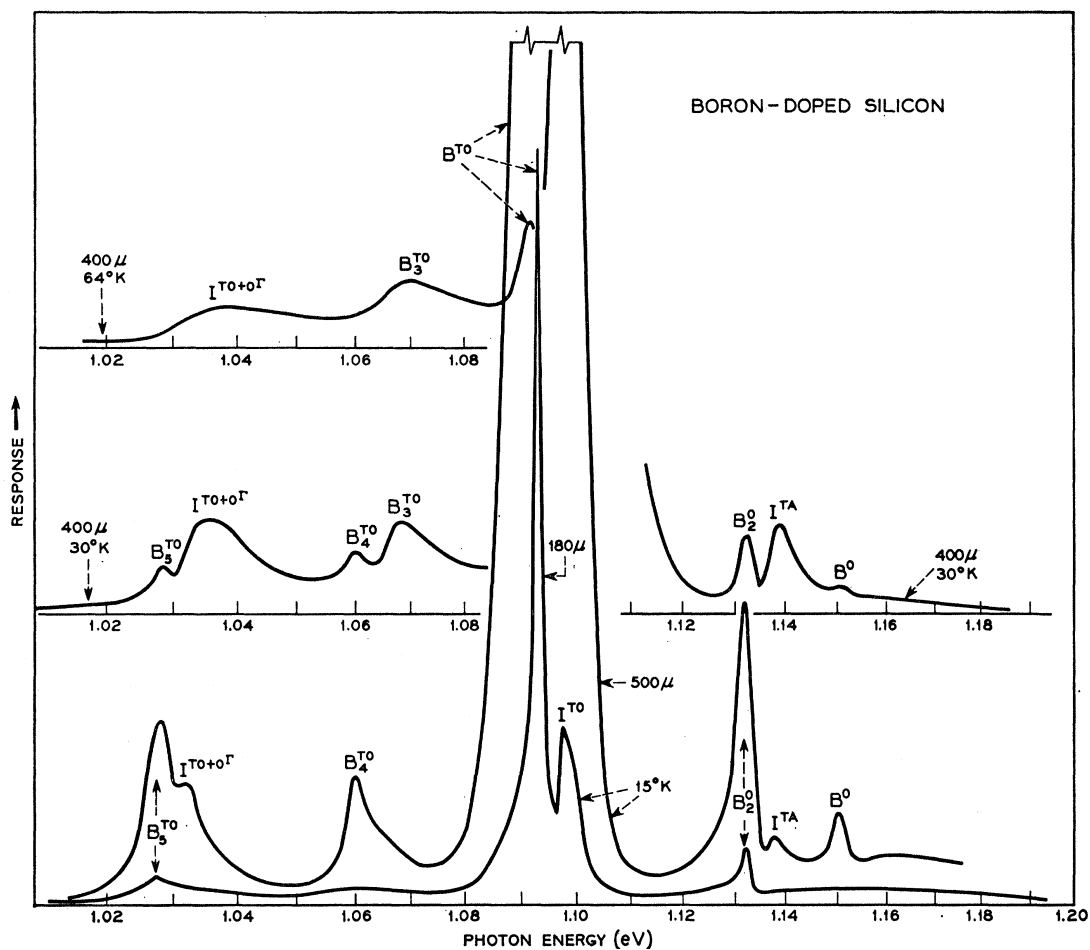


Figure 80: Boron doped ( $6 \cdot 10^{16} cm^{-3}$ ) Si PL specter from [3]

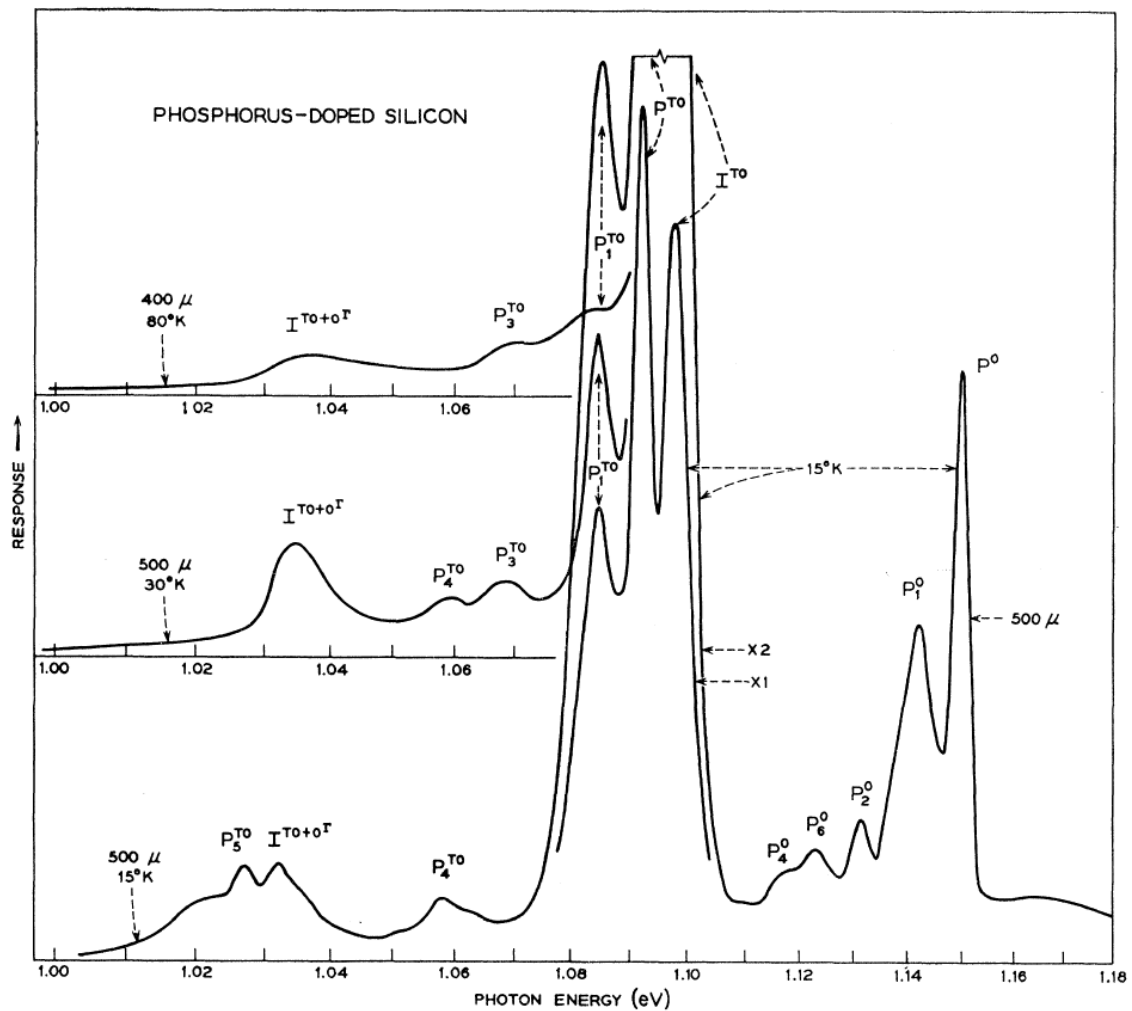


Figure 81: Phosphorus doped ( $8 \cdot 10^{16} cm^{-3}$ ) Si PL specter from [3]

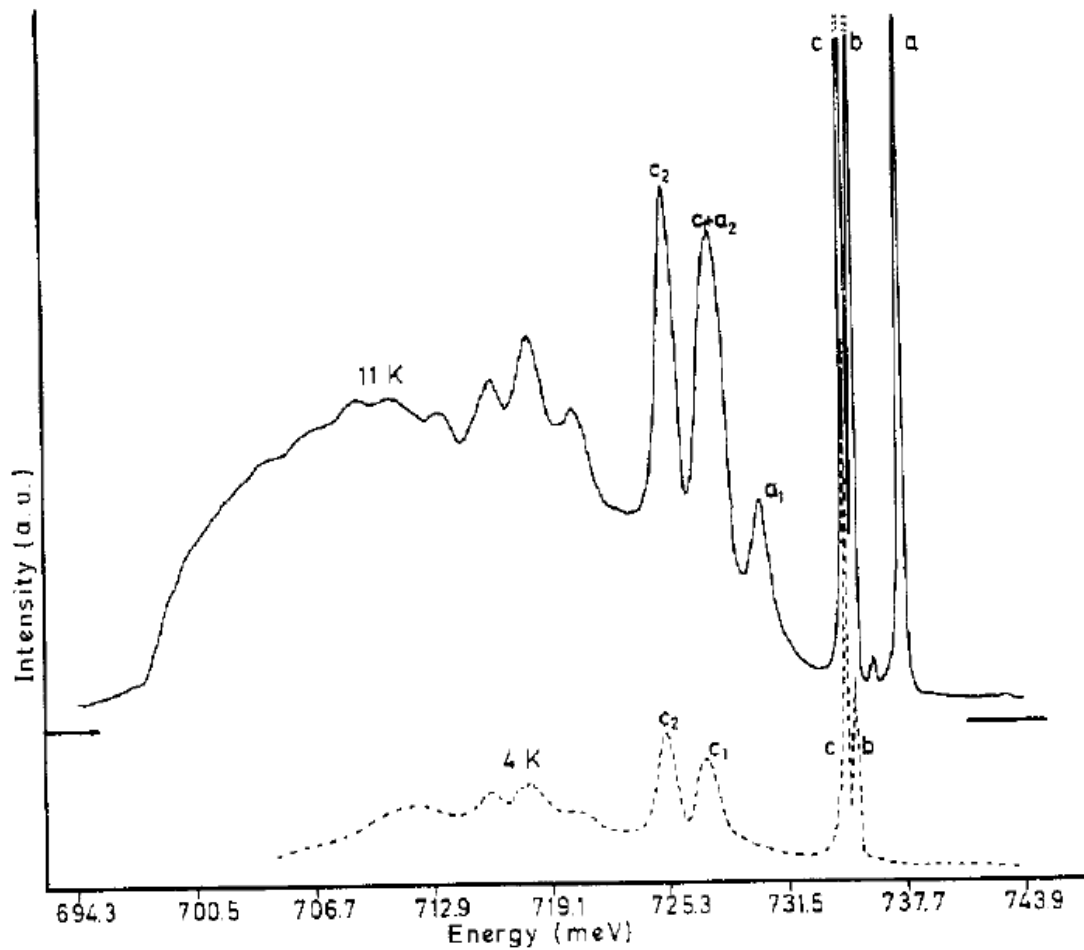


Figure 82: Iron diffused Si sample at two different temperatures from [4]

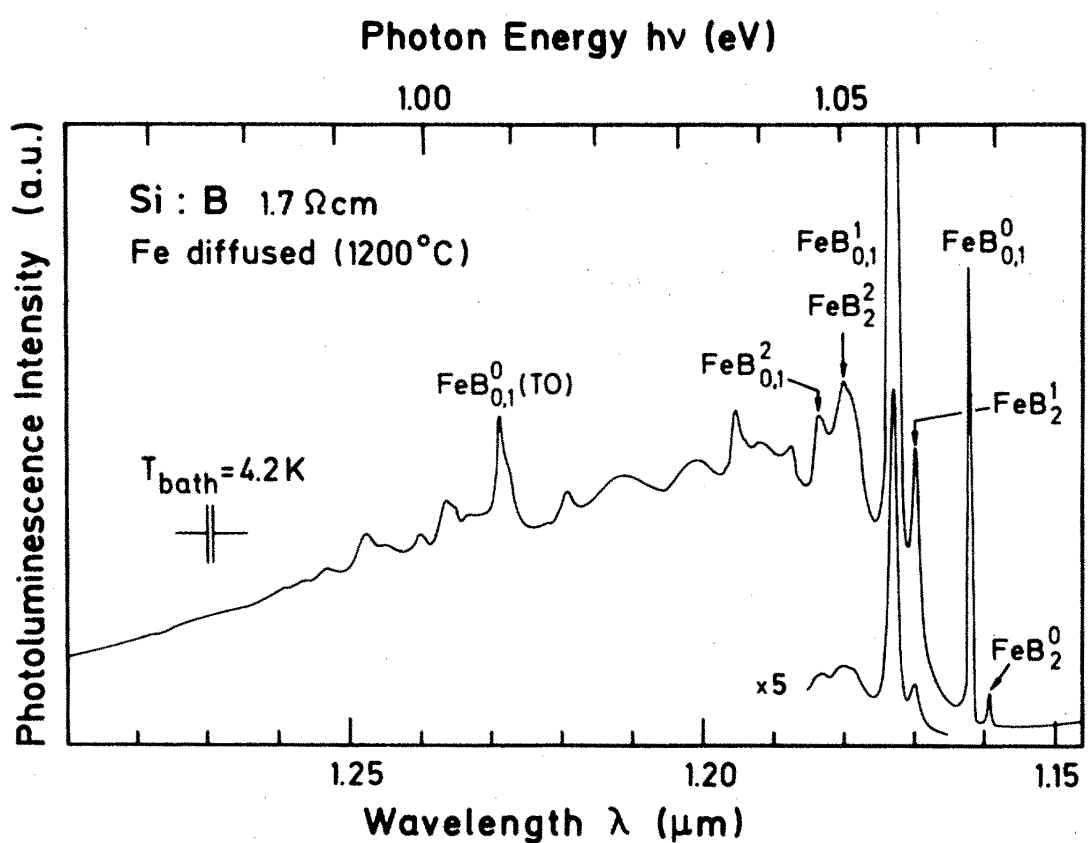


Figure 83: Iron diffused boron doped Si sample from [5]

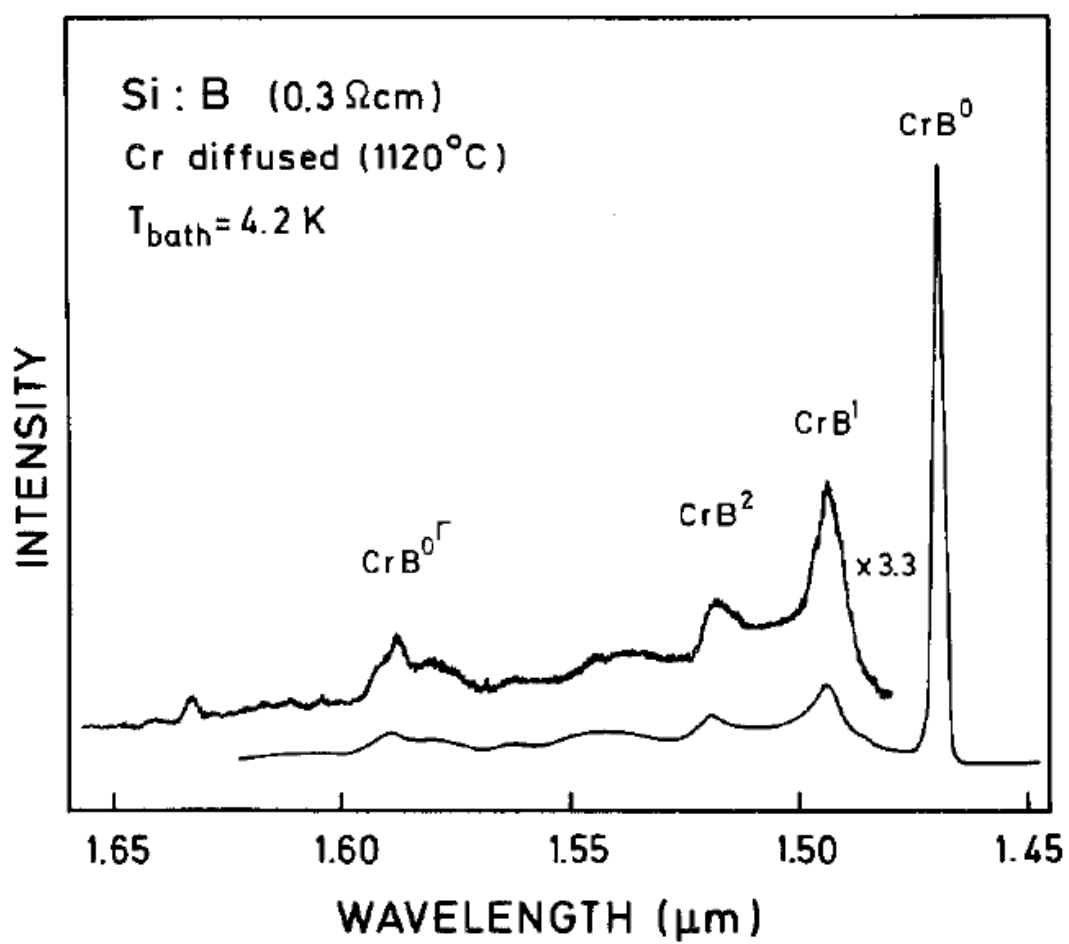


Figure 84: Chromium diffused Boron doped Si sample from [6]

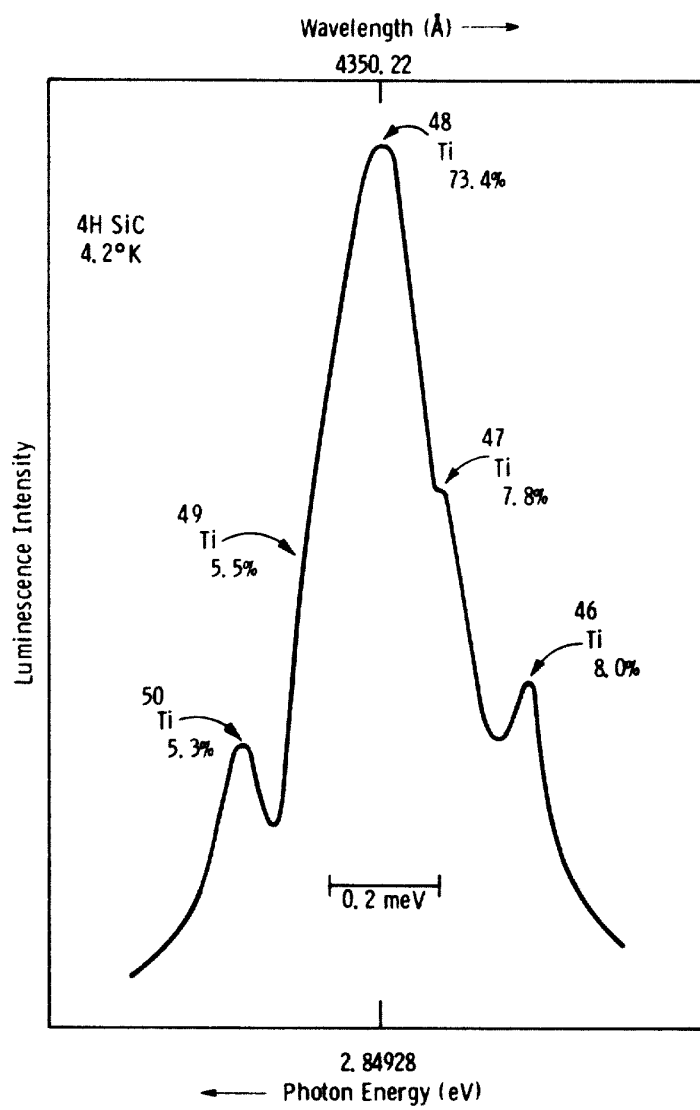


Figure 85: Titanium PL from Ti contaminated 4H SiC from [7]

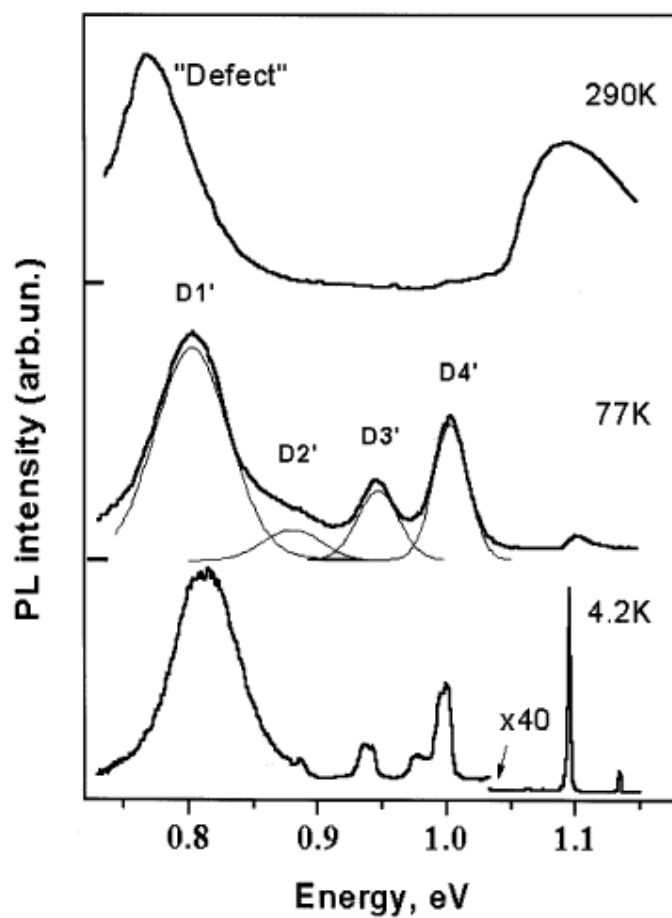


Figure 86: Dislocation related luminescence from mc-Si at different temperatures. The spectrum at 77 K is deconvolution numerical to resolve four individual Gaussian peaks. From [8].

Ref.	Sample type	Excitation process	Area	Processing	Doping
[36]	mc-Si	532nm Nd:YVO <sub>4</sub>	0.1mW/10 μm diameter	Sawing damage etched by HNO <sub>3</sub> /HF	B-doped
[46]	Cz-Si	Kr ion laser 647nm	10 μm		Undoped
[24]	Cz-Si	Xenon lamp	50mW on 3mm modulated at 9Hz	deformed by bending at 850° C	undoped, weak n and p
[15]	mc-Si	800nm AlGaAs laser	Pulsed 300mW / 3mm		Block-casting technique for Baysix
[8]	mc-Si	800nm AlGaAs at 140mW		Produced by EFG	
[9]	mc-Si and FZ-Si	Ar ion 514nm at 300mW	100μm	Produced by EFG	boron doped 10 <sup>15</sup> cm <sup>-3</sup>
[26]	FZ-Si	Kr-ion 647nm, Ar-ion 41.5nm and Nd-YAG 1064nm		Deformed a 650° C and 850° C	residual 10 <sup>12</sup> cm <sup>-3</sup> boron
[47]	mc-Si	Nd:YVO 532nm	6mW, 10μm diameter	Slicing damage etched off by HNO <sub>3</sub> /HF.	boron doped
[6]	FZ-Si and CZ-Si		50mW laser	Etched with HNO <sub>3</sub> /HF. Chromium diffused	boron doped
[5]	FZ-Si	Ar+ 514nm	500mW	Fe diffused	boron doped
[4]	FZ-Si	Argon laser		Fe diffusion	undoped
[38]		Ar <sup>+</sup> 514nm at 1.5W			Cu doped
[32]	FZ-Si	Ar <sup>+</sup> 514nm		Heated above a Bunsen burner.	Doped with Cu and/or Fe
[66]	mc-Si		6W/cm <sup>2</sup>	Polished by HNO <sub>3</sub> /HF	Undoped
[3]	CZ-Si	200W mercury arc 2.5eV			Undoped and doped
[44]		Ar <sup>+</sup> or Kr <sup>+</sup> laser 0.6W	0.8mm diameter	Dislocations by bending at 700°C	phosphorus doped

Table 8: Sample types and procedures

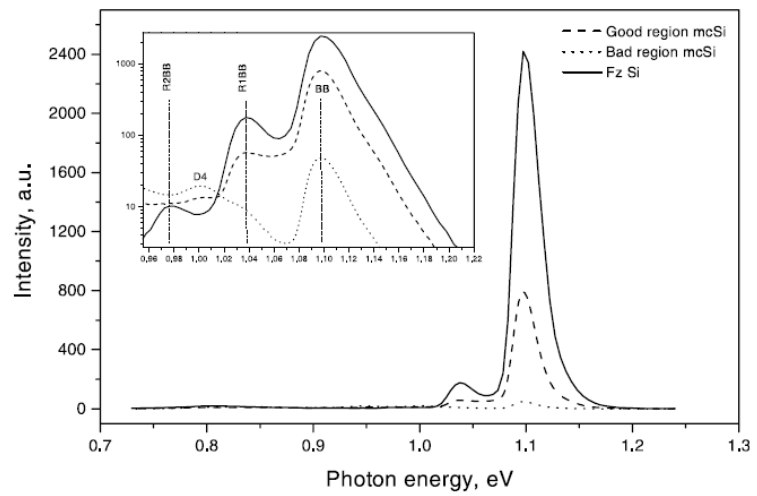


Figure 87: Comparison of the spectra in high and low quality regions of mc-Si with FZ-Si from [9]

## C Abbreviations

Abbreviation	Description
$B_{TO}$	TO phonon replica of the Boron bound exiton
BE	Bound exciton
$D_a$	Broad background emission
$D_b$	Oxygen impurity band
CZ-Si	Czochralski processed Silicon
D1	Dislocation related line 1
D1'	Dislocation related line 1 for mc-Si
D2	Dislocation related line 2
D2'	Dislocation related line 2 for mc-Si
D3	Dislocation related line 3
D3'	Dislocation related line 3 for mc-Si
D4	Dislocation related line 4
D4'	Dislocation related line 4 for mc-Si
EBIC	Electron beam induced current
EBSP	Electron Backscatter Diffraction Pattern
EHD	Electron Hole Droplet
FE	Free exciton
FZ-Si	Float-zone silicon
EFG	Edge-define Film-fed Growth
$I^{TO}$	Intrinsic TO phonon assisted
LO	Longitudinal Optical phonon mode
mc-Si	Multicrystalline silicon
ppba	Parts Per Billion Atomic
ppbw	Parts Per Billion by Weight
R1BB	One phonon replica of band edge emission
R2BB	Two phonon replica of band edge emission
TA	Transerval Acoustical phonon mode
TO	Transversal Optical phonon mode
SA GB	Small Angle Grain Boundary
ZPL	Zero Phonon Line

Table 9: Abbreviations

## D Matlab code

### D.1 Dead pixel correction

```
function [C] = dead_pixel_correction(A)
% Copy neighbour value on defect pixels in InGaAs camera.
    C = A;
    C(401,2) = A(400,2); % Defective (slightly to low)
    C(723,2) = A(722,2); % Defective (slightly to high)
    C(933,2) = A(932,2); % This pixel is dead (too high values)
    C(873,2) = A(872,2); % This pixel is dead (too low values)
end
```

### D.2 Dark current noise estimation removal

```
function[C] = dark_current_noise_removal(A,B)
% Smoothens noise, and find min value, and remove offset.
% Negative values from noise are truncated to 0.
% A and B MUST be of equal length!

if (length(A) ~= length(B))
    X = 'Length different from B';
    B = [];
end
if (isempty(B))
    % No noise is measured, remove a static offset instead.
    C = A;
    Ay = A(:,2); % Amplitude values
    Ay = sgolayfilt(Ay,1,255); % 1st order filtering
    offset = min(Ay); % Minimum offset, from noise averaging

    for i=1:length(A),
        new_value = A(i,2)-offset;
        if (new_value < 0)
            new_value = 0;
        end
        C(i,2) = new_value;
    end
else
    % B matrix is the noise measurement
    % - filter, and remove offset
    C = A;
    By = B(:,2); % Amplitude values
    OFFSET = sgolayfilt(By,1,25); % 1st order filtering
```

```

for i=1:length(A),
    new_y_value = (C(i,2) - OFFSET(i));
    % white noise artifacts can result in < 0 values which are
    % clearly not possible in real life
    if (new_y_value < 0)
        new_y_value = 0;
    end
    C(i,2) = new_y_value;
end
end

```

### D.3 Read result files from directory

```

function [C] = get_result_from_dir(dname,delimiter,drop_rightside)
% Reads all files in a directory, and return matrix elements
% separated by delimiter from file contents

C = 0;

% Read directory
files = dir(dname);

% Sort filenames in dir
filenames = {files.name};

% Sort numbers in string logically
[dummy, index] = sort_nat(filenames);

% re-index the files array:
files = files(index);

% Combine files to one large array
for i=1:length(files),
    if (files(i).name == '.') % Do nothing
    elseif (strcmp(files(i).name,'..')) % Do nothing
        elseif (strcmp(files(i).name,'.svn')) % Do nothing
    else
        % Read file contents into memory
        A = dlmread([dname,files(i).name],delimiter);

        % Filter out dead pixels in the InGaAs camera
        A = dead_pixel_correction(A);
        if (0 == C)
            C=A;
        else
            C=[C;A];
        end
    end
end

```

```

        else
            if (drop_rightside == 0)
                C = matrix_align_and_glue(C,A);
            else
                C = matrix_align_and_glue_reverse(C,A);
            end
        end
    end
end

```

## D.4 Remove overlap and glue intervals

```

function[C] = matrix_align_and_glue_reverse(A,B)

overlapIndex = 0;

% Drop the left side in the interval
for i=1:length(B),
    if (A(length(A),1) < B(i,1))
        overlapIndex = i;
        break;
    end
end

% Define new array length
sizeA = length(A);
sizeB = length(B);
new_array_size = (sizeA+sizeB-overlapIndex);

% Define right length of array
temp_C = zeros([new_array_size 2]);

% Add existing elements
for j = 1:length(A),
    temp_C(j,1) = A(j,1);
    temp_C(j,2) = A(j,2);
end

% Add new elements
for k = 1:(length(B)-overlapIndex),
    temp_C((length(A)+k),1) = B(overlapIndex+k,1);
    temp_C((length(A)+k),2) = B(overlapIndex+k,2);
end

C = temp_C;

```

```
end
```

## D.5 Filter and plot results

```
function plot_result(Result,fig_number,type,legend1,title1,fontsize,plot_type,sgoffilter_strength)

    % Define X and Y values
    Ax = Result(:,1);
    Ay = Result(:,2);

    % Filter
    if (sgofilter_strength > 0)
        % 1st order filtering
        Ay = sgolayfilt(Ay,1,sgofilter_strength);
    end

    % Calculate ev values if needed
    if (strcmp(type,'ev'))
        Ax = nm_to_ev(Ax);
        xlabel1 = 'Energy [eV]';
    else
        xlabel1 = 'Wavelength [nm]';
    end

    % Detect same figure plot
    cf = get(0,'CurrentFigure');
    fill_info = 0;
    if (isempty(cf))
        fill_info = 1;
    end
    if (cf ~= fig_number)
        fill_info = 1;
    end

    % Plot
    fig = figure(fig_number);

    if (fill_info)
        axes1 = axes('Parent',fig,'FontSize',fontsize);
        box(axes1,'on');

        hold(axes1,'all');
        hold on;
    end

    plot(Ax,Ay,plot_type);
```

```
% If no figure exists, input info
if (fill_info) % Don't add info twice
    legend(legend1);
    title(title1);
    ylabel('Counts');
    xlabel(xlabel1);
end
end
```